Fusion Materials Research at Oak Ridge National Laboratory in Fiscal Year 2019

Compiled by:

F.W. Wiffen
Y. Katoh
S. Melton

February 2020

OAK RIDGE NATIONAL LABORATORY
MANAGED BY UT-BATTELLE FOR THE US DEPARTMENT OF ENERGY

ORNL/TM-2020/1456

Materials Science and Technology Division

FUSION MATERIALS RESEARCH AT OAK RIDGE NATIONAL LABORATORY IN FISCAL YEAR 2019

Compiled by:

F.W. Wiffen
Y. Katoh
S. Melton

Date Published: February 2020

CONTENTS

LIST OF FIGURES

LIST OF TABLES

1. INTRODUCTION

Yutai Katoh (katohy@ornl.gov), F.W. Wiffen

This is the eighth Annual report of the Oak Ridge National Laboratory (ORNL) program aimed at developing and qualifying materials that can meet the application requirements of fusion power systems, especially the near-plasma regions of those systems. Earlier issues of these annual reports can be found at the Fusion Materials Program website at https://www.ornl.gov/division/mstd/program/fusion-materials; more detailed reporting for those and many earlier years are contained in the series of Semiannual Progress reports at the same website, and the detailed results of the program are contained in the published scientific literature.

Achieving fusion energy presents a formidable challenge to the field of materials science, to provide a suite of suitable materials in close integration to the plasma physics and other applied technologies. The technological challenge presented by the conceptual future fusion power systems is the inability of current materials and components to withstand the harsh fusion nuclear environment. The overarching goal of the ORNL fusion materials program is to provide the applied materials science support and materials understanding to underpin the ongoing Department of Energy (DOE) Office of Science - Fusion Energy Sciences (FES) program, in parallel with developing materials for fusion power systems. In this effort the program continues to be integrated both with the larger United States (U.S.) and international fusion materials communities and with the international fusion design and technology communities.

This long-running ORNL program continues to pursue development of low activation structural materials, with the greatest effort directed at the Reduced Activation Ferritic/Martensitic (RAFM) Steels, higher strength/higher creep resistant/coolant compatible/radiation tolerant advanced steels, and Silicon Carbide Composites. Tasks within the steels portfolio are pursuing several options for advanced steels: These include development of Castable Nanostructured Alloys, exploratory work on Bainitic steels and Oxide Dispersion Strengthened (ODS) ferrous alloys, and Aluminum containing alloys that promise improved liquid metal compatibility. Parallel to this is the increased emphasis on radiation effects, high heat flux testing and the development of refractory metals, especially tungsten materials. This includes the thermal testing of irradiated materials, the development and evaluation of new tungsten materials, and the study and understanding of the irradiation performance of tungsten. Newer efforts also support the Blanket and Fuel Cycle Programs. In each case the materials are being developed in a design-informed fashion where properties improvements are led by fusion-relevant design studies and directed at advancing the Technology Readiness Level of the material systems.

Continuing work supported by an Early Career Award is looking in depth at the materials side of the Plasma Materials Interactions, characterizing the materials response to plasma impingement and determining the controlling mechanisms of the materials behavior.

In FY 2019, new activities were initiated within the ORNL fusion materials program and assisting other emerging FES fusion technology programs. A new program element explores application of advanced manufacturing technologies to production of tungsten plasma facing materials and advanced heat-resistant RAFM steels with the goal of innovating a new generation of plasma-facing components. Newer efforts also support the Blanket and Fuel Cycle Program and Liquid Metal Plasma-Facing Component Program.

A limited effort is directed at examining functional and exploratory materials. Work on materials for diagnostic systems has recently been inactive, although ORNL stands ready to support basic irradiation materials science of ceramics that could be used in diagnostic systems. For high-temperature superconductors, ORNL has a limited program to quantify the irradiation sensitivity of the most recently developed tape materials. A new fixture to evaluate effects of gamma field exposure of these materials is

ready for use with the spent High Flux Isotope Reactor (HFIR) core radiation source. A small effort is evaluating better copper alloys for use in components subjected to high heat loading.

This program integrates fundamental modeling into the development efforts as much as practicable, directed especially at understanding experimentally observed behavior.

This fusion materials program makes heavy reliance on neutron irradiation in HFIR at ORNL, complemented by limited use of ion irradiation facilities when these are better suited to explore fundamental aspects of materials behavior under irradiation. Associated with the HFIR irradiations is the infrastructure needed to evaluate the effects of the irradiation on the material properties and microstructures. This requires both the hot cells needed for experiment disassembly and the equipment to test highly radioactive specimens, and the shielded test equipment in the Low Activation Materials Development and Analysis Laboratory (LAMDA). Maintaining, upgrading, and replacing this state-of-the-art suite of instruments and test stands is an ongoing effort, shared with other programs focused on similar needs.

The program provides limited support to the FES System Studies team, reported as "Materials Engineering in Support of the FNSF Program."

The fusion materials effort consists of a wide array of tasks and collaborations both within the U.S. and with international partners. The major continuing international collaborating partners are the Japanese National Institutes for Quantum and Radiological Science and Technology (QST) collaboration, focused on structural materials, the Japanese National Institute for Fusion Science (the ending PHENIX collaboration, replaced midyear by the FRONTIER collaboration) and the Karlsruhe Institute of Technology in Germany, acting for EUROfusion (examining steel materials).

Because the biannual International Conference on Fusion Reactor Materials was scheduled for October 2019, a lot of the FY 2019 effort was directed at bringing work to suitable points for reporting to the international community. We expect that this will result in several technical publications submitted to the Journal of Nuclear Materials and other appropriate journals during FY 2020.

The FY 2019 Materials Research activities supporting the Office of Science, Office of Fusion Energy Sciences carried out by ORNL are reported here. The organization of the report is mainly by material type, with sections on each of the many specific technical activities.

2. ADVANCED STEELS

2.1 DEVELOPMENT OF ADVANCED RAFM STEELS – CASTABLE NANOSTRUCTURED ALLOYS

L. Tan (tanl@ornl.gov), J.D. Poplawsky, Y. Yang, Y. Katoh

OBJECTIVE

Castable nanostructure alloys (CNAs) are being developed at ORNL to fill the performance gap between current reduced-activation ferritic-martensitic (RAFM) steels and oxide-dispersion-strengthened (ODS) alloys. The ODS alloys develop a large amount of ultrafine oxide clusters/precipitates via powder metallurgy technology. The CNAs will develop similar microstructures with carbonitrides or carbides via conventional, affordable steel making methods. The FY 2019 effort focused on microstructural characterization of two CNAs by atom probe tomography (APT) and transmission electron microscopy (TEM).

SUMMARY

The APT has been rarely used to characterize RAFM steels because the low density of precipitates is difficult to probe. Two carbide-version CNAs were characterized by APT and TEM, with good agreement in the sizes and density of MX precipitates determined by each technique. The size and density of MX in the CNA3 are comparable to that of oxide clusters in an ODS-Eurofer. The APT also provided high-fidelity chemistry analyses of the precipitates, allowing better understanding of their stabilities in terms of transmutation and thermodynamics. The study also suggests that melting solely by vacuum induction melting (VIM) is not enough to provide good impurity control for the desired amount of MX formation.

PROGRESS AND STATUS

The initial development of CNAs focused on carbonitride version with increased nitrogen content favoring a larger amount of $(V,Ta)(C,N)$ type MX precipitates, which yielded a representative alloy CNA1. Since then the development of CNAs has focused on carbide version, promoting $(Ti,Ta)C$ type MX precipitates, which yielded a series of alloys from CNA2 to the recent CNA7. To have a better statistical comparison with the carbide-version CNAs, the carbonitride-version CNA was revisited with a representative alloy CC22 having a comparable amount of carbonitride MX but noticeably less $M_{23}C_6$ than in CNA1. The tensile strength, creep resistance, and Charpy impact toughness of CC22 were reported in the Semiannual Progress Report (DOE/ER-0313/65, Vol. 65, December 31, 2018, https://www.ornl.gov/division/mstd/program/fusion-materials). In general, carbonitride- and carbide-version CNAs showed similar tensile properties and creep resistance. However, their Charpy impact toughness had a large variation, especially in the upper-shelf energy (USE), as shown in *Figure 1*. The carbide-version CNAs showed higher USE and lower ductile-brittle transition temperature than the carbonitride-version CNAs. CNA3 and CNA7, fabricated by vacuum arc melting (VAM) and VIM, respectively, had similar USE, higher than the other CNAs. Therefore, these two alloys were selected for detailed parallel characterization using APT and TEM.

Figure 2 shows examples of APT results for CNA3 and CNA7, illustrating the sizes and distribution of MX precipitates in the matrix and both $M_{23}C_6$ and MX at a grain boundary in CNA3 while only a single large MX precipitate was probed in CNA7. The TEM-characterized ultrafine dispersive MX precipitates in the matrix of CNA3 had sizes (~3–28 nm) and density [~$(1.1–1.4)\times10^{22}$ m^{-3}] consistent with the APT results. These results are comparable to that of oxide clusters in ODS-Eurofer (0.5%Y_2O_3). The APT

results also gave high-fidelity chemistry of the MX, $M_{23}C_6$, and matrix phases. The TEM characterization of CNA7 indicated a lower density of MX than in CNA3. This is attributed to the higher oxygen content in CNA7 revealed by the alloy composition analyses and the APT results, which tied up too much of the Ti and Ta. Therefore, VIM melting alone is not enough for RAFM steel fabrication. Additional refinement in melting, such as electro-slag re-melting (ESR) or vacuum arc re-melting (VAR), will be necessary to reduce the impurities in large scale heat production.
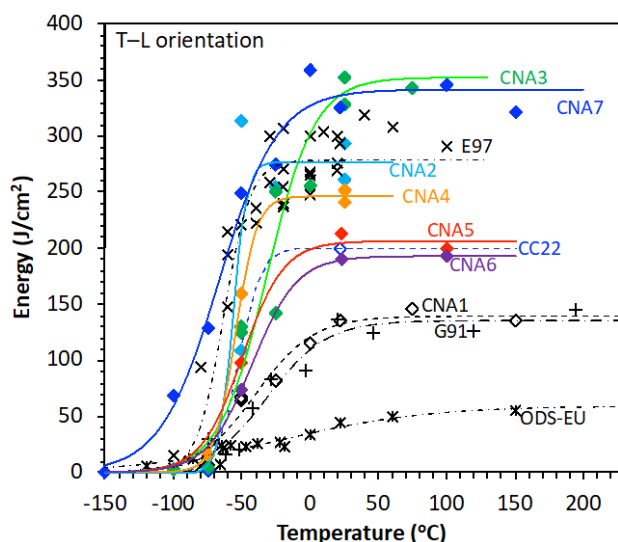
Figure 1. Charpy impact toughness of CNAs compared with literature data of Eurofer97, Grade 91, and ODS-Eurofer alloys.
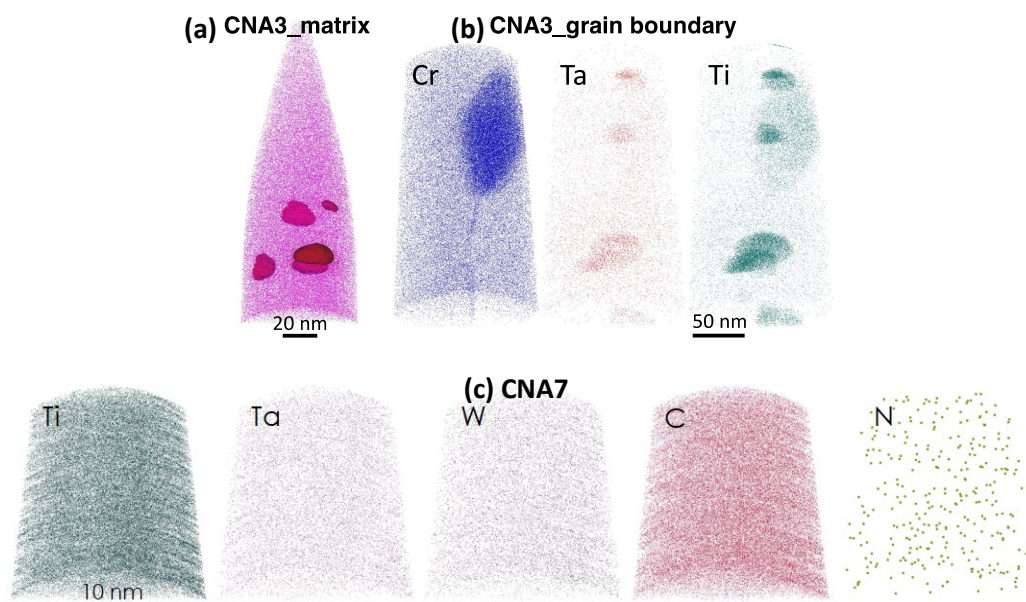
Figure 2. Representative APT results for (a-b) CNA3 and (c) CNA7, showing precipitates in the matrix and at a grain boundary.

4

FUTURE PLANS

Based on the collected results developed on these CNA heats, one CNA will be selected for a 400-lb heat produced by VIM+ESR or VIM+VAR.

2.2 REVISITING THE CARBONITRIDE – VERSION CASTABLE NANOSTRUCTURED ALLOYS

T. Graening, L. Tan, Y. Yang (yangying@ornl.gov)

OBJECTIVE

A carbonitride-version of castable nanostructure alloys (CNAs) was formulated in the initial developmental stage of CNAs by increasing the nitrogen content to favor the formation of (V,Ta)(C,N)-type MX precipitates. The composition was recently revised to reduce the fraction of $M_{23}C_6$ precipitates, thus increasing the phase fraction ratio of MX/$M_{23}C_6$. This serves to investigate the effect of slight changes in the minor alloying elements on the microstructure and mechanical properties. A systematic analysis of three variants of carbonitride-version CNA with different chemical compositions using SEM, TEM and tensile and Charpy impact toughness tests will be compared with the established carbonitride- and carbide-version CNAs.

SUMMARY

Microstructure characterization and mechanical test of the carbonitride-version CNA variants were performed. A decreased normalization temperature of 1070°C and the high MX/$M_{23}C_6$ ratio decreased the prior austenite grain (PAG) size. Clear correlations between the PAG, packet, and block sizes and the lath widths were identified. An inhomogeneous distribution of MX and $M_{23}C_6$ precipitates along the grain boundaries in the CNAs was found, without the formation of small nanoscale precipitates within the grains. Mechanical tests showed an increased upper-shelf energy, a reduced DBTT and an increased yield strength (only for CNA22).

PROGRESS AND STATUS

The chemical compositions of three carbonitride-version CNAs were optimized using thermodynamic calculations to achieve a finer-scale microstructure and an increased ratio of MX to $M_{23}C_6$ precipitates. The results are displayed in ***Figure 3***. The three new CNAs have a lower content of C to reduce the amount of $M_{23}C_6$, with the amount of N unable to be controlled as high as the reference steel, while the increased ratio of N/C led to an increased ratio of MX/$M_{23}C_6$. CNA22, CNA21, and CNA23 have a decreasing amount of the minor elements and a decreasing ratio of MX/$M_{23}C_6$ in the mentioned order.

The impacts of the changed chemical compositions and a lowered normalization temperature (reduction from 1200 to 1070°C) are displayed as inverse pole figure (IPF) maps in ***Figure 4***. Much smaller PAG, block and packet sizes are visible for all three alloys in comparison with a reference alloy 1539F. All microstructural features are combined in ***Figure 5***, which summarizes the superior microstructure of CNA22 in comparison with all other alloys. ***Figure 5*** shows the ultimate tensile strength at 700°C plotted against the DBTT. CNA21 and 23 have the lowest DBTT due to the smallest number of minor elements, but the lack of precipitates led to a decreased ultimate tensile strength (UTS). CNA22, showing the highest MX/$M_{23}C_6$ ratio and highest amount of elements C and N among the three new CNAs, shows a lower DBTT (by 40°C) and a higher UTS (by 110 MPa) at 700°C.

The TEM EDS maps of each sample at different magnifications were recorded to investigate the distribution and sizes of the precipitates (not shown here). No significant differences between the three alloys were observed. However, most of the precipitates were located along grain boundaries and no small nano-scaled precipitates were found within grains, which could lead to lower creep and irradiation resistance.

FUTURE PLANS

The hypothesis of the alloys with reduced $M_{23}C_6$ favoring greater creep resistance will be investigated.
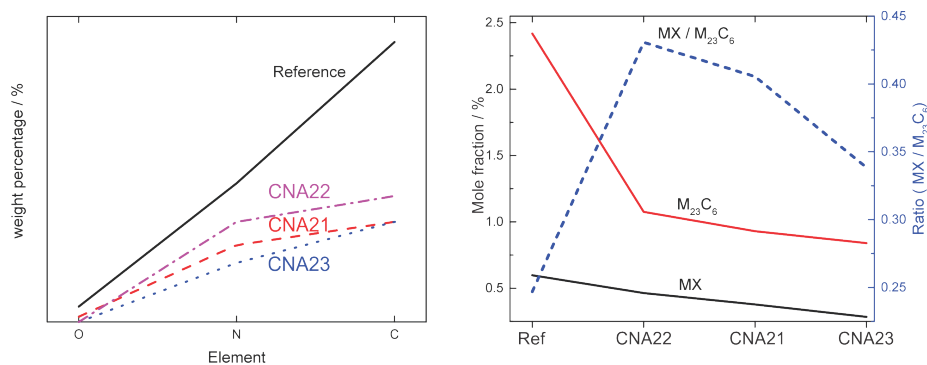
Figure 3. Minor elements chemical composition and calculated precipitate formation in three CNAs and a reference alloy.
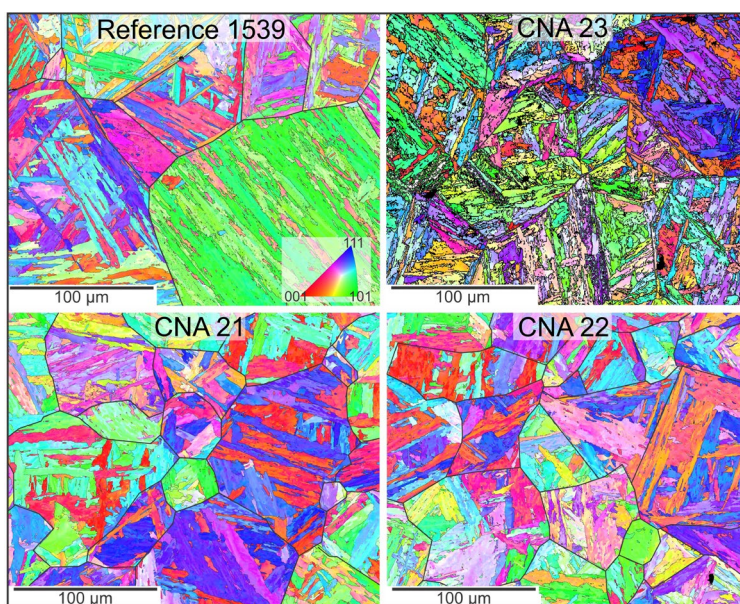
Figure 4. EBSD images used to determine PAG, block and packet sizes of the alloys evaluated in this study.
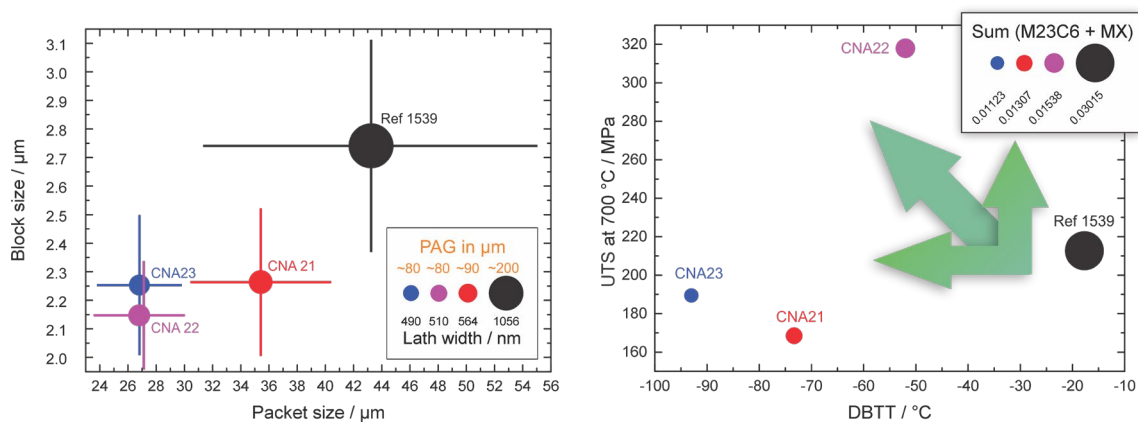
Figure 5. Summary comparison of the microstructures of four alloys shown beside a comparison of the results of strength and toughness testing.

2.3   RADIOLOGICAL ANALYSIS AND TRANSMUTATION CONSIDERATIONS FOR CASTABLE NANOSTRUCTURED ALLOYS

W. Zhong, L. Tan (tanl@ornl.gov)

OBJECTIVE

The development of new generation reduced-activation ferritic-martensitic (RAFM) steels via fine control of alloy composition must consider the radiological effect induced by the composition variation. With impurity control practice like current RAFM steels, castable nanostructured alloys (CNAs) have a few key alloying element changes to increase the density of nanoscale precipitates. Therefore, radiological analysis on the CNAs is necessary to evaluate the radiological impact from the composition variations. The result for CNAs will be compared to the current RAFM steels Eurofer 97 and F82H.

SUMMARY

Radiological analysis of representative carbonitride- and carbide-version CNAs, i.e., CNA1 and CNA3, respectively, was conducted using a fusion First Wall neutron spectrum. The CNAs showed reduced radioactivity at long times after reactor shutdown. In addition, transmutation calculations indicated that the composition evolution of the (V,Ta)(C,N)-type MX precipitate in CNA1 would be slower under a fusion First Wall spectrum than that under the High Flux Isotope Reactor (HFIR) neutron spectrum.

PROGRESS AND STATUS

Radiological analysis was performed on the CNA1and CNA3 alloys using the ORIGEN code with a fusion First-Wall neutron spectrum, assuming five-year service in a fusion reactor. These alloys were selected as the representative of the carbonitride- and carbide-version CNAs, and the results were compared with the current RAFM steels Eurofer 97-2 and F82H-BA12.

The CNAs show low radioactivity after reactor shutdown. ***Figure 6*** shows the dose rate as a function of decay time of the two alloys, together with Eurofer97-2 and F82H-BA12. Both CNA1 and CNA3 show reduced contact dose rate after reactor shutdown. The CNA1 has a higher nitrogen content than Eurofer97-2 and F82H-BA12, which leads to higher activity at longer times due to the production of ^{14}C from the nitrogen. However, the ^{14}C does not contribute to the contact dose rate. Unlike CNA3 which has a comprehensive impurity list like Eurofer97-2 and F82H-BA12, the limited impurities considered for CNA1 will have underestimated its dose rate.

Transmutations lead to composition changes in a reactor environment, which could affect the stability of precipitates and subsequent mechanical properties. (V,Ta)(C,N)-type MX precipitate is one of the typical precipitates in CNA1. ***Figure 7*** shows the transmutation-induced composition evolution of such a precipitate under the HFIR and fusion First Wall neutron spectra. Larger composition changes are present in the carbonitride MX precipitate in the HFIR, and this is most evident for Ta content being reduced from ~11 at% to below 0.05 at% with the production of W, Re and Os. However, the precipitate has relatively smaller composition changes under the fusion First Wall spectrum, with the initial ~11 at% Ta only reduced to ~8 at%.

FUTURE PLANS

Different steelmaking methods will inevitably affect the impurity levels in CNAs, which will influence the radioactivity after service. Similar calculations and analyses will be pursued for alloys with significant changes in specific alloying elements and impurities to ensure that the development of CNAs follows the

general RAFM steel radiological guidelines and to assist data interpretation for neutron-irradiated CNAs.
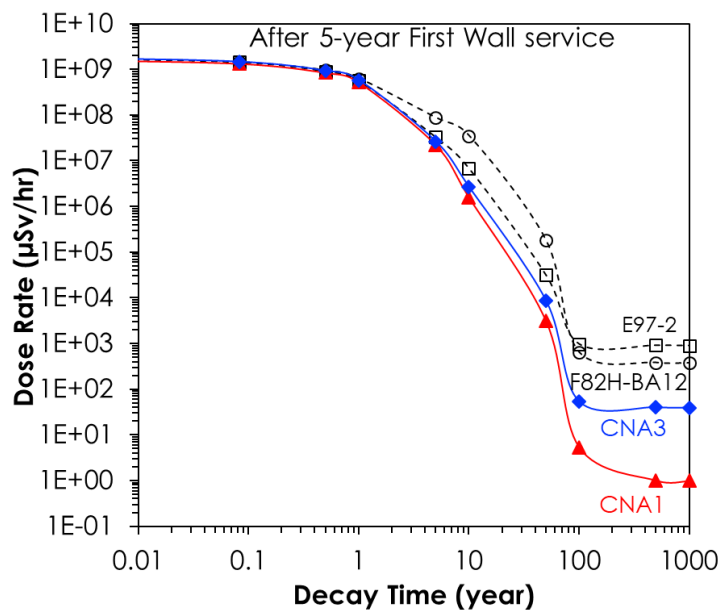
Figure 6. Decay time dependent dose rate of CNA1 and CNA3, calculated using the ORIGEN code for a fusion First-Wall neutron spectrum and five-year service life.
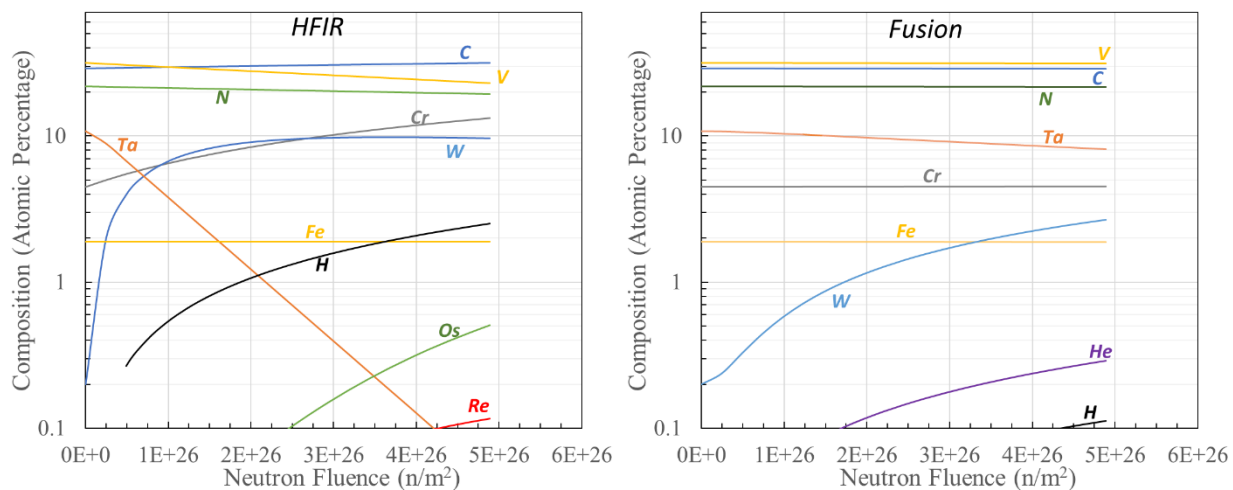
Figure 7. Composition evolution of (V,Ta)(C,N) in CNA1 as a function of fluence of neutrons over 0.1 MeV in the HFIR (left) and fusion First Wall (right).

2.4   EVALUATION OF A NEUTRON-IRRADIATED CARBONITRIDE-VERSION CASTABLE NANOSTRUCTURED ALLOY

L. Tan (tanl@ornl.gov), W. Zhong

OBJECTIVE

Superior radiation resistance is the ultimate developmental goal for castable nanostructure alloys (CNAs). While some of the carbide-version CNAs are now being irradiated, the HFIR irradiation of some carbonitride-version CNA1 specimens was recently completed. This work reports the progress of the post-irradiation examination (PIE) of the CNA1 specimens.

SUMMARY

Detailed PIE was conducted for the CNA1 (carbonitride-version) irradiated to ~7.4 dpa at ~490°C in the HFIR. Room-temperature Vickers hardness and tensile properties revealed consistent softening that is attributed to radiation-enhanced recovery, resulting in reduced lath boundaries and dislocation density. Transmission electron microscopy (TEM), together with energy dispersive x-ray spectroscopy (EDS), showed radiation-induced dislocation loops, few cavities, and slight dissolution of $M_{23}C_6$ and MX precipitates. Partial amorphization was only observed in $M_{23}C_6$ precipitated in matrix. Transmutation slightly destabilized $M_{23}C_6$ and MX, with a stronger effect on the later shown by noticeable depletion of Ta with enriched W. This is consistent with transmutation calculations. The transmutation-induced composition changes tended to destabilize the two types of precipitates according to computational thermodynamics, supporting the observed slight dissolution.

PROGRESS AND STATUS

The initial developmental stage of CNAs was focused on a carbonitride-version of the alloy by increasing nitrogen content to maximize the phase fraction of carbonitride type MX (M=V/Ta, X=C/N). The CNA1 is a representative alloy of the carbonitride-version CNAs. Type SS-J2 miniature tensile specimens of CNA1 were irradiated in the HFIR at target temperatures of 300, 500, and 650°C. Analyses of the SiC temperature monitors irradiated in the same capsules as the CNA1 specimens suggested significant deviations of the irradiation temperatures from the target temperatures, e.g., ~94 to ~190°C higher than the targeted 300°C. Room-temperature tensile tests and Vickers hardness measurements were conducted on the irradiated CNA1. The two CNA1 specimens irradiated at lower doses (0.02/0.52 dpa) and lower temperatures (394/400°C) showed slight hardening compared with the unirradiated sample. However, the CNA1 specimen irradiated to ~7.4 dpa at ~490°C exhibited noticeable softening with reduced strength and increased elongation, as shown in ***Figure 8*a**. Therefore, detailed microstructural characterization and analyses were conducted on the ~7.4 dpa and ~490°C specimen. The radiation-induced mechanical property changes and basic microstructural evolution were reported in the Semiannual Progress Report (DOE/ER-0313/66, Vol. 66, June 30, 2019).

***Figure 8*b** shows an example of TEM characterization of a MX precipitate in the CNA1 irradiated to ~7.4 dpa at ~490°C, indicating a matrix nanoscale precipitate interacting with dislocations. The high-resolution TEM image with its fast Fourier transform suggests an orientation relationship of $(200)_{MX} \parallel (110)_{bcc}$ and $[011]_{MX} \parallel [001]_{bcc}$. Similar TEM characterization was performed for $M_{23}C_6$ at boundaries and in the matrix. The irradiation did not alter the crystal structure of the precipitates but introduced partial amorphization in the $M_{23}C_6$ precipitated in the matrix. To analyze the stability of the precipitates, calculations were conducted using the ORIGEN code with the typical HFIR neutron spectrum. ***Figure 8*c** shows an example of the calculated dose-dependent composition evolution of MX, indicating significant reductions in Ta with increases in W, together with minor transmutations of V into Cr and N into C. The

EDS results of the MX precipitates at 0 and 7.4 dpa conditions are superimposed on the plot, showing good agreement with the calculation. The transmutation-calculated compositions of MX are used in the computational thermodynamic calculation with the result plotted in *Figure 8*d, indicating the destabilization (reduced fraction) of MX primarily induced by its component (Ta,V)C and slightly by V(C,N). The transmutation-induced WC could not compensate for the general reduction of MX. Similar calculations and analyses were performed for the $M_{23}C_6$ precipitates. The detailed characterization explains the observed softening of the CNA1 irradiated to ~7.4 dpa at ~490°C.
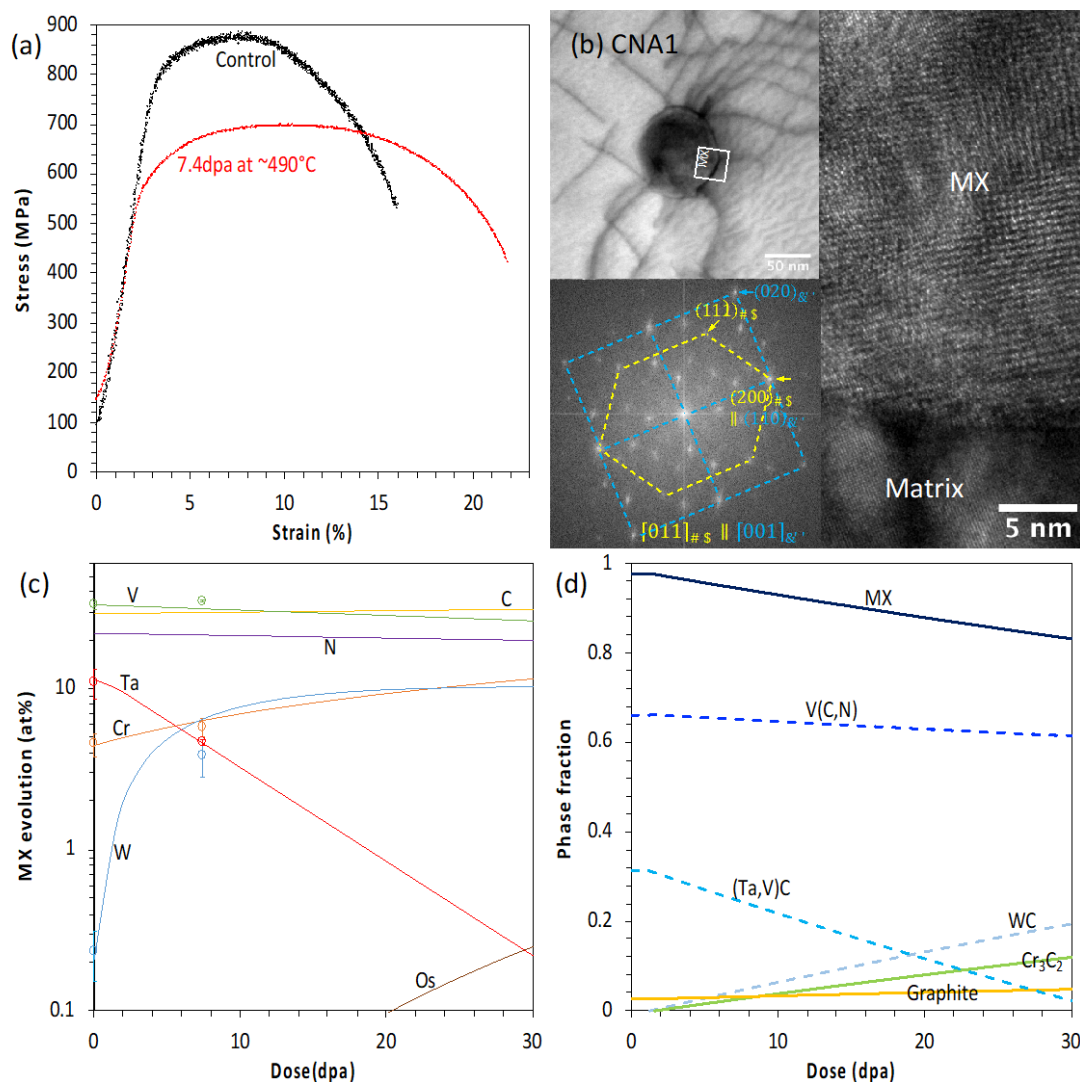
Figure 8. (a) Tensile stress-strain curves and examples of (b) TEM analysis of a MX precipitate, (c) transmutation calculation of dose-dependent composition evolution of MX, and (d) thermodynamics calculation of dose-dependent phase stability of MX.

FUTURE PLANS

Microstructural characterization of the CNA1 irradiated to 9 dpa at 609°C to understand the effect of irradiation temperature on microstructure and mechanical properties. The results will be compared with available literature data and future CNA irradiation results.

2.5   EVALUATION OF IRRADIATED EUROFUSION PROJECT ALLOYS

A. Bhattacharya (bhattacharya@ornl.gov), X. Chen, J. Reed, T. Graening, J.W. Geringer, Y. Katoh

OBJECTIVE

Ten different Eurofer97 RAFM steel variants that were designed by various European laboratories, were irradiated in HFIR to ITER relevant conditions of ~2.5 dpa, ~300 °C. The objective of this task was the post irradiation examination (PIE) of the irradiated steels in the ORNL hot cell and LAMDA facilities. Special emphasis was on the lower temperature embrittlement of these Eurofer97-type steels.

SUMMARY

Following neutron irradiations in HFIR and then SiC thermometry, a suite of mechanical testing that included Vickers hardness indentation tests, uniaxial tensile tests and miniature bend-bar fracture toughness tests were completed on the EUROfusion alloys. Vickers hardness tests revealed irradiation-induced hardening in all ten Eurofer97-type alloys. Tensile testing at both room temperature (RT) and irradiation temperature (300°C) quantified the hardening behavior in terms of the increase in the yield stress (YS) and loss of ductility.

PROGRESS AND STATUS

The safe operating temperature window for structural components fabricated from Eurofer97 steel is very narrow, between ~350-550°C. At low temperatures, safe operation is restricted by irradiation-induced embrittlement, which causes a loss of fracture toughness. At high temperatures, the restrictive factor is creep strength, which is expected to be exacerbated by irradiation. To address this issue, variants of the Eurofer97 alloy, produced using a combination of non-standard fabrication routes and minor alloy chemistry variations, were irradiated in HFIR targeting ITER relevant conditions of 2.5 dpa, 300°C. The fabrication route of these 10 different steels (designated H, I, P, J, K, L, M, N, O, P and reference E) are summarized in ***Table 1***.

Evaluation of the passive SiC thermometry was completed in the LAMDA lab for temperature monitors from the EUROfusion-program HFIR rabbit capsules (ES21 and ES22) designed to operate at 285±20 and 315±20°C respectively. A total of 18 of 24 SiC pieces were analyzed which provided a good knowledge of the temperature distribution for positions within each capsule. The estimated temperatures for both the rabbit capsules, divided into upper, middle and lower positions, are show in ***Figure 9***. This shows that the temperature spread within the capsules was reasonable, with a few exceptions. These exceptions were the samples where evaluated temperature was either higher than 335°C or lower than 260°C. Based on the thermometry results, appropriate samples were selected for hot cell hardness and tensile tests.

Following thermometry evaluation, Vickers hardness indentation tests were performed on the irradiated specimens and compared with the unirradiated reference materials, which revealed irradiation-induced hardening of all ten steels. These tests were performed on the SS-J3 type miniature tensile specimens, using 1 kg load, 15 s dwell time, following ASTM E384 standard. The measurements were performed on the grip/tap sections of the samples, with a minimum of 6 indents per sample. ***Figure 10*** presents a comparison of the irradiated and unirradiated Vickers hardness values for the ten steels, as well as a histogram of change in the hardness. It is evident that all the steels showed a significant hardness increase. What is interesting to note is that the two steels, series K and L, which had the highest hardness before irradiation (> 300 HV) showed the highest increase in hardness compared to the other steels. This suggests that designing steels with Eurofer97-like chemistry but with higher hardness may not be suitable

to address the embrittlement issue. However, it may have benefits when high temperature strength is the key requirement. All other steels showed hardness changes in the range ~55-80 HV (x9.8 MPa).

Table 1. Summary of the ten Eurofer-97 steel variants. AQ: air quenched, WQ: water quenched, LT: low temperature application, HT: high temperature application

M-Code	Material type	Heat	Condition	Provider
E	EUROFER97/2	993391	980°C/0.5h + AQ + 760°C + AC (reference)	KIT
H	EUROFER-LT	J362A	1000°C/0.5h + WQ + 820°C + AC	KIT
I	EUROFER-LT	J363A	1000°C/0.5h + WQ + 820°C + AC	KIT
P	EUROFER-LT	J361A	1000°C/0.5h + WQ + 820°C + AC	KIT
L	EUROFER97/2	994578	1150°C/0.5h + AQ + 700°C + AC	CEA
J	EUROFER-LT	I196C	TMT:1250°C/1h and then rolling to a final rolling temperature of 850°C in 6 rolling steps with a reduction of 20-30% for each rolling pass, then AC. Q&T: 880°C/0.5h+WQ+750°C/2h+AC	SCK.CEN
K	EUROFER-HT	I427A	TMT:1250°C/1h and then rolling to a final rolling temperature of 850°C in 6 rolling steps with a reduction of 20-30% for each rolling pass, then AC. Q&T: 1050°C/15min + WQ + 675°C/1.5h + AC	SCK.CEN
M	EUROFER97/2	993391	1020°C/0.5h + AQ + 1020°C/0.5h + AQ +760°C/1.5h + AC (double austenitization)	ENEA
O	EUROFER-LT	VM2991	TMT: 1080°C/1h, cooling to 650°C and rolling, reduction 40% (from 30 mm to 18mm) Tempering: 760°C/1h + AC	ENEA
N	EUROFER-LT	VM2897	920°C/1.5h + AQ + 920°C/1.5h + AQ + 760°C/1h + AC (double austenitization)	ENEA

After the Vickers hardness tests, uniaxial tensile tests were performed at room temperature and the irradiation temperature (300°C) on all ten steel variants. These tests were performed in the hot-cells on the SS-J3 specimens using the ASTM E8 Standard Test Methods for Tension Testing of Metallic Materials as a guideline. Tests were conducted using a nominal strain rate of ~ 10^{-3} s^{-1}. *Figure 11* compares the YS of the ten steels in the unirradiated and irradiated state. For all ten steels, a significant YS increases, symbolizing hardening, was observed. The YS increase is consistent with the Vickers hardness increases noted in *Figure 10*. Once again, the harder K series steel showed the maximum YS after irradiation, reaching values beyond 1 GPa.

FUTURE PLANS

The next step in this research will be to correlate the hardness and tensile test results with fracture toughness. Following this, detailed microstructural chararcterization of the steels will be performed at LAMDA to develop complete structure-property relationships of the steels. Sample sections have been cut and shipped to LAMDA where initial preparation using focused ion beam (FIB) is complete. Characterization will use conventional and analytical scanning transmission electron microscopy (STEM).
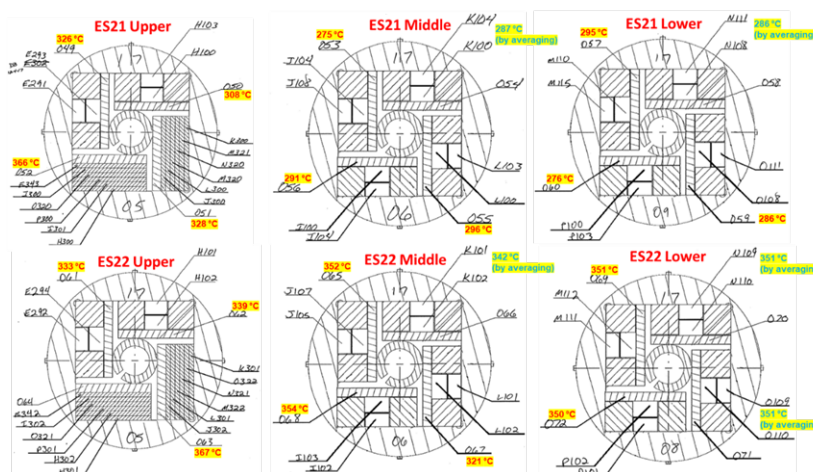
Figure 9. Temperature distribution overlaid on the HFIR loading scheme for the ES21 and ES22 capsules.

(a)   (b)
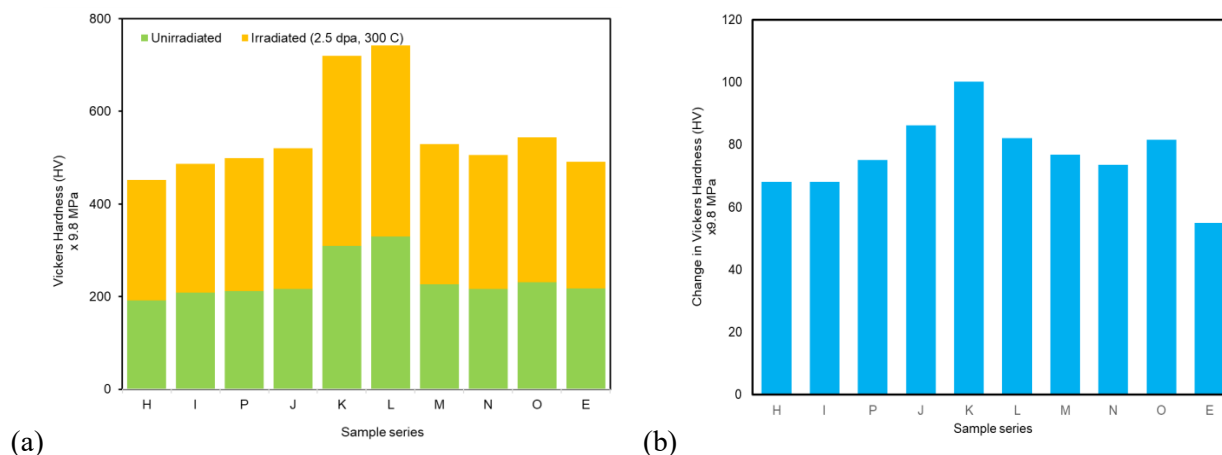
Figure 10. Vickers hardness values of the Eurofer97 steel variants. (a). Comparison of the unirradiated and irradiated steels. (b). Increase in hardness due to irradiation.
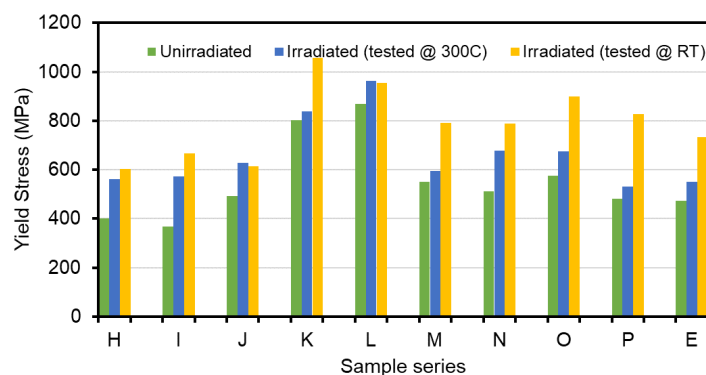
Figure 11. Yield Strengths of the ten Eurofer97 steel variants. The tests were performed on the unirradiated control specimens and irradiated specimens. For the irradiated specimens, the tests were conducted at room temperature and 300°C.

2.6   DEVELOPMENT OF TRANSFORMATION ENHANCED ODS Fe-Cr ALLOYS

D.T. Hoelzer (hoelzerd@ornl.gov)

OBJECTIVE

The objective of this task is to develop two transformation enhanced oxide dispersion strengthened (ODS) Fe-10Cr alloys for fusion reactor applications requiring high-temperature strength and toughness properties and microstructural stability during exposure to energetic neutrons and transmutated He concentrations.

SUMMARY

Two transformation enhanced ODS Fe-10Cr alloys, one with 1%W (wt.%) and the other with no W, were developed to investigate if 1%W had any benefit on the microstructure and mechanical properties. In this study, the creep properties of the two ODS Fe-10Cr alloys were assessed by strain rate jump tensile tests using SS-J3 specimens. Based on the previously obtained tensile properties and the creep properties obtained in this study, it was decided that further alloy development will only occur with the ODS Fe-10Cr alloy containing 1%W.

PROGRESS AND STATUS

The nominal compositions of the two ODS Fe-10Cr alloys are Fe-10Cr-1W-0.3Ti-0.2V (M4) and Fe-10Cr-0.3Ti-0.2V (M5). Both alloys were produced by mechanical alloying with the addition of $0.3Y_2O_3$ (weight %). No W was added to M5 to determine if it has any benefit on the important microstructural features and/or mechanical properties compared to M4 with 1%W. In previous reports, it was shown that the two ODS Fe-10Cr alloys exhibited similar microstructures consisting of ultra-small (<0.5 μm) grains. The tensile properties showed that the 1%W in M4 resulted in a better combination of strength and ductility from 22ºC to 200ºC and better retention of high strength up to 800ºC. M5 showed higher strength at 22ºC to 200ºC, but with poor uniform elongation. Overall, the tensile properties indicated that 1%W addition to M4 improved the balance between strength and ductility from room temperature to 800ºC compared to the W-free M5 alloy.

The creep properties of the two ODS Fe-10Cr alloys were assessed using the strain rate jump tensile (SRJ) test approach at high temperatures. The SRJ tests were conducted with SS-3 tensile specimens that were fabricated from the as-extruded bars of the ODS Fe-10Cr alloys. An Instron 5900R screw driven tensile machine with convection heating in air was used for the SRJ tests. ***Figure 12*** shows the results obtained for M4 and M5 at 700ºC to illustrate the SRJ test. The test begins at the lowest strain rate on the tensile machine and stress is measured. The stress increases with strain until it saturates and does not change with increasing strain. The strain rate is increased and the stress changes in response until it saturates and this procedure is then repeated until the final strain rate is reached that leads to specimen failure. From the comparison of M4 and M5 at 700ºC, both alloys show similar stress levels at the lower strain rates of 2.5 x 10^{-5} s^{-1} and 2.5 x 10^{-4} s^{-1}, but M4 with 1%W shows higher stress level with increased strain rates.
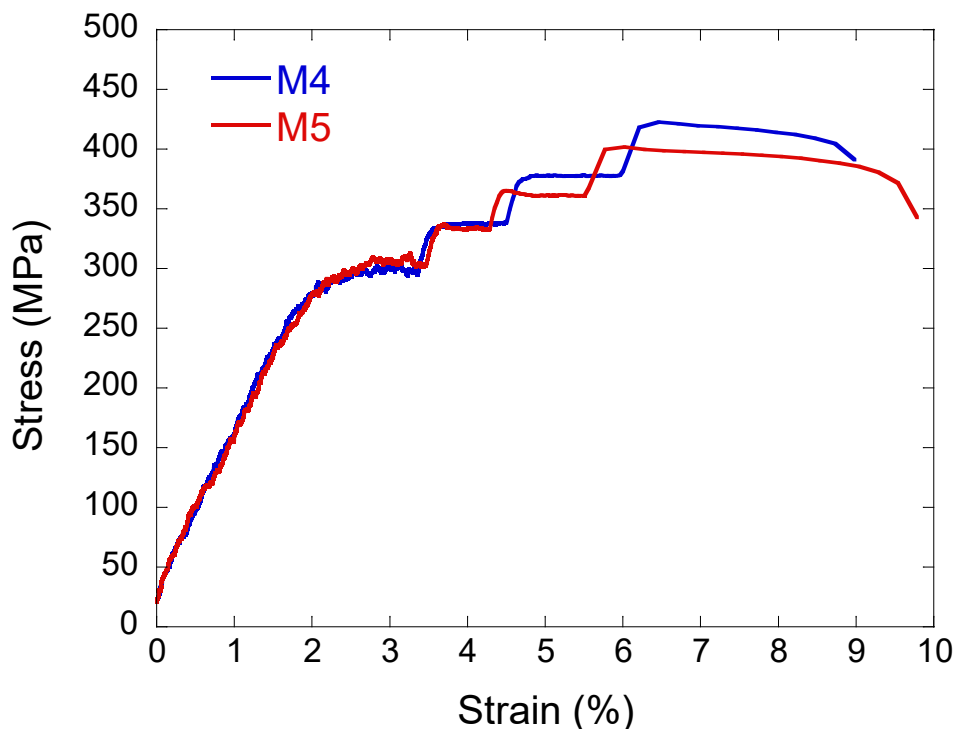
Figure 12. Results of the SRJ tests that were conducted on M4 and M5 at 700ºC.

The results obtained from the SRJ tests for M4 and M5 at 550, 600, 700 and 800ºC are shown in ***Figure 13***. The data is plotted as log strain rate verses log stress with linear line fits. The slope of the lines corresponds to the stress exponent (n), which is:

$$n = \left(\frac{\log \dot{\varepsilon}}{\log \sigma}\right)$$

The results obtained from SRJ tests performed on MA957 are shown in ***Figure 13*** to compare with those of M4 and M5 [1]. The SRJ results showed that the creep properties of M4 (1%W) were superior to that of M5 (0%W) at 550, 600 and 700ºC. M4 showed better creep properties at 800ºC but the specimen failed before reaching the final strain rate. However, the creep properties of M4 and M5 were better than MA957 at elevated temperatures. The calculated stress exponents from the linear line fits of the data shown in ***Figure 13*** are listed in ***Table 2*** for M4, M5 and MA957. The stress exponents for M4 (1%W) and M5 (0%W) are slightly higher than for MA957 but are consistent with the threshold stress creep mechanism that is characteristic of oxide dispersion strengthened alloys.

Like the tensile properties, the creep properties obtained by SRJ tests indicate that the M4 with the 1%W addition is superior to that of M5 with no W. Thus, further alloy development efforts will only involve M4.
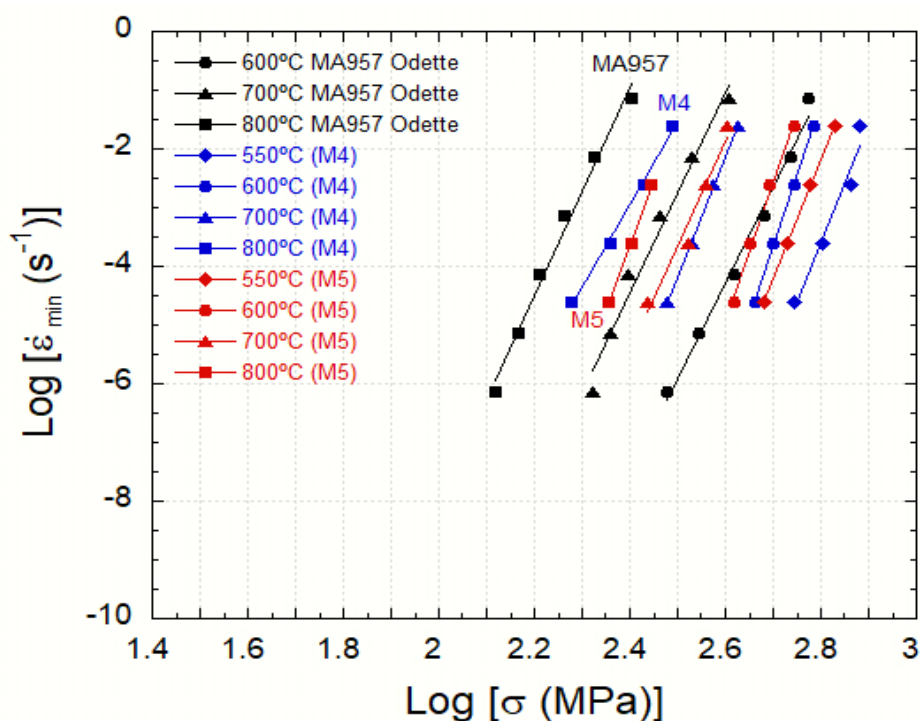
Figure 13. Comparison of creep properties obtained from SRJ tests for M4, M5 and MA957 [1] at elevated temperatures.

Table 2. Calculated stress exponents for M4, M5 and MA957 at elevated temperatures

Temperature	MA957	M4	M5
550ºC	-	20.4	20.4
600ºC	16.3	24.1	23.5
700ºC	16.9	20.3	18.0
800ºC	17.6	14.2	22.1

REFERENCES

[1.] G.R. Odette and T. Yamamoto, NERI Final Report 05-074 (2009).

FUTURE PLANS

The microstructure of M4 will be analyzed using TEM/STEM to investigate the dispersion of Y-Ti-O oxide particles and in-situ high-temperature X-ray diffraction experiments will investigate the transformation kinetics and volume fractions between the bcc-Fe phase that is stable below ~910ºC and the fcc-Fe phase stable above this temperature.

2.7   Fe-Cr-Al ODS ALLOYS FOR FUSION REACTOR APPLICATIONS

Sebastien Dryepondt (dryepondtsn@ornl.gov), Caleb Massey, Phil Edmondson, K.A. Unocic and Ying Zhang

OBJECTIVE

The aim of this project is to develop new oxide dispersion strengthened (ODS) Fe-10/12Cr-5/6Al-0.3Zr + Y_2O_3 alloys containing a high density of nano oxides to enhance the alloy irradiation and creep performance. The formation of an Al-rich scale will also ensure enhanced compatibility with Pb-Li at 600-800ºC.

SUMMARY

The dual coolant lead-lithium (DCLL) blanket concept for DEMO-type fusion reactors requires materials with acceptable Pb-Li compatibility. The Pb-Li capsule and flowing loop tests have demonstrated that alumina-forming alloys offer much better Pb-Li compatibility compared to chromia forming alloys at temperature above ~550ºC due to the formation of a "semi-protective" $LiAlO_2$ oxide layer [1,2].

Oxide dispersion strengthened (ODS) alloys are prime candidate materials for advanced fusion reactor concept operating at temperature >650ºC due to their great irradiation and creep resistance. Also, Al-containing ODS alloys will be required due to their superior Pb-Li compatibility compared to FeCr ODS alloys.

The ORNL has developed several ODS Fe-10/12-Cr-5/6Al-0.3Zr + $0.25Y_2O_3$ alloys and performed tensile, creep and Pb-Li compatibility tests at 700-800ºC to demonstrate the alloys potential for fusion applications [1-4].   In-depth analysis of the processing parameters – microstructure – property relationships was also conducted to optimize the alloy processing route [4,6]. The FY 2019 research was focused on understanding the impact of Zr additions on nano precipitate formation, analysis of creep damage and modification of the fabrication process to improve ODS FeCrAl creep strength while maintaining enough ductility for component fabrication.

PROGRESS AND STATUS

An CM01 or CM08 Zoz Simoloyers were used to ball mill gas atomized Fe-10Cr-6.1Al-0.3Zr (wt.%) powder with nanocrystalline yttria (17-31 nm in diameter) under Ar atmosphere for 40 h. Then 20 g of the ball milled powder was encapsulated in an evacuated (10^{-4} Torr) quartz vial and annealed at 1000°C for 1h (ZY10C60 powder). An 600 g of the same or similar powder was extruded at 900ºC (4H9C), 950ºC(4H95C) or 1000°C (4H10C) after annealing for 1 h using a 2-inch OD mild steel extrusion can.

A two-step extrusion process was also tried using a larger 4-in. OD extrusion can containing ~ 1.5 kg of powder (4H795C). The powder was annealed at 750ºC for two hours followed by an anneal for 30 min at 950ºC and extrusion at the same temperature through a 2x1.5in. rectangular die.

The composition of the ball milled powder and extruded alloys are given in ***Table 3***. The chemical composition of a first generation ODS alloy is also given for comparison. An Fe-12Cr-5Al powder was also balled with a mixture of nanocrystalline yttria and zirconia and then extruded at 950ºC after annealing for 1h at the same temperature using a 4-in. OD extrusion can and a 2x1.5-in. rectangular die.

Table 3. Chemical compositions of powders (at.%) and alloys provided by DIRATS using ICP-OES

Sample	Form	Mill	Fe	Cr	Al	Zr	Y	O	C	N
125YZ	Extruded alloy	CM08	77.84	11.62	9.46	0.17	0.1	0.63	0.11	0.06
ZY10C60	Annealed Powder	CM08	77.42	9.73	11.78	0.15	0.13	0.43	0.25	0.04
4H10C	Extruded Alloy	CM08	78.00	9.55	11.33	0.15	0.12	0.38	0.26	0.12
4H9C	Extruded Alloy	CM01	77.48	9.72	11.58	0.16	0.12	0.42	0.07	0.34
4H795C	Extruded Alloy	CM08	77.66	9.75	11.49	0.16	0.13	0.32	0.25	0.16
4H95C	Extruded Alloy	CM01	77.56	9.67	11.74	0.16	0.12	0.45	0.078	0.2

Characterization of the powder and alloys mainly used atom probe tomography (APT) [7] and scanning or transmission electron microscopy (S/TEM) methods. Tensile and creep testing was performed on subsize SS3-type dog bone specimens 0.76 mm thick for the tensile specimens and 2 mm thick for the creep specimens.

RESULTS

Microstructure characterization

The APT maps of the Z10C60 powder presented in ***Figure 14*** allowed the identification of the various nano-precipitates present in the alloy. In addition to the numerous (Y,Al,O) nano precipitates, ZrC, Zr(N,C) and $(Fe,Cr)_{23}C_6$ larger precipitates were also observed. These results seemed in contradiction with work published by Dou et al. highlighting the presence of trigonal δ-phase $Zr_3Y_4O_{12}$ nano precipitates in an Fe–15Cr–2W–0.1Ti–4Al–0.63Zr–$0.35Y_2O_3$ ODS alloy [8]. Thermodynamic calculations using the CALPHAD approach were conducted to assess the impact of Zr and impurities such as C and N on precipitates formation in 4H10C. ***Figure 15*** shows phase predictions considering two different scenarios i.e. with or without C and N impurities in the alloy.
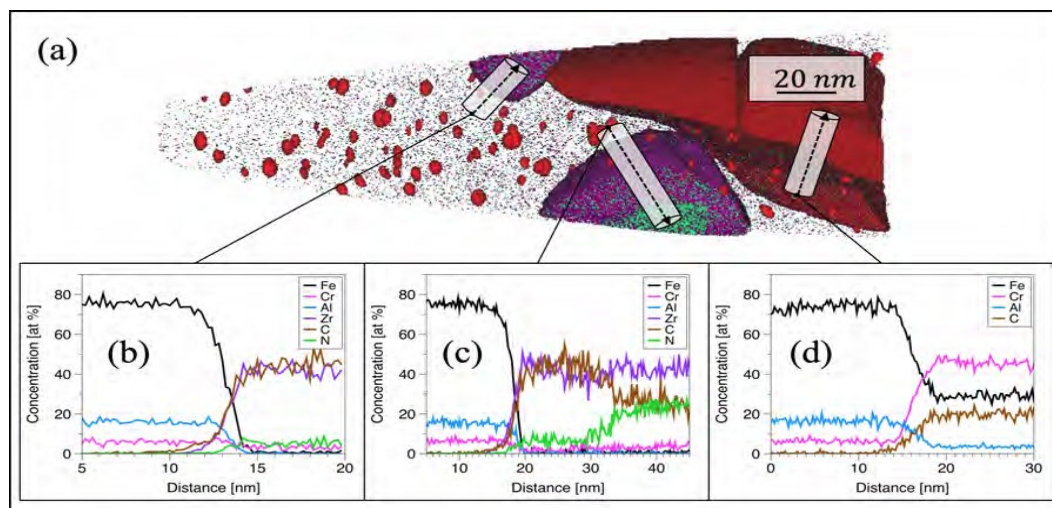
Figure 14. APT control volume of ZY10C60 annealed powder with multiple types of precipitates. Red 1.5 at.% (Y,Al,O) isoconcentration surfaces highlight the smallest precipitate population. In addition, 1D concentration profiles through larger precipitates provide evidence for (b) ZrC, (c) Zr(C,N), and (d) $(Fe,Cr)_{23}C_6$.

Phase predictions with C and N impurities were in good agreement with the experimental results shown in *Figure 14*, but $Zr_3Y_4O_{12}$ was predicted to be the main phase present when C and N were omitted. The C and N concentrations were not specified in Dou et al.'s article but the presence of $Zr_3Y_4O_{12}$ precipitates in their alloy is likely related to lower N and C concentrations compared to 4H10C. These results have been summarized in a paper accepted for publication in Acta Materialia.
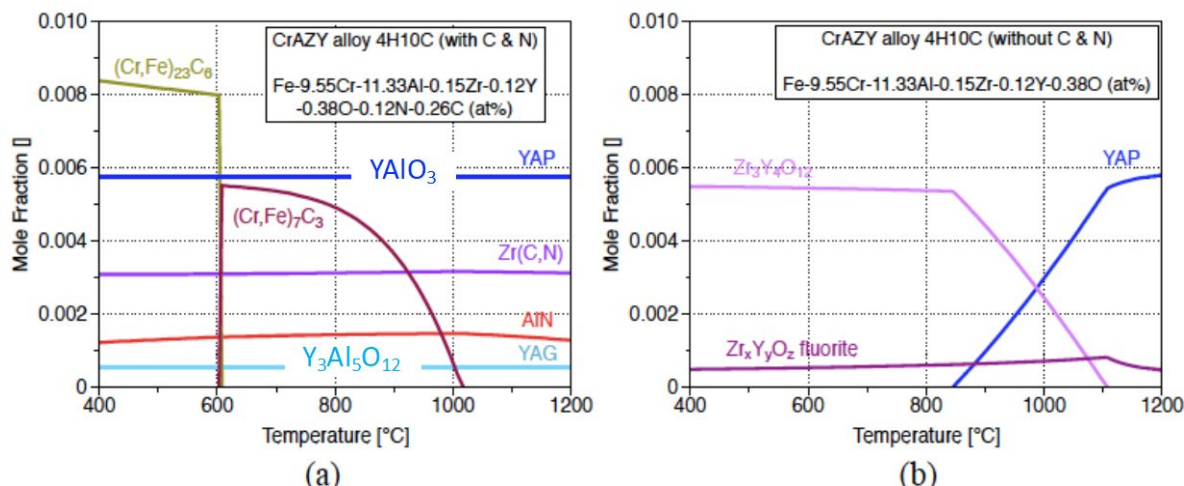
Figure 15. Thermodynamic calculation predicting phases in the 4H10C alloy, (a) with and (b) without C and N impurity elements.

Long-term creep tests

A summary of the long-term creep tests conducted at 700 and 800ºC on the ODS 125YZ and 4H95C alloys are shown in *Figure 16a*, with duration exceeding 25,000 h for tests conducted at 700ºC. All the tests were interrupted before failure for microstructure analysis except for one test conducted on alloy 4H95C at 800ºC, 120 MPa that failed after 1,800 h. Very limited creep data is available for ODS FeCrAl alloys at 700-800ºC but the alloys creep strength is superior to the creep strength of ODS FeCrAlZr alloys fabricated by Kimura et al.[9]. The high number density of nano precipitates shown in *Figure 14* is the likely reason for such good creep performances.

As can be seen in *Figure 16b* and *Figure 16c* microstructure characterization of the 4H95C specimens tested at 700ºC, 140 MPa for 26,700 h and 800ºC, 100 MPa for 6,000 h revealed the presence of numerous creep cavities. These cavities were associated either with clusters of AlN precipitates present in the alloy due the high N content of 4H95C (*Table 3*), or Al_2O_3 stringers. These stringers are believed to form during extrusion due to the thin native oxide scale at the surface of the ball milled powder.
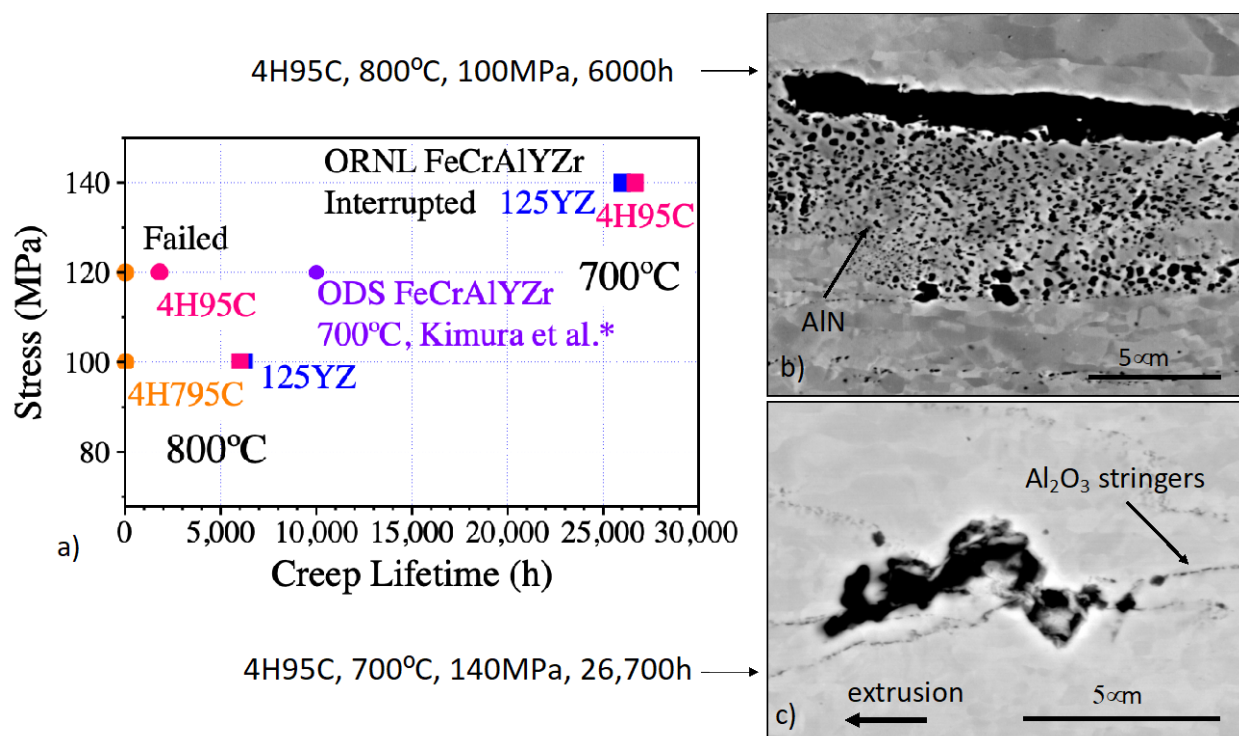
Figure 16. a) Time to rupture for ODS FeCrAlYZr creep specimens tested at 700ºC or 800ºC, b) Scanning electron microscopy (SEM) image of the 4H9C specimen creep tested at 800ºC, 100 MPa for 6,000 h, c) SEM image of the 4H9C specimen creep tested at 700ºC, 140 MPa for 26,700 h.

Two-step extrusion process

A new two-step extrusion process was designed based on the following previous observations:
  - the nano precipitates formed during annealing of the ball milled powder at 650-800ºC
  - coarsening of these precipitates took place at temperature above 1050ºC
  - increasing extrusion temperature led to an increase of the grain size and higher tensile strength but lower ductility

The new 4H795C powder was, therefore, annealed for two hours at 750ºC to nucleate a high number density of nano precipitates, then annealed for 30 min at 950ºC and finally extruded at 950ºC to obtain a good balance between strength and ductility. The yield strength and ductility at 20-800ºC of the new 40H795C are compared in **Figure 17a** with the properties of alloys 4H9C and 4H95C that were annealed for 1h and then extruded at 900C and 950ºC, respectively. Similar yield strengths were measured for the 4H95C and 4H795C but the ductility of alloy 4H795C at T<600ºC was lower than the ductility of both the 4H95C and 4H9C alloys. Creep testing was conducted at 800ºC on the 4H795C, but premature failure was observed at both 120 and 100 MPa (**Figure 16**). As can be seen in **Figure 18**, microstructure examination of the specimen creep tested at 800ºC, 120 MPa revealed again the presence of clusters of AlN precipitates and alumina stringers along the extrusion direction. The AlN clusters were not observed in the 4H95C alloy which likely explains the better ductility of the alloy. A new alloy will be processed with an additional Ar purging step to avoid ingress of air during ball milling. Transfer of the powder from the Simoloyer to the extrusion can will also be conducted in a glove box to control the atmosphere and limit oxidation of the ball milled powder.
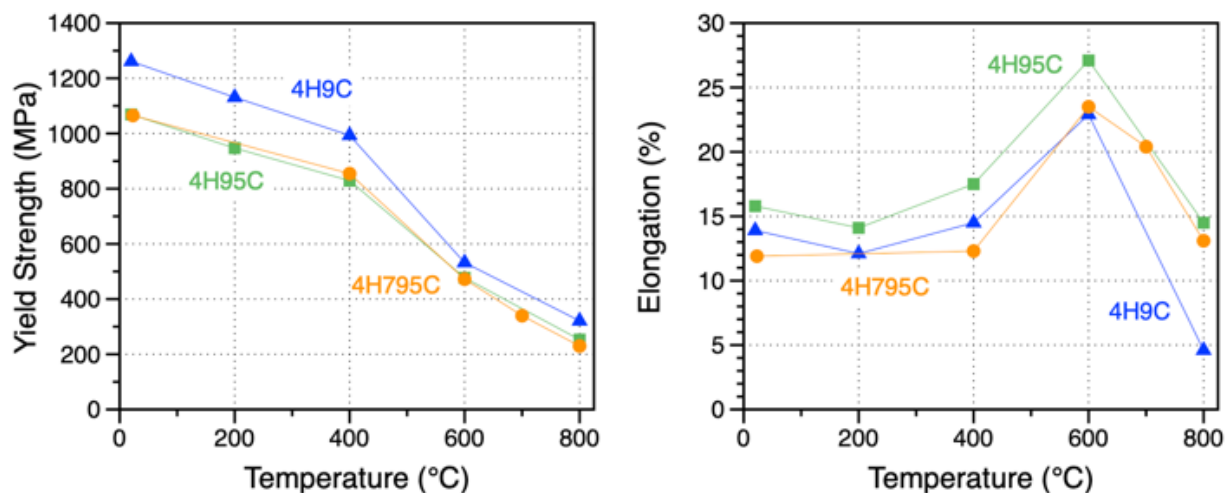
Figure 17. comparison of the tensile properties at 20-800ºC of three ODS FeCrAl alloys annealed and extruded at different temperatures, a) yield strength, b) elongation at rupture.
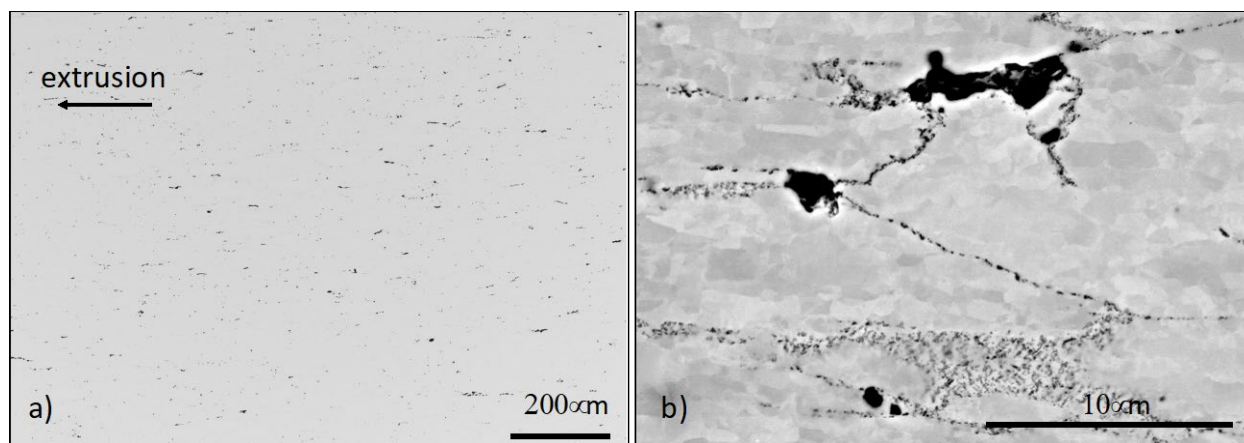
Figure 18. a) Optical and b) SEM pictures of the 4H795C creep specimens tested at 800ºC, 120MPa showing the presence of creep cavities related to alumina stringers and/cluster of AlN precipitates.

FUTURE PLANS

Advanced characterization and thermodynamic calculation were used to explain the formation in ODS FeCrAl alloys of (Y,Al) nano oxides and Zr-rich carbides and carbonitrides. The high number density of (Y,Al) nano oxides led to great long-term creep resistance at 700 and 800ºC. To further improve ODS FeCrAl alloys strength and ductility, additional steps are required to better control powder exposure to air and limit the formation of detrimental AlN clusters and alumina stringers. Additive manufacturing could also be a promising route for the fabrication of complex parts using ODS powders and feasibility study will take place in FY 2020.

REFERENCES
[1.]   K. A. Unocic, and D. T. Hoelzer, *Journal of Nuclear Materials,* 479, 357-364 (2016).
[2.]   J. Jun, K. A. Unocic, M. J. Lance, H. M. Meyer, III, B. A. Pint, *Journal of Nuclear Materials*, in press (2019)
[3.]   B.A. Pint, S. Dryepondt, K.A. Unocic, D.T. Hoelzer, *JOM* 66(12) (2014) 2458-2466

[4.]   K. A. Unocic, B. A. Pint, and D. T. Hoelzer, *Journal of Materials Science*, 51, 9190-9206 (2016).

[5.]   C.P. Massey, S.N. Dryepondt, P.D. Edmondson, K.A. Terrani and S.J. Zinkle, *Journal of Nuclear Materials,* 15, 227-238 (2018).

[6.]   C.P. Massey, S. N. Dryepondt, P.D. Edmondson, M.G. Frith, K C. Littrell, A. Kini, B. Gault, K.A. Terrani, and S.J. Zinkle, *Acta Materialia*, 166, 1-17 (2019).

[7.]   C.M. Parish, N.K. Kumar, L.L. Snead, P.D. Edmondson, K.G. Field, C. Silva, A.M. Williams, K. Linton, K.J. Leonard, *Microscopy and Microanalysis* 21(S3) (2015) 1003-1004

[8.]   P. Dou, A. Kimura, R. Kasada, T. Okuda, M. Inoue, S. Ukai, S. Ohnuki, T. Fujisawa, F. Abe, *Journal of Nuclear Materials*, 444, 441-453 (2014).

[9.]   A. Kimura, R. Kasada, N. Iwata, H. Kishimoto, C.H. Zhang, J. Isselin, P. Dou, J.H. Lee,

[10.] N. Muthukumar, T. Okuda, M. Inoue, S. Ukai, S. Ohnuki, T. Fujisawa, T.F. Abe, *Journal of Nuclear Materials,* 417, 176-179 (2011).

2.8   BAINITIC STEEL DEVELOPMENT FOR FUSION APPLICATIONS

Y. Yamamoto (yamamotoy@ornl.gov)

OBJECTIVE

This work aims to develop new bainitic steels, based on 3Cr-3WV(Ta) steels originally developed at ORNL. The goal is mechanical properties of both base metal and weldments superior to those of existing commercial bainitic steels or ferritic-martensitic (F-M) steels, together with avoiding the requirement for post-weld heat treatment (PWHT). The target applications are high temperature structural components in fusion reactors such as the vacuum vessel, structural ring which supports the blanket modules, and magnet shields, to be used at or above the 400-500ºC range. Improvement of long-term creep properties by introducing additional fine, stable second-phase dispersions, as well as maintaining good weldability, is targeted via optimization of alloy composition and thermo-mechanical heat treatment.

SUMMARY

The alloy design strategy is to balance high hardenability and relatively low hardness in as-normalized condition, targeting reduced property inhomogeneity across the weldment. This has successfully been achieved by compositional modification (high Mn and low C) in both 3Cr-3WV base and 3Cr-3WVTa base bainitic steels. The base metal creep performance as well as the hardness distribution across the weldment met the proposed design targets and criteria. The cross-weld creep performance of the modified steels at 550°C also showed a slight improvement compared to the original steel, but that was not the case at 600°C, indicating that the performance advantages in the modified steel could not be demonstrated in the aggressive, accelerated test conditions. Systematic property evaluations at relatively low temperature range (e.g. 500°C or less) is continuing.

PROGRESS AND STATUS

The calculated continuous cooling transformation (CCT) diagrams of proposed 3Cr-3WV base steels (***Figure 19***, by JMatPro v.9) indicated that the Mn addition (0.4 → 2 wt.%) lowered the bainitic transformation start temperature and the reduced C content (0.10 → 0.05 wt.%) did not change the phase transformation kinetics significantly. The proposed alloy design strategy utilized these characteristics; high Mn addition for high hardenability over a wide range of cooling rate, and low C content for potentially low hardness in the as-normalized condition, compared to the original 3Cr-3WV(Ta) steels. A major target was to lower the hardness at the heat affected zone (HAZ) in the weldment to minimize the cross-weld property inhomogeneity for PWHT-free design and maintain the creep performance though the improved hardenability. The cross-weld hardness distribution shown in ***Figure 20*** clearly demonstrated the controlled hardness of the HAZ in the modified 3Cr-3WV steel with high Mn and low C. The modified steel also showed good impact toughness at room temperature, even in as-normalized condition (Charpy absorbed energy: 123 J/cm^2), suggesting a potentially similar RT toughness of the HAZ in the as-welded condition. The base metal creep performance of the modified steels at 550 and 600°C exhibited creep strengths comparable to the original steels, despite the lower C content in the modified steels (***Figure 21***). The cross-weld creep tests indicated comparable or slightly improved properties in the modified steel at 550°C compared to the original steels, whereas an opposite trend was observed at 600°C. This was hypothetically due to temperature sensitivity of the modified steel mechanical properties, indicating that the creep testing with accelerated conditions (e.g. high temperature and stress) might not be suitable for capturing the advantages of alloy modification.

FUTURE PLANS

Based on these consideration, the property evaluation in a lower temperature range (e.g. 500°C or less) will be systematically conducted to demonstrate the performance advantages of alloy modification in 3Cr-3WV(Ta) base bainitic steels.

Fs: Ferrite start temperature
Ps: Pearlite start temperature
Bs: Bainite start temperature
Bf: Bainite finish temperature

- - - - Fs for original 3Cr-3WV
- - - - Bs for original 3Cr-3WV
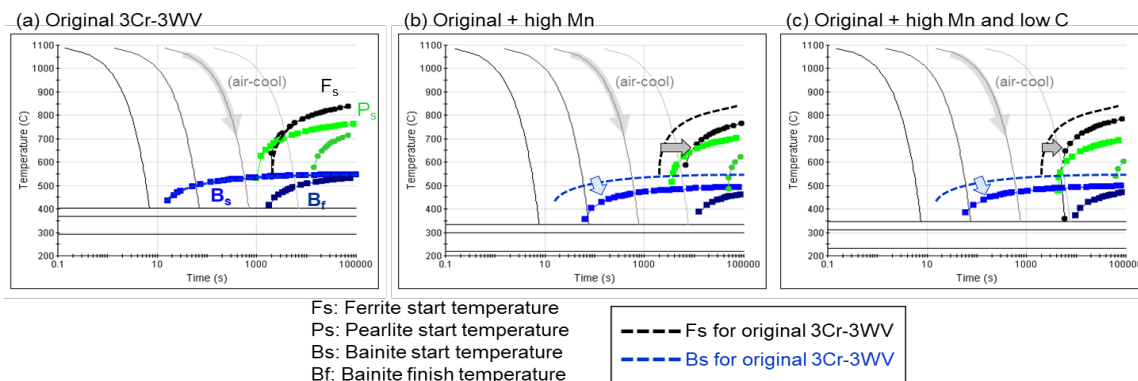
Figure 19. Predicted continuous cooling curves of 3Cr-3WV base steels (calculated by JMatPro v.9).
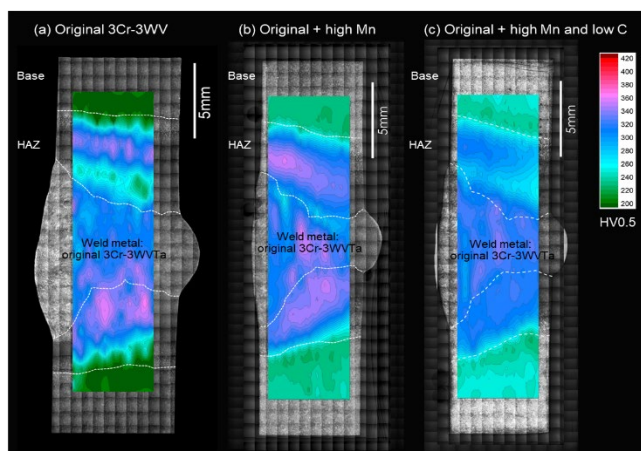
Figure 20. 2D contour map showing Vickers hard hardness distribution across the weld metal in 3Cr-3WV base steels (as-GTAW).
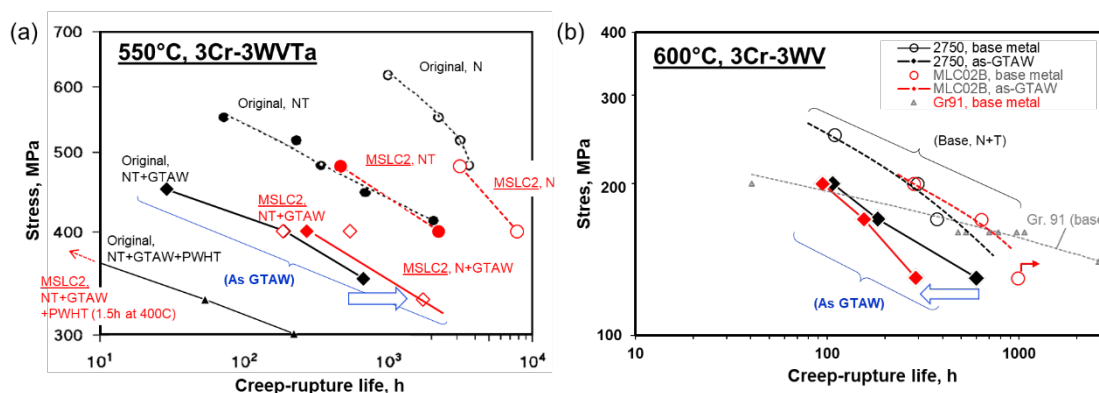
Figure 21. Creep-rupture properties of (a) 3Cr-3WVTa base steels tested at 550°C and (b) 3Cr-3WV base steels tested at 600°C.

2.9   IRRADIATION CREEP OF F82H USING PRESSURIZED TUBES

A.A. Campbell (campbellaa@ornl.gov), Y. Katoh, J.W. Geringer J.D. Reed, K.R. Smith, P.L. Mulligan, M. Ando (QST-Japan)

OBJECTIVE

The objective of this task the determination of neutron induced irradiation creep in reduced activation ferritic martensitic (RAFM) steel alloy F82H at 300°C. The stress necessary to drive irradiation creep was provided using pressurized thin-walled tubes. The internal inert gas pressure induces a hoop stress in the sealed tubes, driving irradiation-induced creep in the tube, which is measured as changes in the tube diameter.

SUMMARY

Four creep capsules designed for a target irradiation temperature of 300°C and hoop stresses of 0, 150, 300, and 380 MPa, were irradiated in the HFIR during cycles 475 and 476. Disassembly and post-irradiation dimensional inspection of the four creep tube samples was completed.

PROGRESS AND STATUS

The neutron irradiation creep of reduced activation ferritic martensitic (RAFM) steels, such as F82H, will be important for the design of fusion reactor blanket systems. This work is redeveloping the capability at ORNL to perform pressurized creep tube (PCT) experiments in HFIR and the capability to measure the creep deformation.

The four capsules completed two irradiation cycles in HFIR ending in December 2017, with a nominal damage level of 3.7 dpa. The capsules were shipped from the HFIR to the Irradiated Materials Examination and Testing (IMET) hot cells facility. The capsule disassembly and post-irradiation exanimation (PIE) was performed in the IMET hot cells.

The capsule disassembly and PIE procedure followed the following steps:
1. Puncture outer capsule housing – determine whether pressurization gas inside the PCTs was retained.
2. Cut open capsule and extract specimen and holder thermometry.
   a. Holder thermometry put aside for shipment to LADMA for analysis.
3. Microscope investigation of PCT outer surfaces, ensure no large visible flaws.
4. Measure outer diameter of PCTs while pressurized, via 2 non-contact techniques.
   a. Laser profilometry using a Beta LaserMike model 162.
   b. Optical imaging with a Celestron hand-held microscope.
5. Cut ends off specimen to release pressurizing gas and extract internal sample thermometry.
   a. Internal sample thermometry put aside for shipment to LADMA for analysis.
6. Remeasure outer diameter of PCTs using same methods as in Step 4.

Two pieces of equipment were designed for this work, the capsule puncture system (Step 1) and a stage for the optical imaging with the hand-held microscope (Step 4b). The capsule puncture system (***Figure 22*a**) is a self-contained pressure vessel that has a puncture tip that puts a hole in the capsule outer aluminum housing and a pressure gauge for measuring if any gas escapes from the capsule. The composite imaging with the microscope (***Figure 22*b**) has an articulating stage that moves the sample a known distance between images and includes a gauge pin and millimeter gauge for calibration.
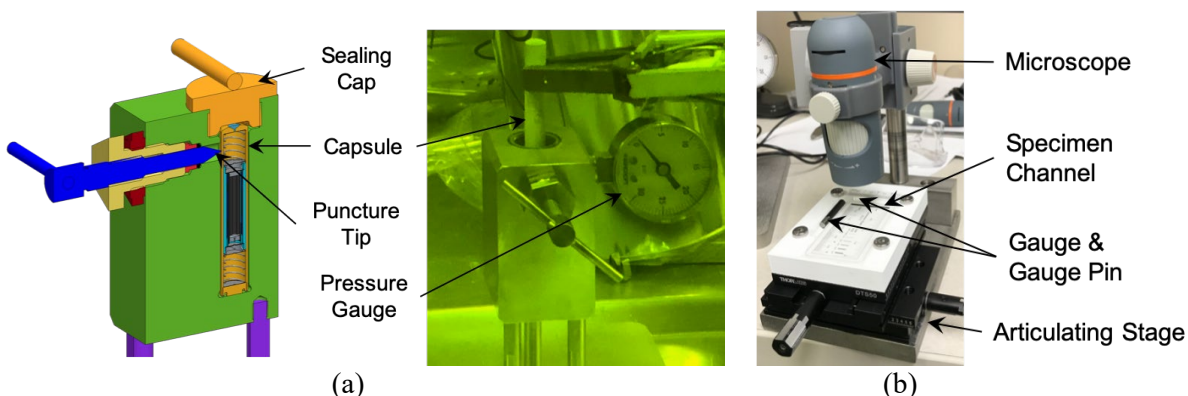
Figure 22. (a) system for puncturing capsule housing. (b) setup for composite optical imaging with a microscope.

The capsule puncture step found that the specimens pressurized at 300 MPa and 380 MPa did not retain their pressurization gas, while the 0 MPa and 150 MPa specimens were still intact. Capsule disassembly for the intact PCTs only required a shake of the capsule to remove the specimens, while the failed PCTs required that the inner V-4Cr-4Ti holder be milled open for PCT extraction. The corrugated aluminum foil between the PCT and the holder (to promote even heat transfer) was easily removed from the intact PCTs, while the foil on the failed specimens required extra work to remove the foil. After capsule disassembly the failed specimens were investigated, which found a rupture in the thin-wall region of the 380 MPa PCT (*Figure 23*), while no such failure indication was observed in the 300 MPa PCT.
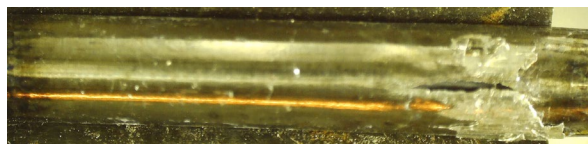
Figure 23. Image of sample pressurized at 380 MPa showing rupture location.

The laser profilometer measurements were performed in the center 15.24 mm (0.6 inches), with a 7.2-degree rotation and a 30.48 μm (0.0012 inch) step between measurements (helical pattern), giving 500 diameter values along the length during 10 total rotations. The value recorded for each point is an average of 2000 measurements with the profilometer at each location/rotation. For the composite imaging 15-20 images were captured along the specimen length and stitched together. Stitching was performed with Adobe Photoshop to retain image resolution.

A jig was developed for cutting the ends off the PCTs that only put gripping force on the ends of the specimens to keep from crimping the thin-walled areas, which would alter the unpressurized dimensional measurements. With this jig the PCT cutting was successfully completed and the internal thermometry was extracted, and dimensional measurements were performed.

The 0 MPa PCT showed 0% creep strain (as expected). The PCT pressurized at 150 MPa showed a creep strain of ~0.18%.

FUTURE PLANS

The future work includes analysis of the thermometry to determine the PCT irradiation temperatures. Additional work including analysis of these results, comparison with historical results, and analysis of the failed PCTs is on-going. Microstructural characterization and other evaluation may follow if warranted by results of the creep measurements.

3.   CERAMIC AND COMPOSITE MATERIALS

3.1   ADVANCED CHARACTERIZATION OF DEFECTS IN IRRADIATED SILICON CARBIDE: HIGH ENERGY XRD

T. Koyanagi (koyangit@ornl.gov), D.J. Sprouster (State University of New York, Stony Brook), Y. Katoh

OBJECTIVE

The goal of this project is to develop advanced characterization techniques for defects in irradiated SiC. High energy x-ray diffraction (XRD) is expected to be useful to nondestructively assess irradiated SiC materials.

SUMMARY

We have employed XRD pair distribution function (PDF) analysis to investigate the structure of polycrystalline β-SiC following neutron irradiation. The structure as a function of irradiation temperature and dose was quantified by analyzing pair distribution functions. Such structural information will be valuable for direct comparison of experimental and simulated atomic structures of irradiated silicon carbide, which will be essential for a predictive model of SiC behavior in fusion reactor environments.

A manuscript based on this study has been accepted in Journal of Nuclear Materials (https://doi.org/10.1016/j.jnucmat.2019.151798).

PROGRESS AND STATUS

The effects of neutron irradiation on the microstructural evolution and the resulting changes in physical and mechanical properties are of critical importance for the development of SiC materials for nuclear fusion applications. This study used β-SiC neutron-irradiated under a wide range of conditions at temperatures between 380 and 1180°C and neutron doses of 0.01to 29 displacements per atom. The effects on the SiC structure were then evaluated using high-energy XRD at Brookhaven National Laboratory.

PDF measurements, which incorporate scattering from both diffuse and Bragg components were conducted to obtain information regarding irradiation-induced atomistic structural changes. The structural information quantified from the analysis of the PDFs shows that the defect populations in neutron irradiated β-SiC affect both the short and medium-range order (***Figure 24***). Larger atomic displacement parameters were quantified for the C sub-lattice, indicating the C sub-lattice preferentially disorders relative to the Si sub-lattice. A dose-dependent decrease in the size of defect free material was also shown by the atomic structure refinements. Finally, evidence of combinations of defects and defect clusters were observable in the PDFs, particularly in the first three correlation peaks.

FUTURE PLANS

Future work will include to exploit how the PDF technique in combination with modeling can allow experimental determination of the defects associated with the observed changes. The PDF analysis will also be applied to SiC irradiated while under applied stresses to help understand irradiation creep.
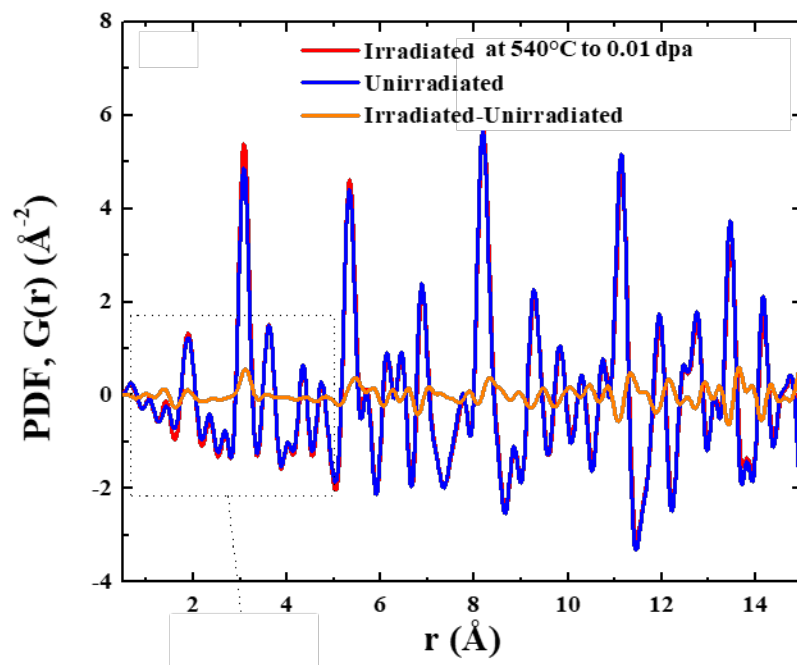
Figure 24. PDF, G(r): number of atoms in a spherical shell at a distance (r) in a β-SiC lattice nonirradiated and neutron irradiated at 540°C to 0.01 dpa. The difference of PDF function before and after irradiation (orange line) identified short range irradiation induced disordering.

3.2   SIC JOINING TECHNOLOGY FOR FUSION REACTOR

T. Koyanagi (koyangit@ornl.gov), Huaxin Li (Hefei University of Technology, China), Xunxiang Hu, and Y. Katoh

OBJECTIVE

The objective of this work is to develop technology to join silicon carbide to other materials for fusion applications. Joining SiC to tungsten (W) was conducted in this task for potential use in fabricating divertor components.

SUMMARY

Successful joining of SiC to W was achieved using the state-of-the-art spark plasma sintering method. The joint microstructure and mechanical properties were characterized in detail. The combination of glow-discharge optical emission spectroscopy (GDOES), transmission electron microscopy (TEM), and transmission Kikuchi diffraction (TKD) revealed limited reaction layers formed during joining. Micro-cantilever tests combined with high-speed nano-indentation revealed robust joint interfacial strength. This work has been published in *Surface & Coatings Technology* 367 (2019) 1–10.

PROGRESS AND STATUS

A W coating on a SiC material can protect the SiC substrate from high surface temperature and erosion due to sputtering when it is used as a divertor structure in a fusion reactor system. To develop joining technology for this application, a W foil/SiC substrate sandwich was joined by the spark plasma sintering method at 1300°C for 10 min under a pressure of 30 MPa. We successfully fabricated the joints shown in ***Figure 25***.

A multiscale experimental characterization was used to fully understand the joint microstructure; a combination of GDOES, TEM + Energy-dispersive X-ray spectroscopy (EDS), scanning electron microscopy + TKD characterization (***Figure 26***) enabled us to identify tungsten silicide (W_5Si_3) and carbide (W_2C) phases in the bonding layer. In addition, micro-cantilever bend tests using a nano-indentation system measured adhesion strength with modulus determined by the high-speed nano-indentation technique. This was used with the corresponding theory or modeling, essential for accurate adhesion strength determination. The average adhesion strength reached was 9.52 ± 2.68 GPa, which reveals that the W/SiC interface formed a robust interfacial bond.

In addition to the successful joining of SiC to W, this study demonstrated a multiscale experimental characterization scheme that will be generally applicable to various costing/substrate systems.

FUTURE PLANS

This study found that spark plasma sintering is potentially useful for joining ceramics materials. Future studies will explore advanced joining technologies using this technique.

Figure 25. Appearance of W-SiC joint specimens.
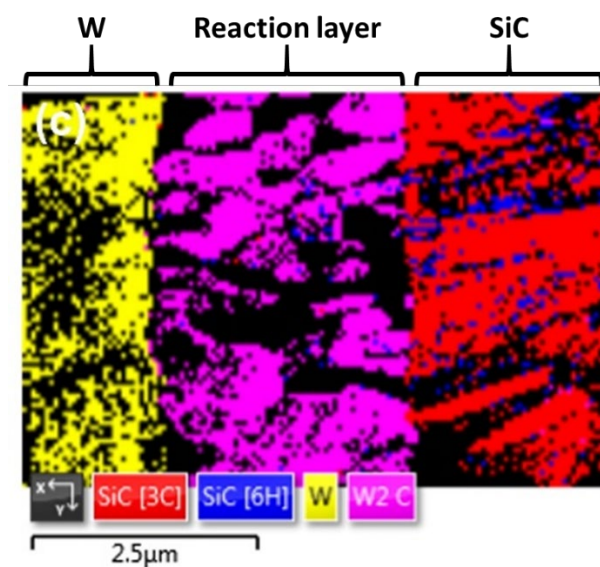
Figure 26. Phase identifications of SiC-W joint system using transmission Kikuchi diffraction. The unidentified phase in the reaction layer was found to be W_5Si_3 based on TEM selected area diffraction pattern analysis.

3.3   EXPLORING ALTERNATE STRUCTURAL CERAMICS

T. Koyanagi (koyangit@ornl.gov), A. Bhattacharya, Y. Katoh, C. Ang (UTK), D. King (Missouri University of Science and Technology [MUST]), G. Hilmas (MUST), W. Fahrenholtz (MUST)

OBJECTIVE

The objective of this task is to explore alternate high-temperature ceramics materials for potential fusion applications. TiB_2 was studied because of its high melting point above 3000°C and high thermal conductivity.

SUMMARY

The response of polycrystalline TiB_2 to neutron irradiation was investigated. The material was fabricated using isotopically enriched ^{11}B powders to minimize helium production via the $^{10}B(n,\alpha)^7Li$ reaction. Neutron irradiation in HFIR was at ~200 and ~600°C to a fast fluence of 2.4×10^{25} n/m^2 (>0.1 MeV). Detailed transmission electron microscopy (TEM) characterizations were conducted to understand radiation damage processes. The limited cavity formation observed highlights the potential for using this type of ceramic material in future fusion reactors. A paper on this study has been published in *Acta Materialia* 165 (2019) 26–39.

PROGRESS AND STATUS

The TiB_2 is an ultra-high temperature ceramic with melting point above 3000°C. Diborides are currently not considered structural materials for nuclear applications because of accumulation of helium from the transmutation reaction of ^{10}B. However, demonstration of the radiation tolerance of TiB_2 made with isotopically separated ^{11}B should result in reconsideration of diborides for use in nuclear structures. For example, diborides could be used as the plasma–facing components of a fusion blanket.

The TEM observations of the neutron irradiated specimens revealed that TiB_2 was susceptible to irradiation damage in terms of dislocation loop formation (***Figure 27***), cavities and anisotropic lattice parameter swelling induced micro-cracking. X-ray diffraction analysis also confirmed the anisotropic lattice distortion (***Figure 27***). At both 220 and 620°C, TEM revealed dislocation loops on basal and prism planes, with nearly two orders of magnitude higher number density of prism-plane loops. Helium generation and temperature rise from residual ^{10}B transmutation caused matrix and grain boundary cavities for the irradiation at 620°C, which was not as significant as seen in TiB_2 without isotope control.

FUTURE PLANS

Response of another ultra-high temperature ceramic with isotope control ($Zr^{11}B_2$) to neutron irradiation will be investigated.
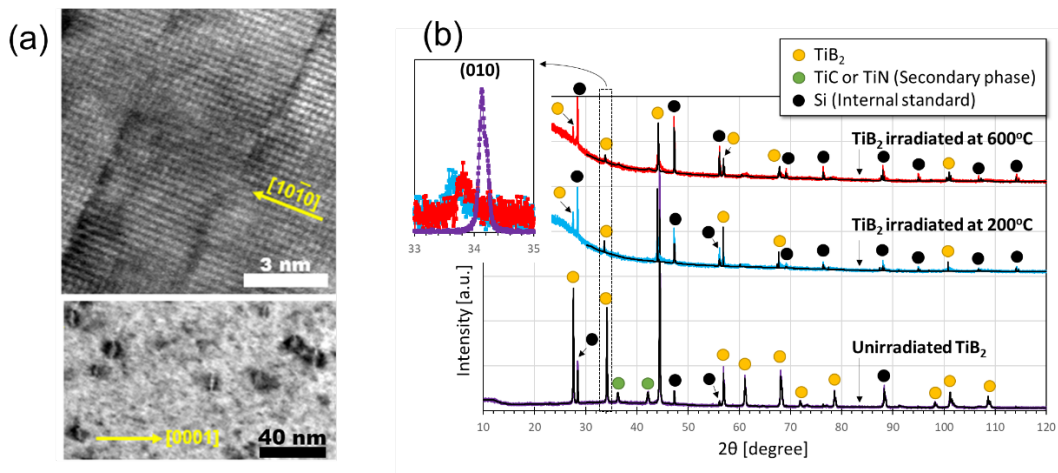
Figure 27. (a) Atomic scale views of irradiation-induced defects in TiB$_2$ after irradiation at ~200°C and (b) x-ray diffraction spectra of unirradiated and irradiated TiB^2.

4.   HIGH HEAT FLUX AND PLASMA FACING MATERIALS

4.1   MECHANICAL PROPERTIES OF IRRADIATED TUNGSTEN – PHENIX COLLABORATION

L. M. Garrison (garrisonlm@ornl.gov), J. Echols, N. Reid, T. Miyazawa, C. Lin, Y. Katoh

OBJECTIVE

The PHENIX collaboration is directed at expanding the database on neutron irradiation effects in tungsten materials. This task is evaluating the effects of irradiation on the mechanical properties.

SUMMARY

The HFIR RB*19J irradiation capsule included over 20 varieties of tungsten for the PHENIX collaboration in three temperature zones, nominally 500, 700, and 900°C. Hardness and tensile tests have been completed on all samples. A new alumina fixture was designed and deployed for tensile testing at 900°C. Fracture surface analysis has been completed on most samples.

PROGRESS AND STATUS

The HFIR RB*19J irradiation capsule used a gadolinium sleeve to reduce the thermal neutron flux on the samples, thereby reducing the transmutation of W to Re and Os. This reduction in transmutation did not have a significant effect on the hardness measured after irradiation (***Figure 28***).
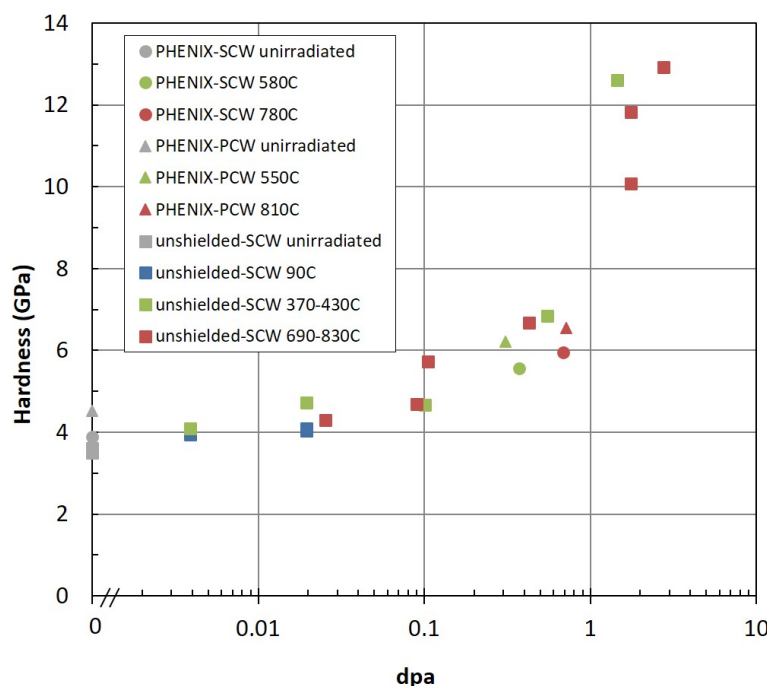
Figure 28. Hardness data for tungsten irradiated in a thermal neutron shielded HFIR capsule compared with data from previous unshielded irradiations of tungsten. Reproduced from L. M. Garrison, et al. "PHENIX US-Japan Collaboration Investigation of Thermal and Mechanical Properties of Thermal Neutron Shielded Irradiated Tungsten," Fusion Science and Technology, 75, 6 (2019) 499-509.

Fifteen types of tungsten have been tensile tested before and after irradiation at ~500, ~700, and ~900°C for a total of approximately 90 data points. Tests were conducted in a vacuum tensile test frame at an extension rate of 0.5 mm/min. Tests conducted at 500 and 700°C used an Inconel fixture. A new alumina fixture was designed for tests at 900°C and will allow future tests at higher temperatures. Example fracture surfaces of thick plate tungsten produced by ALMT are shown in ***Figure 29***. The thick plate tungsten material has anisotropic grains, so samples were machined in three different directions, called A, B, and C. The A direction shows horizontal elongation of the grains on the fracture surface after irradiation and testing at ~500°C, but after irradiation and testing at 900°C the grains appear to have recrystallized. The C direction tensile samples of the thick plate tungsten have grains that appear elongated vertically on the fracture surface, and both temperatures of irradiation and testing resulted in significant necking of the material. Despite the difference in their fracture surfaces, the tensile curves of the A and C direction material have the same trends at 500°C and 900°C, with no strain hardening at 500°C, and both showing strain hardening at 900°C. Stress- strain curves for the tests at 500°C are shown in ***Figure 30***. Tensile and fracture results on the rest of the 90 samples are being analyzed and compared to generate information on the tungsten mechanical properties and the dependence on grain size and shape.
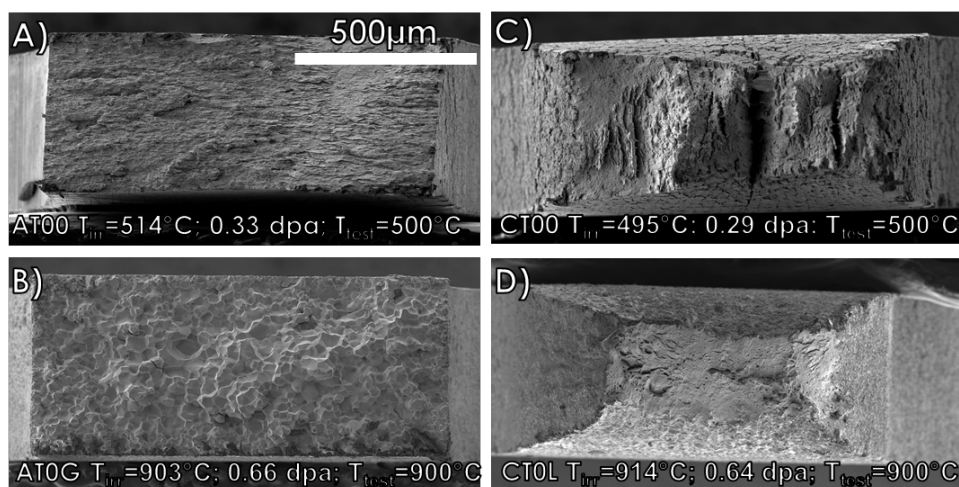
Figure 29. Fracture surfaces of thick plate tungsten cut from the same original block in either the (a)-(b) A direction or the (c)-(d) C direction.
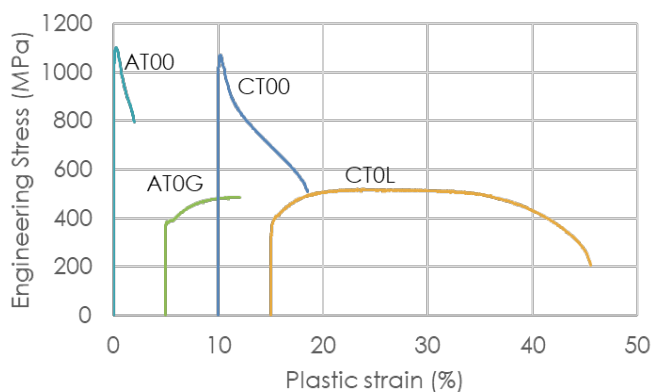
Figure 30. Tensile curves show no strain hardening for the thick plate tungsten tested at 500°C (AT00 and CT00) but a different curve shape for those tested at 900°C (AT0G and CT0L). Irradiation conditions as shown in Figure 29.

**4.2   THERMAL PROPERTIES OF NEUTRON IRRADIATED TUNGSTEN MATERIALS -
          PHENIX COLLABORATION**

*L. M. Garrison (garrisonlm@ornl.gov), J. Echols, S. Curlin, H. Wang, M. Akiyoshi (Osaka University,
Japan), S. Copp (University of Tennessee)*

OBJECTIVE

The PHENIX collaboration is directed at expanding the database on neutron irradiation effects in tungsten
materials. This task is evaluating the effects of irradiation on the thermal properties.

SUMMARY

The LFA467 thermal diffusivity instrument is being prepared for testing by several benchmark tests. The
instrument can measure thermal diffusivity on samples as thin as 0.5 mm, but much fine tuning of the
settings is required to get repeatable and accurate results. A set of unirradiated samples of different sizes
cut from the same source material are being used to establish parameters for reliable testing of different
sample geometries. Once this is established, the testing will continue on the irradiated tungsten samples
from the HFIR RB* 19J capsule.

PROGRESS AND STATUS

The LFA467 uses a quick laser pulse on one face of the sample and uses a detector to measure the
temperature difference on the opposite face. It has four heated chambers, but only two have the proper
temperature control. The LFA467 was chosen over the LFA457 instrument because it has a faster pulse
and a better vacuum system. Tungsten is sensitive to small concentrations of oxygen in the environment
at elevated temperature and significant oxidation was observed in the LFA457 starting around 400°C.
Initial tests in the LFA 467 also had oxidation, so improvements were made to the gas input and vacuum
lines. Now, tests have been completed to 800°C in the LFA467 without noticeable oxidation.

Sample Size Testing

Before any other tests are conducted, a size effect study must be completed for the tungsten specimen
geometries used in these irradiation experiments. Eight samples of unirradiated tungsten of various
diameters and thicknesses were cut from a single block of Alfa Aesar brand unalloyed tungsten.
Measurements were made on samples of each geometry listed in *Table 4*. The data points should all fall
on the same curve in the thermal diffusivity vs. temperature graph. It is critical that the data being
collected in this first step is consistent for all sizes and shapes of the sample being tested before we move
to the irradiated material. Samples will be tested from room temperature to a maximum temperature of
800ºC in 50ºC increments using the LFA467 device.

To date, six of the eight samples from *Table 4* have been measured (*Figure 31*). The thermal diffusivity
values of the samples are similar, except for sample D6T.5. However, the procedure used to collect the
data in *Figure 31* is not yet optimized or repeatable. The LFA 467 does not have built in settings for
samples that are 0.5 mm thick or for non-round samples. There are many options that can be tuned
including the pulse width and half time, so these must be adjusted to find the accurate settings for each
geometry. A set of parameters specific to each sample geometry is being developed. Once these
parameters are finalized, the tests on the irradiated samples will proceed with confidence.

Table 4. Unirradiated Alfa Aesar manufactured unalloyed tungsten samples used for size effect study

Sample Type	Sample Diameter	Sample Thickness
Tensile Bar	n/a	0.5 mm
Disk	3 mm	0.5 mm
Disk	3 mm	1 mm
Disk	6 mm	0.5 mm
Disk	6 mm	1 mm
Disk	6 mm	2 mm
Disk	12.7 mm	2 mm
Disk	10 mm	1 mm
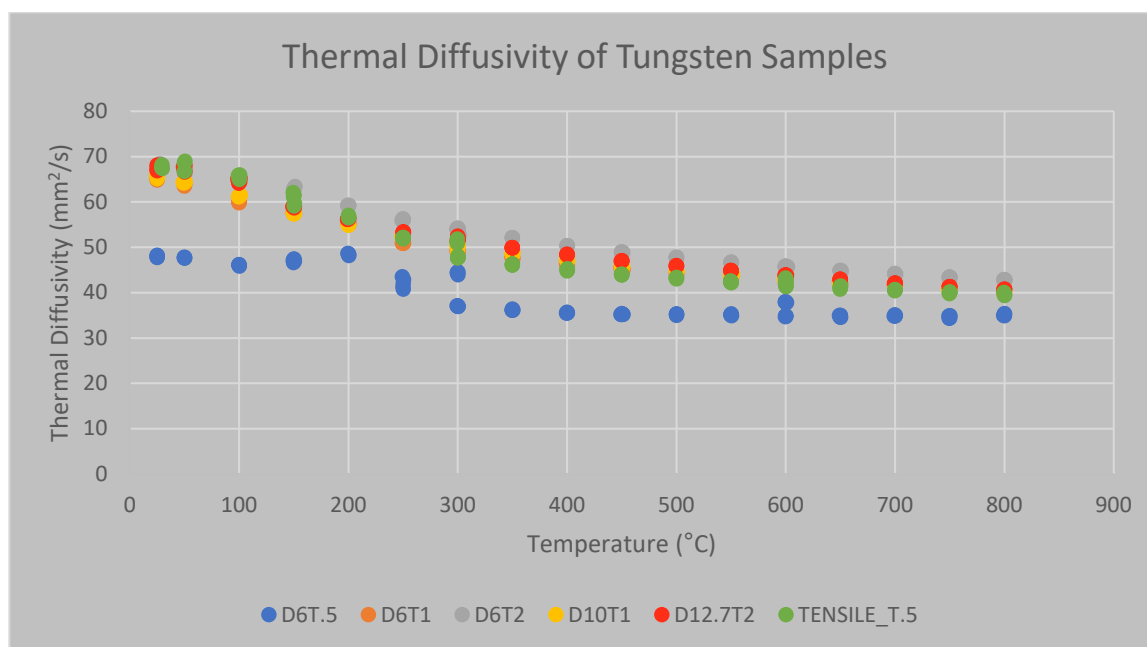
Figure 31. Thermal diffusivity data for six of the eight sample geometries listed in Table 4. The legend at the bottom of the graph lists first the diameter followed by the thickness of the sample.

4.3   EFFECT OF IRRADIATION ON THE ELECTRICAL RESISTIVITY OF TUNGSTEN MATERIALS - PHENIX COLLABORATION

J. R. Echols (echolsjr@ornl.gov), L. M. Garrison

OBJECTIVE

The PHENIX collaboration is directed at expanding the database on neutron irradiation effects in tungsten materials. This task is evaluating the effects of irradiation on the electrical resistivity.

SUMMARY

Two new fixtures were developed for measuring the electrical conductivity of miniaturized tensile samples and 3 mm disks. Testing has been performed for a range of tungsten samples as part of the PHENIX collaboration on irradiation effects.

PROGRESS AND STATUS

The high thermal conductivity of tungsten is critical for its use in future fusion reactors and is one of the reasons tungsten is the leading candidate material for high heat flux regions of reactors. However, neutron irradiation in a reactor environment degrades its thermal conductivity. To separate the phonon, electron, and transmutant element contributions to tungsten thermal conductivity, electrical conductivity measurements need to be compared against thermal conductivity measurements.

The US-Japan collaboration, PHENIX, has a goal of investigating tungsten and tungsten-based materials response to neutron irradiation for use in future fusion reactors. To this end, the PHENIX collaboration exposed over 1500 single crystal, polycrystalline, and W-Re alloy samples in the RB*19J irradiation capsule in the High Flux Isotope Reactor (HFIR) to doses of ~0.2-0.7 dpa. Nominal irradiation temperatures were 500, 800 and 1200°C. Evaluation of the SiC temperature monitors contained in the subcapsules indicated actual irradiation temperature ranges in the three subcapsules of 430-670, 740-960, and 880-1080°C. A gadolinium shield was included in the irradiation capsule to reduce the thermal neutron flux and therefore the rate of W to Re,Os transmutations.

The HFIR capsule geometry and radioactivity levels of the irradiated samples severely limit the size of the samples which can be used. Therefore, to measure the electrical conductivity of the irradiated samples, two different miniature electrical resistivity fixtures were designed and constructed: one for 3 mm diameter disks and one for SSJ tensile specimens. These fixtures are shown in **Figure 32**. The electrical resistance measurement system utilizes a Keithley Model 182 Sensitive Digital Voltmeter to measure the voltage drop across the inner lead, a Model 237 High Voltage Source Measure Unit which provides the current, along with the custom fixtures. The system has been constructed, tested and calibrated using high purity W and Cu standards. Pre-calibration electrical resistivities are within 1% of literature values in both cases Resistivity measurements were made at room temperature, between 20°C and 24°C. Resistivity values were then normalized to 20°C for comparison.

During resistivity testing, it was noted that sample surfaces from the 880-1080°C zone were discolored by an opaque film. Measuring the resistivity of the samples before and after removing the film confirmed that this film would give inaccurately high results, as shown in **Figure 33**. Therefore, all samples from this zone must first be polished on one side before testing.

Resistivity over the range of pure W samples shows clustering correlated with irradiation temperature, with samples from the 880-1080°C zone possessing the least amount of degeneration, as shown in **Figure**

33. The large spread in resistivity observed in the irradiated samples from the 430-670°C zone is unexpected. The results which are least tightly grouped are all from polycrystalline samples. It is possible that grain boundaries may play a surprisingly large role in the post-irradiation electrical resistivity and more work will be done to investigate this possibility.

FUTURE PLANS

Testing is still underway to acquire resistivity data from the entire set of samples from the PHENIX collaboration. Comparisons to transmutation, microstructure, thermal conductivity will be made in the future to investigate their relationship to the electrical resistivity.
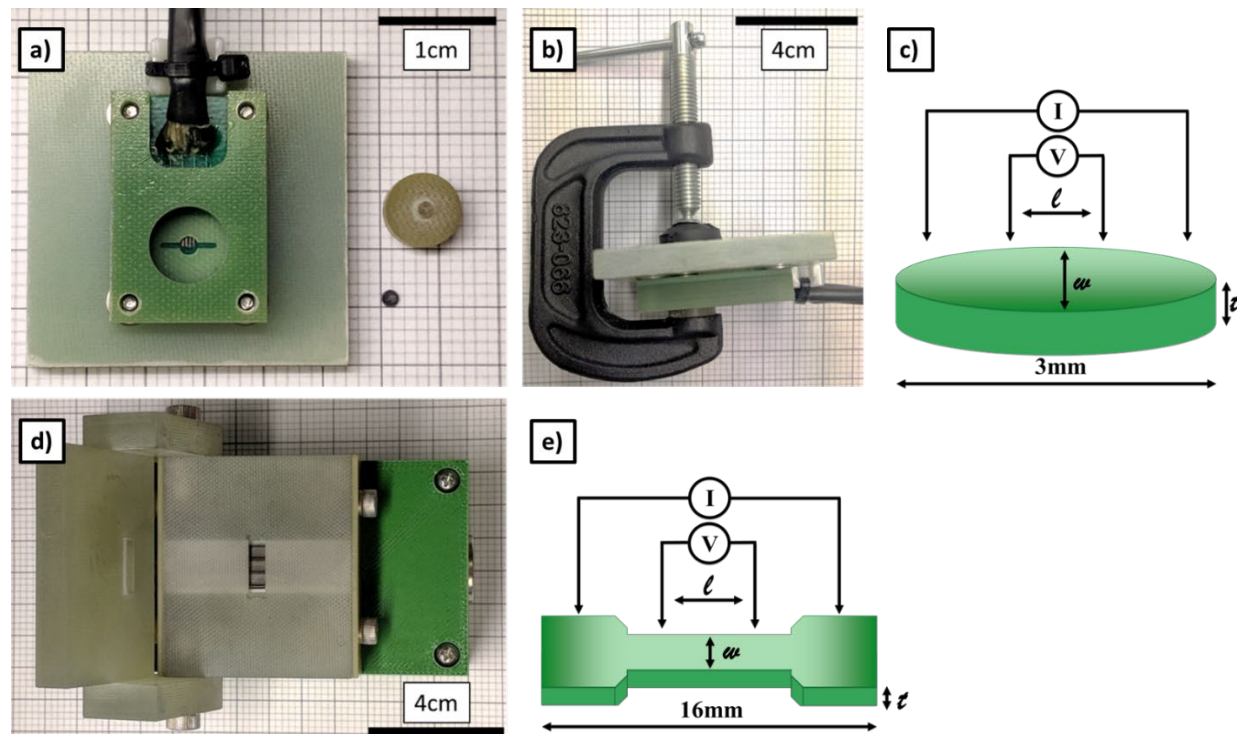
Figure 32. Electrical resistivity testing apparatuses. For each image, major gridlines are 1 cm apart. a) Disassembled 3 mm disk holder. Apparatus on left, example 3 mm disk and plug on right. b) Assembled 3 mm disk fixture. The plug is clamped to the apparatus to ensure proper contact with the pins. c) Simplified 3 mm disk circuit schematic. d) Tensile bar fixture. e) Simplified tensile specimen circuit schematic. Circuit schematics show length (l), width (w), and thicknesses (t) used in resistivity calculation.
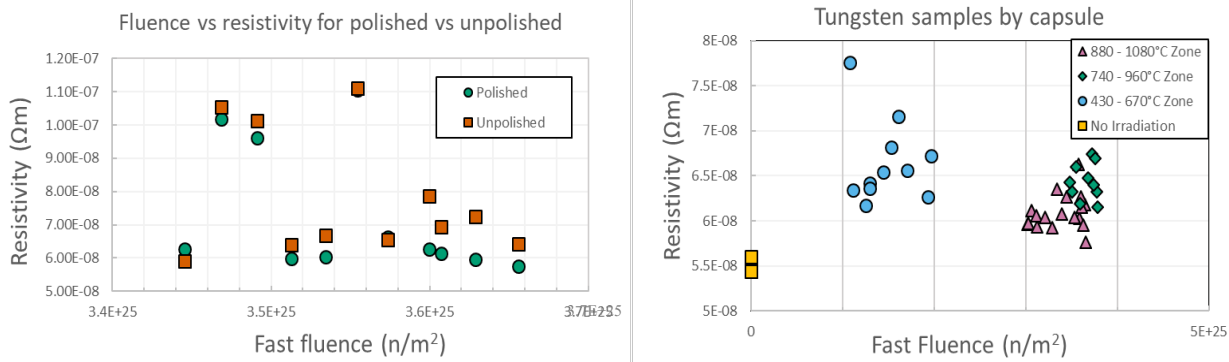
Figure 33. Resistivity vs fast neutron fluence, for measurements taken between 20°C and 24°C and normalized to 20°C. The polished vs unpolished data on the left shows the importance of removing the thin film apparent on samples from the 880-1080°C zone. The clustering of measured tungsten resistivity by zone (and thus irradiation temperature) on the right highlights the three distinct regions of resistivity change resulting from the different irradiation temperatures.

4.4 ELEMENTAL CHARACTERIZATION OF NEUTRON IRRADIATED TUNGSTEN USING THE GD-OES TECHNIQUE

L. M. Garrison (garrisonlm@ornl.gov), N. Reid

OBJECTIVE

The aim of this work is to analyze impurities, alloying elements, and transmutation elements in neutron irradiated tungsten using the GD-OES technique to better understand tungsten evolution in a fusion environment.

SUMMARY

The glow discharge optical emission spectroscopy (GD-OES) technique can analyze the elemental composition of materials with depth resolution. It was used to measure transmutation products Re and Os in W as well as other impurities. A mounting system was designed and machined to prepare this technique for irradiated tungsten samples. The system was calibrated and use in pulsed versus continuous mode was investigated. With this preparation complete, the technique will be used on the irradiated tungsten materials of the PHENIX collaboration.

PROGRESS AND STATUS

The GD-OES technique sputters material from the surface of a sample, ionizes the eroded material, and identifies elements from the optical emission of the excited atoms. It is well suited to characterizing irradiated samples because the signal does not depend on the isotope (as in mass-based measurements) and it can analyze a relatively large region (compared to microscope-based techniques). A recently designed sample mounting system with the GD Profiler 2 instrument is used for measurements on 6 mm discs and the tab ends of tensile specimens.

Reliable information from GD-OES measurements requires calibration with known standards. A set of W-Re alloy standards were fabricated, listed in *Table 5*. The compositions of "ITERW10" and "WRE1" were measured with ICP-OES to confirm their compositions; WRE3 and WRE5 composition is estimated from the fabrication process and will be confirmed with ICP-OES. These alloys were used for the calibration of the GD-OES instrument (*Figure 34*). The matrix W composition calculated from the calibration does not yield a linear fit to the known compositions (*Figure 34*a). The Re concentration from the calibration step does yield a linear fit for the low concentration alloys, but the WRE5 with approximately 17.7% Re lies above the line. These alloys did not contain additions of Os, so the small Os signal intensity, between ~0.015 and 0.035 V is mapped to a concentration of zero.

Table 5. Composition of W-Re alloys used for calibrating the GD-OES

Material Name	Re wt%
ITERW10	0.5 wppm
WRE1	0.41
WRE3	0.83
WRE5	17.7
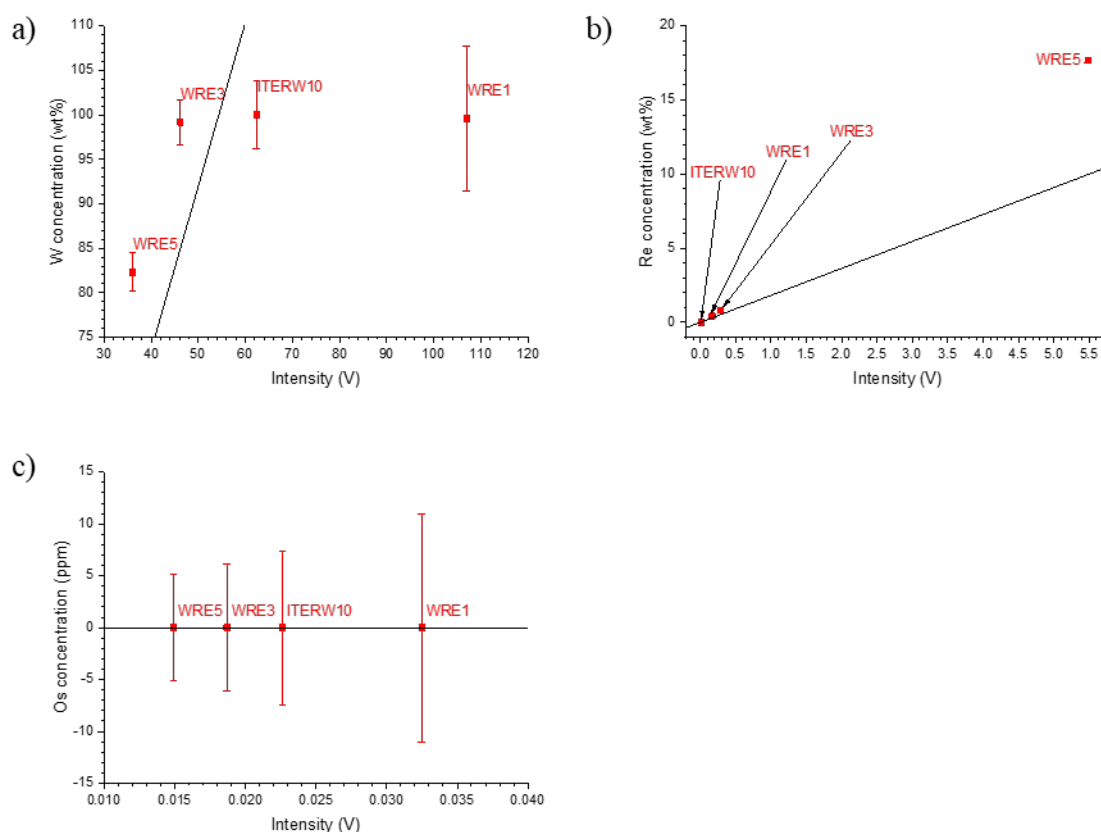
Figure 34. a) W, b) Re, and c) Os calibration curves for the GD-ODS signal using a continuous rf plasma measurement. W-Re-Os alloys will be used for calibration of Os in future work, as well as alloys with concentrations in the middle range of 1-15 wt%. With more standard materials used, higher-order polynomial calibration fits will be obtained, statistical and propagation error reduced, and with less contribution from statistical outliers.

The W and Re measured signals shown in *Figure 35* demonstrate two different rf sputtering modes that GD-OES can perform. The rf plasma can be run continuously (normal) or pulsed at a user-specified frequency and duty cycle. The advantages of the plasma pulsed mode are that the sputtering of the surface is at a controlled rate and allows sputtered atoms to be pumped away between pulses, as well as preventing certain other artifacts such as self-absorption. The sacrifice of running in a pulsed mode is that less light is emitted from the sample as the frequency is reduced, degrading the measurement sensitivity. Pulse mode sputtering also requires the user to specify the rf capacitance beforehand, which may lead to higher reflected rf power and thus less light emission and degraded sensitivity. Any changes in the rf parameters creates a plasma with different properties, and hence recalibration is needed when the pulse frequency, duty cycle, power, or ambient gas pressure is changed. The pulsed mode was calibrated only for the unalloyed W sample and WRE5, producing a larger error band but resulting in much less noise in the data (*Figure 35*). More standards can be calibrated to give a transition from pulsed to normal without any breaks.

The pulsing conditions of 100 Hz at a 0.5 duty cycle are preferred for measurement of transmutation elements in irradiated tungsten samples from the PHENIX collaboration. Calibration will include a enough set of Re and Os concentrations on the calibration curve ranging from ppm amounts to near the

solubility limits of these elements in W. The radioactive samples will be affixed to aluminum substrates and centered to achieve the required vacuum-tight assembly for the measurements.
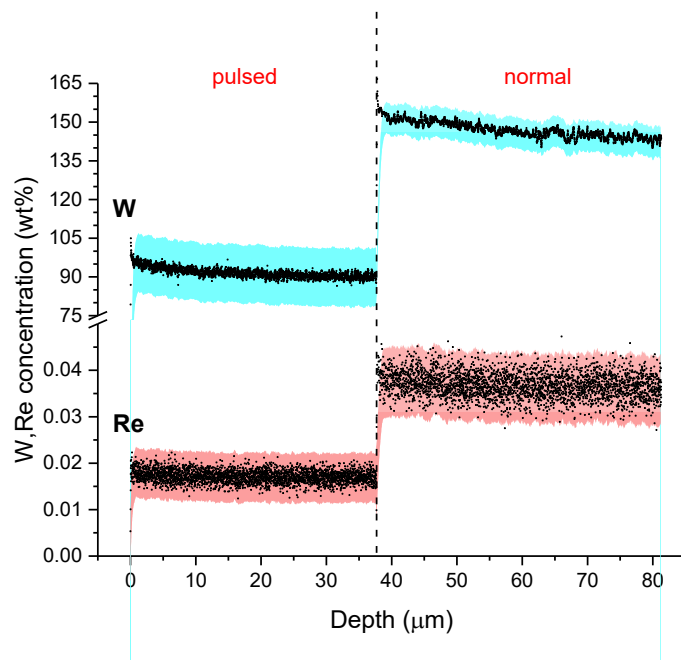
Figure 35. GD-OES signals for pulsed and continuous rf sputtering of an unalloyed W sample done in series to obtain a concentration depth profile. Sputtering rate can be controlled to get surface-sensitive quantification. The radiofrequency) source was pulsed at 100 Hz for 5 min and then run continuously for 5 min. Both sputtering methods require independent calibration.

4.5   MODELING THE MECHANICAL PROPERTIES OF TUNGSTEN COMPOSITES

L. M. Garrison (garrisonlm@ornl.gov), N. Jensen, J. Blanchard (University of Wisconsin-Madison)

OBJECTIVE

The objective of this project is to perform a finite element analysis of tensile tests of tungsten composites to understand and optimize the experimentally measured properties.

SUMMARY

Tungsten laminate composites have been simulated using the finite element modeling program ANSYS. Individual tungsten and steel foils were modeled under tension and compared to the tungsten-steel laminate results. The boundary conditions have been set to require no slipping between layers, so the resulting stress in the tungsten layers is higher than the steel layers. Comparisons are being completed between the model and experimental results.

PROGRESS AND STATUS

Tungsten composites have been fabricated and experimentally tested in tension under several conditions relevant to fusion, including neutron irradiation and high heat flux. While the composites show some benefit compared to tungsten alone, there is a lack of understanding of the deformation mechanisms of the composites and of how to optimize the composite designs. By modeling the composites, variations of layers and materials can be more easily evaluated; favored geometries can then be fabricated and experimentally tested. This modeling will also allow deeper understanding of the deformation mechanisms active in the composites.

This ANSYS model was used for the SSJ2 geometry tensile specimen with round, perfectly stiff cylinders to apply pressure to the shoulders of the specimen (***Figure 36***). The composite modeled here has three tungsten layers and two steel layers, each 0.1 mm thick for a total thickness of 0.5 mm. Each layer is modeled individually in ANSYS and perfect bonding was selected as a boundary condition between the layers, so no sliding or delamination is allowed. Because no movement between layers is allowed, the resulting strain is equal across all layers (***Figure 37***). Future simulations could use a friction coefficient between layers. Mechanical properties from experimental tensile tests of individual steel and tungsten foils were used as the input to the simulations. Because tungsten has the higher Young's modulus, when the tungsten and steel layers are constrained to have equal strains, the tungsten layers have higher stress values (***Figure 38***). The model results are being compared with experimental results for verification. Future work will explore different layer thicknesses and composite interlayer materials.
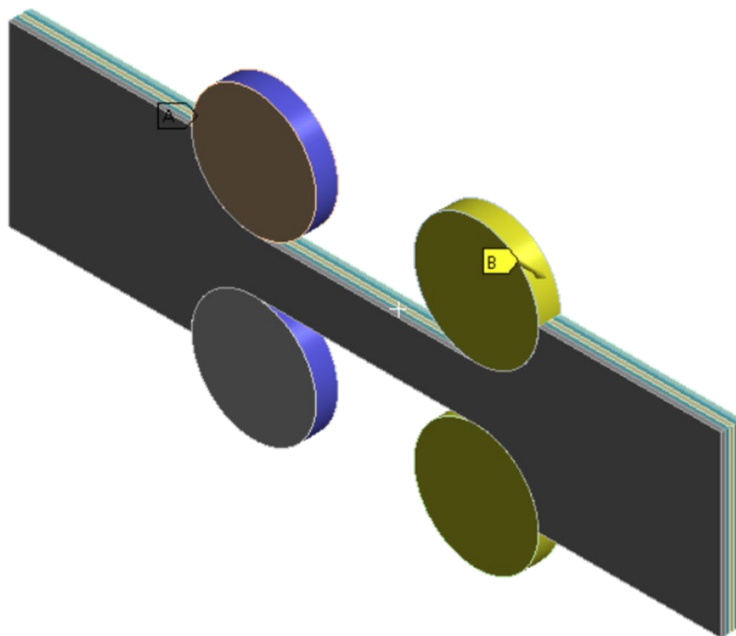
Figure 36. The SSJ2 tensile specimen viewed on an angle. The blue cylinders are fixed in space while a velocity is applied to the yellow cylinders to simulate the tensile test.
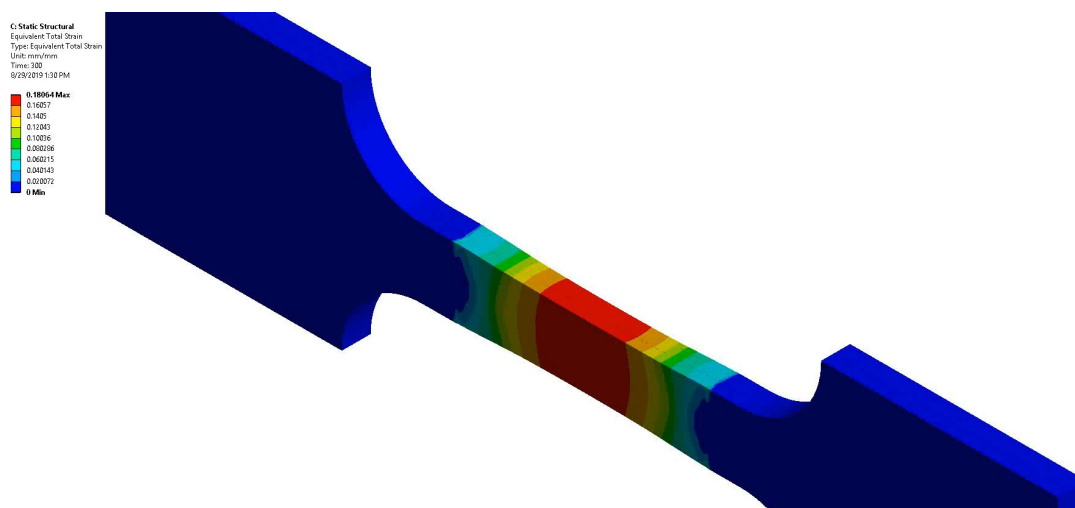
Figure 37. Colors indicate strain with red being highest and blue lowest. This simulation used applied motion (cross-head spead) of 0.1 mm/min.
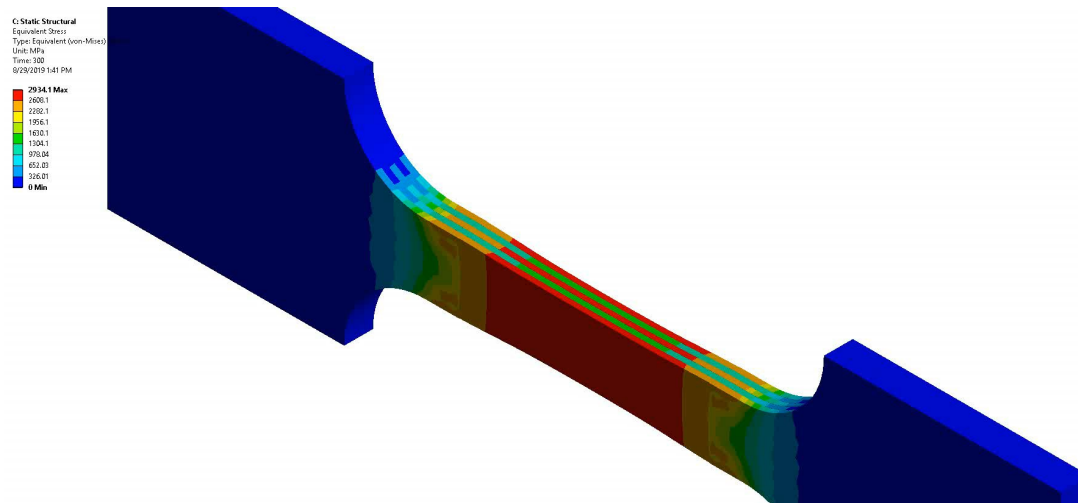
Figure 38. Equivalent stress is indicated by the color scale. The three tungsten layers have higher stress than the two steel layers, due to differences in Young's modulus.

5.   PLASMA MATERIALS INTERACTIONS

5.1   DAMAGE-MECHANISM INTERACTIONS AT THE PLASMA-MATERIALS INTERFACE

C. M. Parish (parishcm@ornl.gov), D. Morrall

OBJECTIVE

The overarching objective of this work is to bridge the gap between the atomistic knowledge and models and the phenomenological materials science underlying the design, fabrication, and service of divertors and other plasma-facing components for magnetic confinement fusion. Specifically, the influence of intrinsic defects (dislocations, grain boundaries) and extrinsic defects (ion- and neutron-irradiation damage, impurities) interactions with He and He bubbles, in terms of nucleation sites, growth, trapping, and surface degradation, will be measured.

SUMMARY

This year we have explored both radiation damage and plasma-implantation effects. Radiation effects studies included continued analysis of neutron-irradiated tungsten, and plasma effects included analysis of the flux and fluence effects on the near-surface region of tungsten, and exploration of helium effects in the near-surface microstructure.

PROGRESS AND STATUS

Neutron-irradiated tungsten specimens from the HFIR 19J gadolinium-shielded capsule were examined. Electron backscatter diffraction (EBSD) was used to examine the grain sizes of the polycrystalline specimens, with typical results shown in ***Figure 39***. Thanks to the new Oxford Symmetry EBSD + Tescan MIRA3 microscope at ORNL, unprecedented numbers of grains could be measured, giving excellent statistics for the evaluation of changes (or lack of changes) in the grain sizes. Indeed, having tens of thousands of grains for grain-size calculations now opens a new question of finding the correct statistical descriptions to determine when two distributions are the same or different, which is an open question.

These observations are important, because eventual plasma-facing service behavior will depend significantly on the grain sizes, textures, and morphologies, and measurements as a function of irradiation parameters are necessary to understand the eventual plasma-facing behavior.

In addition to grain sizes, the precipitation and transmutant microstructures were examined. The CT06 (thick plate, ~0.5 dpa 800°C) sample is shown in ***Figure 40***. Here, a high density of voids is present, and X-ray mapping shows Re-enriched spherical volumes, consistent with solute clustering prior to precipitation of a second phase.

Data analysis of the EDS spectrum image, ***Figure 41***, clearly shows the Re precipitates and Re segregation in the grain boundary.

Several experimental campaigns are underway of plasma-materials interactions in collaboration with UC-San Diego. One campaign involves loading iso-fluence helium into the near-surface region of polycrystalline tungsten specimens at different temperatures in order to determine what effect a helium

bubble "blockade" might have on D-T retention, and another involves iso-thermal loading of (001) single crystals to different fluences of helium.
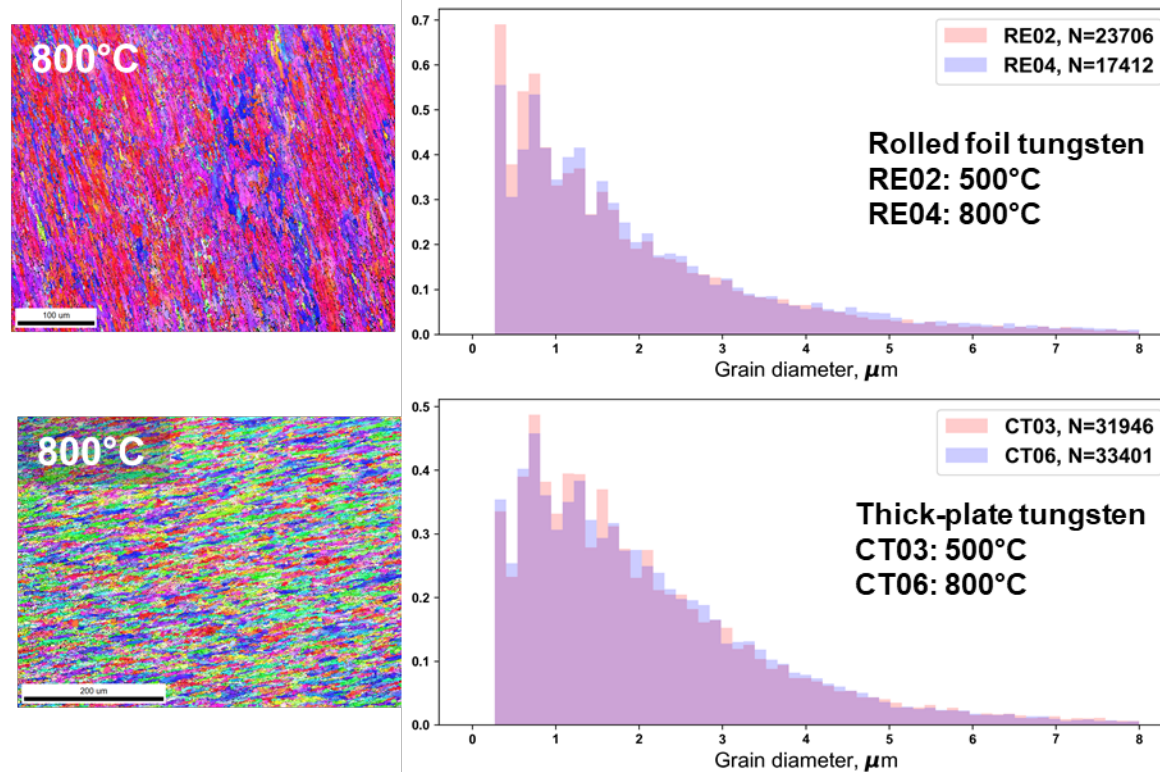
Figure 39. EBSD images (left) and measured grain sizes (right) for rolled foil and thick plate tungsten, irradiated to ~0.5 dpa at 500 or 800°C.
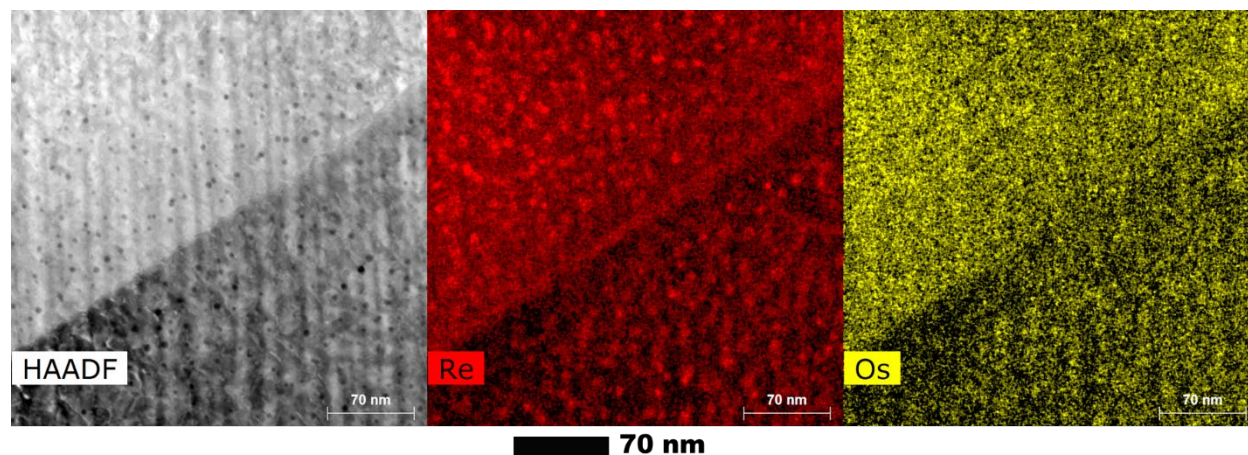
Figure 40. STEM image (left) and X-ray maps (center, right) of the 800°C, ~0.5 dpa CT06, thick-plate tungsten from the Gd-shielded HFIR 19J irradiation capsule. A high density of voids (imaged black in HAADF mode) and Re-clusters (Re map) are visible.
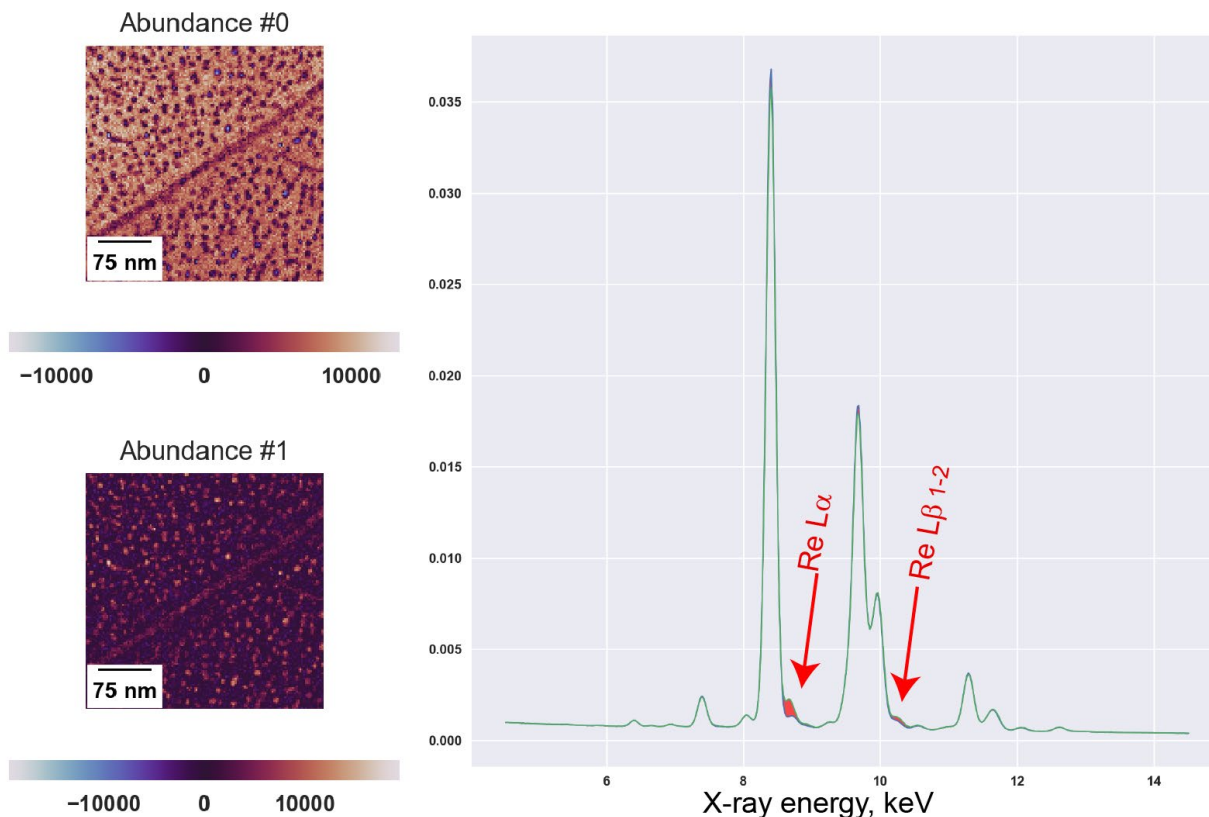
Figure 41. Abundance maps and endmember spectra from the data in Figure 40, using a modification of independent component analysis. The red regions are the differences between endmembers #0 and #1 and are associated with Re L X-ray lines.

Both campaigns with UC-San Diego are at low temperature (≤600°C) and low helium landing energy (~50 eV), so all the plasma-materials interactions are in the ~15 nm near-surface region of the specimens. However, FIB-based methods cause ~20-30 nm of damage in tungsten, so we have developed surface-specific FIB protocols to ensure the FIB preparation does not introduce excessive artifacts into the helium-implanted region. ***Figure 42*** illustrates the FIB-deposited Pt cap, but with an electron-beam-deposited carbon cap beneath the Pt. This electron beam deposition provides a non-damaging sacrificial layer to prevent the gallium beam from destroying the features of interest during the Pt deposition.

This improved protocol is compared to the "standard" (incorrect) protocol in ***Figure 43***, where significant Ga deposition and Ga/W intermixing is detected in the top ~15 nm of the specimen with the incorrect procedure. With the improved protocol, the Ga and W layers are clearly separated, and the He-induced damage is visible in the W layer's top few nanometers.
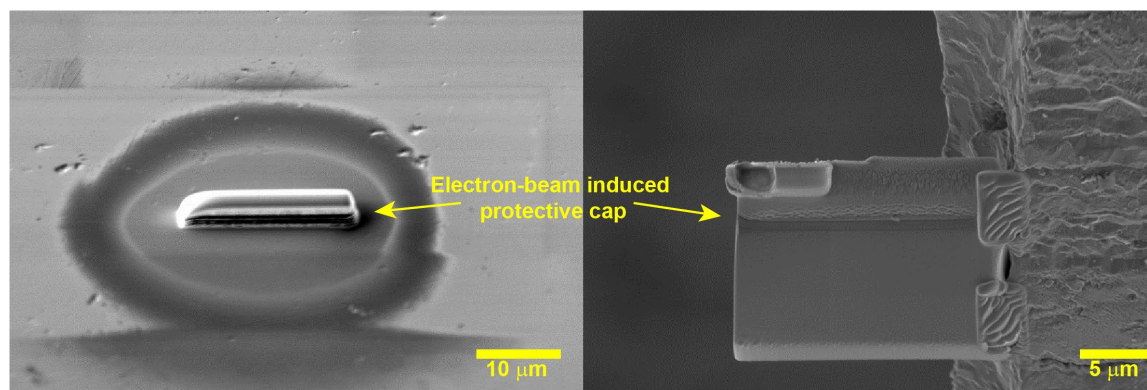
Figure 42. SEM images of the tungsten specimen (left) with deposited sacrificial layers, and the FIB liftout with the electron-beam induced protective cap visible (right).
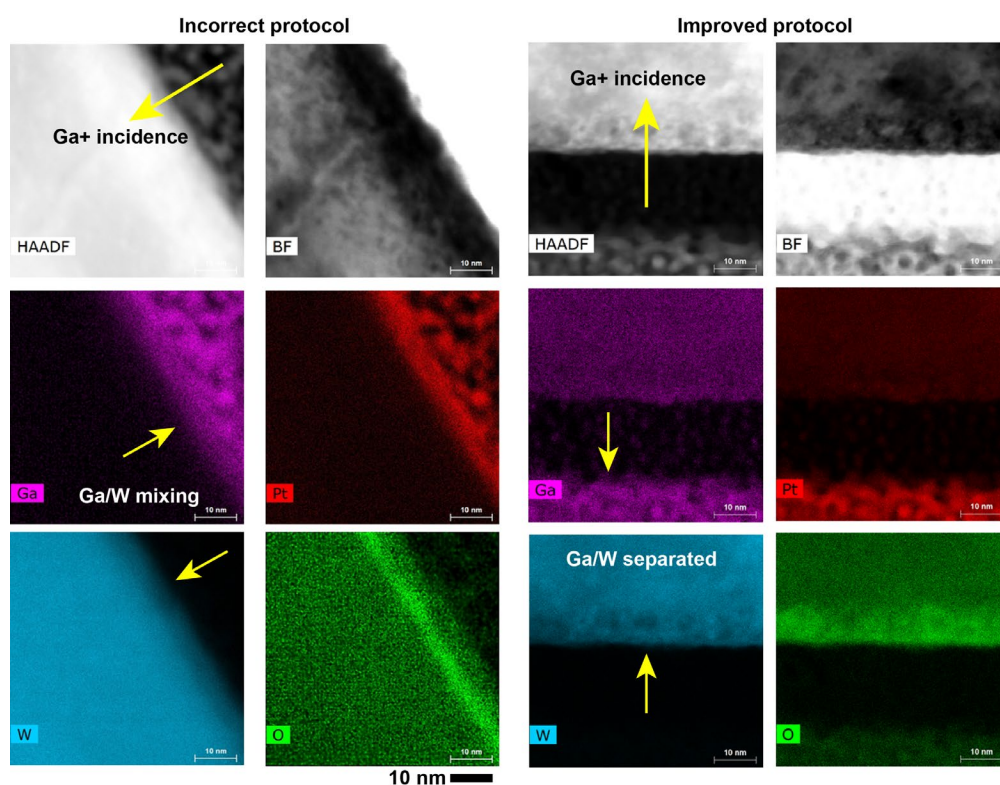
Figure 43. X-ray maps and STEM images of low-energy He-implanted tungsten prepared incorrectly (left) and correctly (right). The Ga and W layers are clearly differentiated for the correct procedure and intermixed for the incorrectly prepared specimen.

FUTURE PLANS

Our collaborations with UC-San Diego and University of Illinois will continue. We will be performing advanced characterization of UIUC specimens and will possibly begin collaborating with Stony Brook University. The newly perfected FIB procedure is in use to prepare samples from the PMI campaigns. More FIB samples will also be prepared from the HFIR 19J irradiated specimens for advanced STEM.

5.2   HYDROGEN ISOTOPE TRANSPORT PROPERTIES IN ADVANCED RAFM STEELS FOR FUSION REACTOR STRUCTURAL APPLICATION

Z. Chen, B.D. Wirth (UT Knoxville), Y. Katoh, X. Hu (hux1@ornl.gov, ORNL)

OBJECTIVE

The objective of this project is to determine the permeability, diffusivity and retention of deuterium in representative reduced activation ferritic-martensitic (RAFM) steels by using gas-driven permeation and thermal desorption spectroscopy techniques.

SUMMARY

The fundamentals of hydrogen-materials interactions are critically important for the design of a robust fusion breeding blanket enabling the self-sufficient tritium cycle. In this study, we utilized the gas-driven permeation testing techniques to determine the basic hydrogen transport properties in representative RAFM steels. This will expand the current database of hydrogen behavior in fusion materials. Thermal desorption spectroscopy (TDS) was used to measure the deuterium retention. The experimental results are comparable to literature data. In addition, the correlation between sink strength and the deuterium permeability and diffusivity was briefly discussed. More work is needed to elucidate the correlation between the microstructures and the hydrogen isotope transport properties in fusion structural materials.

PROGRESS AND STATUS

Introduction

The RAFM steels [1, 2], castable nanostructured alloys (CNAs) [3], and oxide dispersion strengthened (ODS) [4] ferritic steels are three candidate materials for future fusion reactors. Nevertheless, the hydrogen isotope behavior in those materials is not well understood [5], especially in the service environment, which is critically important to realize fusion fuel self-sufficiency and address concerns of tritium safety.

Table 6. The chemical composition of iron base materials studied

Category	Sample	Fe	Cr	W	Ta	Mn	V	C	O	Al	Si	N	Ti	Y	Co	S	P	Cu	Nb	Ni	Mo
RAFM	Eurofer97	Bal.	8.82	1.09	0.13	0.47	0.2	0.11	0.001	0.009	0.04	0.022	0.005	n/a	n/a	n/a	n/a	n/a	n/a	n/a	n/a
	G91	Bal.	8.6	n/a	n/a	0.37	0.2	0.08	n/a	n/a	0.1	0.055	n/a	n/a	n/a	n/a	n/a	n/a	0.07	0.09	0.9
CNA	FTa1	Bal.	9.01	1.1	0.1	0.46	0.32	0.1	0.008	n/a	0.23	0.05	n/a	n/a	n/a	n/a	n/a	n/a	n/a	n/a	n/a
	TT3mt	Bal.	8.5	1.3	0.1	0.9	0.1	0.08	n/a	n/a	0.1	n/a	0.1	n/a	n/a	n/a	n/a	n/a	n/a	n/a	n/a
ODS	M4	Bal.	9.7	0.97	n/a	0.01	0.18	0.031	n/a	0.01	0.02	0.0184	0.015	0.023	0.02	0.031	n/a	n/a	n/a	n/a	n/a
	9YWTV	Bal.	8.91	1.98	n/a	0.01	0.18	0.06	0.12	0.01	0.02	0.0174	0.37	0.07	0.02	0.004	0.003	0.01	0.02	0.01	n/a
	14YWT	Bal.	Bal.	14.3	2.32	n/a	0.008	n/a	0.024	0.177	0.016	0.043	0.099	0.27	n/a	n/a	n/a	n/a	n/a	n/a	n/a

In this project, we measured the deuterium transport properties of 2 RAFM steels (Eurofer 97 and G91), 3 ODS steels (M4 Fe-10Cr, 9YWT-PM2, 14YWTV-SM13) and 2 CNA alloys (FTa1 and TT3mt) in the as-fabricated state by employing the gas-driven permeation testing technique. Eurofer 97, FTa1 and 14YWT were selected for TDS tests. The compositions of these alloys are given in *Table 6*.

Experimental Work

The permeability and diffusivity tests used disk-shaped specimens machined with a diameter of 12.6 mm and ~1 mm in thickness. Then specimens were polished to a surface finish of 1 μm on each side. Permeation testing was performed using the ORNL gas-driven permeation testing station, which is shown in **Figure 44**. Ultra-high vacuum (~1×10⁻⁷ torr) was reached in both upstream and downstream sections prior to testing. The upstream gas pressure is measured by a MKS hot cathode vacuum transducer, while the downstream gas permeation flux is obtained using the quadrupole mass spectrometer (QMS). The TDS system (**Figure 44**) shared the same downstream section of the permeation testing station. In this work, we used the samples after diffusivity tests for the TDS measurements. The temperature ramp rate used was 0.5°C /s.
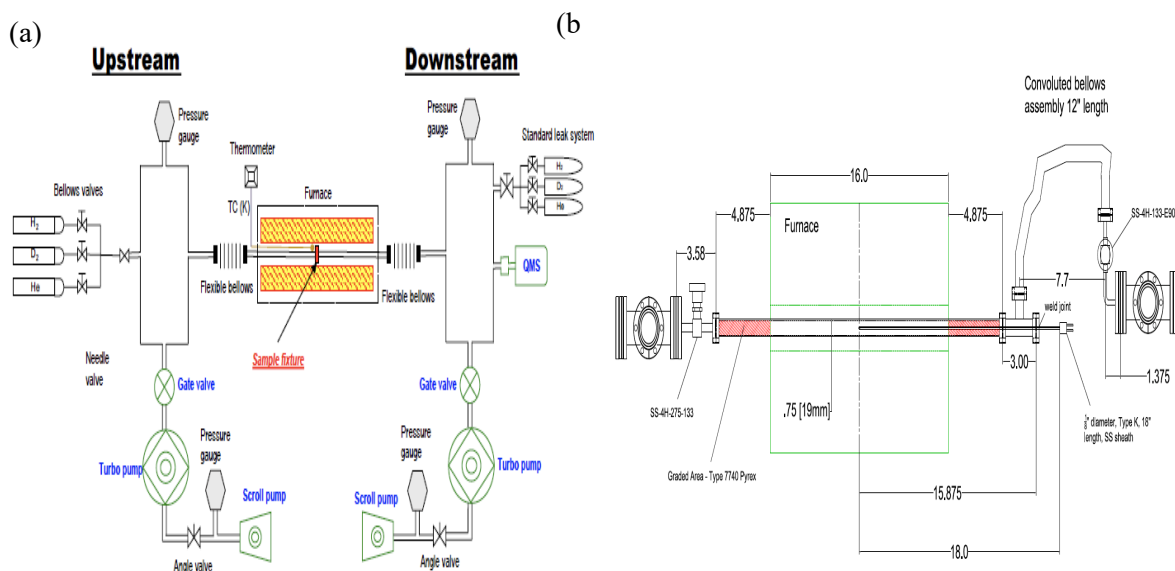
Figure 44. Schematic view of the (a) gas-driven permeation system (left) and (b) the thermal desorption spectroscopy system (right).

Results and Discussion

Deuterium Transport Properties

The deuterium permeation flux through the studied materials was recorded as a function of applied D gas pressure (140 to ~ 500 torr) in the temperature range from 350°C to 600°C. The applied D pressure for the diffusivity tests was fixed at 1 atm.

Theoretically, the steady state permeation flux is related to the square root of driving gas pressure through [6]:

$$J = \Phi \frac{p^{1/2}}{\delta} \tag{1}$$

Where Φ is the deuterium gas permeability in units of mol $D_2\ m^{-1}s^{-1}MPa^{-1/2}$, J is the permeation flux in mol $D_2\ m^{-2}s^{-1}$, p is the applied gas pressure in MPa and δ in the sample thickness in m.

At the steady permeation state, the downstream pressure linearly increases. Thus dffusivity can be obtained by the time lag method [8]:

$$t_L = \frac{\delta^2}{6D} \tag{2}$$

Both permeability and diffusivity can be described with Arrhenius expressions:

$$\Phi = \Phi_0 \cdot exp\left(-\frac{E_\Phi}{RT}\right) \tag{3}$$

$$D = D_0 \cdot exp\left(-\frac{E_D}{RT}\right) \tag{4}$$

The permeability of deuterium in the studied materials is summarized in ***Figure 45***. The results indicate that the deuterium permeabilities of these tested samples are within a narrow range of one order of magnitude. However, it is observed that the ODS steels have relatively lower permeability, especially the 14YWT-SM13, which has the highest sink strength due to the large number density of nanoparticles. The deuterium permeability of Eurofer97 is highest among all tested materials.
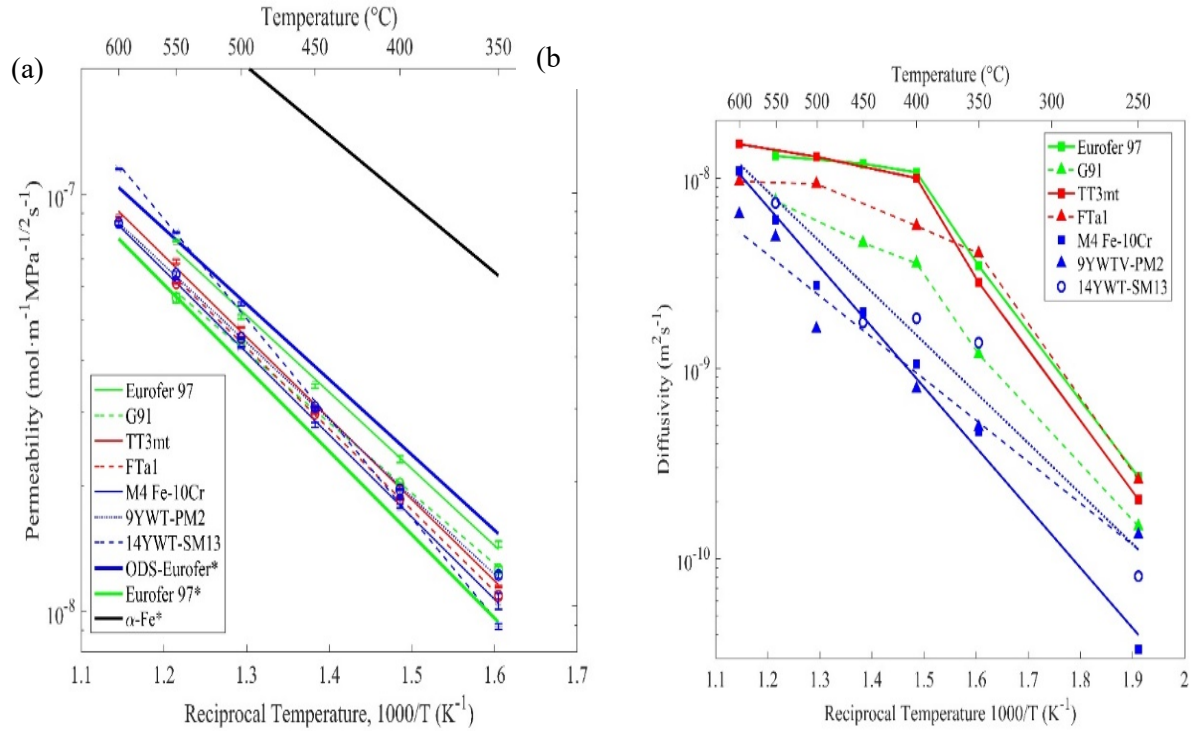
Figure 45. (a) Deuterium permeability (left) and (b) deuterium diffusivity(right) of advanced steels. Data for alpha iron taken from literature are also shown for comparison [7].

Table 7. Deuterium permeability coefficients and activation energies for advanced RAFM steels

Category	Sample steel	Temperature °C	Φ_0 $mol \cdot m^{-1} \cdot s^{-1} \cdot MPa^{-1/2}$	E_Φ $kJ \cdot mol^{-1}$	D_0 $m^2 \cdot s^{-1}$	E_D $kJ \cdot mol^{-1}$
RAFM	Eurofer 97	350-550	1.26×10^{-5}	35.22	8.89×10^{-7}	14.71
	G91	350-550	4.22×10^{-6}	29.85	2.02×10^{-6}	15.82
CNA	TT3mt	350-600	1.55×10^{-5}	37.30	3.15×10^{-8}	2.54
	FTa1	350-600	1.46×10^{-5}	37.26	6.13×10^{-8}	4.30
ODS	M4 Fe-10Cr	350-600	1.53×10^{-5}	37.75	1.04×10^{-7}	7.00
	9YWTV-PM2	350-600	1.14×10^{-5}	35.51	2.23×10^{-7}	13.46
	14YWT-SM13	350-600	1.73×10^{-5}	39.67	8.42×10^{-6}	20.86
Ref.	ODS-Eurofer[7]	/	4.22×10^{-5}	34.6	1.33×10^{-6}	30.4
steels	Eurofer 97[7]	/	1.53×10^{-5}	38.3	1.50×10^{-7}	14.5

The diffusivity of deuterium in the studied materials is summarized in *Figure 45*. Diffusion coefficients and activation energies of these seven materials were obtained by fitting the experimental data, given in *Table 7*. The diffusion activation energy of CNA steels is clearly smaller than that of conventional RAFM steels and ODS steels. More work is needed to understand the correlation between the microstructure and the measured diffusivity data.

In consideration of the trapping phenomena caused by the microstructures, which has a significant influence on the time lag determination, fresh samples were used for diffusivity tests at each measurement temperature. The upstream deuterium pressure is set to 1 atm. The results of diffusivity of the seven RAFM steels, together with literature data for ODS-Eurofer and Eurofer97, are plotted in the *Figure 45*b. Generally, the deuterium diffusivity in steels with higher sink strength is lower than that with lower sink strength. These measured diffusivities in the current study are comparable to the literature data.

Deuterium Retention

The TDS results, *Figure 46*, show that the peak desorption rate for deuterium is comparable for Eurofer97 and FTa1, while that for 14YWT is 1 to ~2 orders of magnitude higher. This clearly shows that the ODS steels have stronger trapping for hydrogen species than does CNAs and RAFM steels [9].
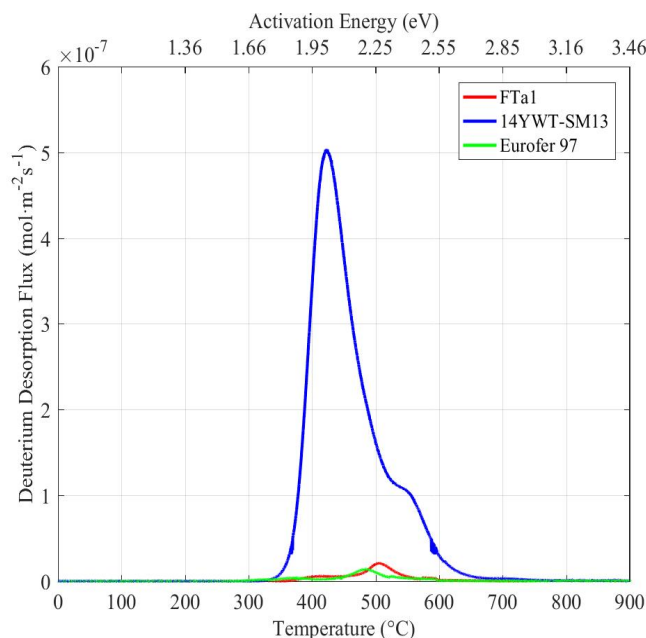
Figure 46. Deuterium desorption and retention results.

FUTURE PLANS

The deuterium diffusivity in ODS steels is quite different than that in RAFM and CNAs. More tests are needed to investigate and understand the trapping effects at lower temperatures. Trapping energy will be obtained by fitting the effective diffusivity data and will be compared to the binding energy between D and defects, to determine dominating effects that influence the diffusion behaviors.

REFERENCES

[1.] Tanigawa, H., et al., *Status and key issues of reduced activation ferritic/martensitic steels as the structural material for a DEMO blanket.* Journal of Nuclear Materials, 2011. **417**(1-3): p. 9-15.

[2.] Zinkle, S.J., et al., *Development of next generation tempered and ODS reduced activation ferritic/martensitic steels for fusion energy applications.* Nuclear Fusion, 2017. **57**(9): p. 092005.

[3.] Tan, L., Y. Katoh, and L.L. Snead, *Development of castable nanostructured alloys as a new generation RAFM steels.* Journal of Nuclear Materials, 2018. **509**: p. 267-275.

[4.] Hoelzer, D.T., *History and outlook of ODS/NFA ferritic alloys for nuclear application.* Transactions of the American Nuclear Society, 2018. **118**: p. 1587-1590.

[5.] Zinkle, S.J., et al., *Multimodal options for materials research to advance the basis for fusion energy in the ITER era.* Nuclear Fusion, 2013. **53**(10).

[6.] Oriani, R.A., *The diffusion and trapping of hydrogen in steel.* Acta Metallurgica, 1970. **18**(1): p. 147-157.

[7.] Esteban, G.A., et al., *Hydrogen transport and trapping in ODS-EUROFER.* Fusion Engineering and Design, 2007. **82**(15-24): p. 2634-2640.

[8.] Andrew, P.L. and A.A. Haasz, *Models for hydrogen permeation in metals.* Journal of Applied Physics, 1992. **72**(7): p. 2749-2757.

[9.] Hu, X., and et al., *Deuterium retention in advanced steels for fusion reactor structural application.* Journal of Nuclear Materials, 2019. **516**: p. 144-151.

5.3   HIGH HEAT FLUX TESTING OF NEUTRON IRRADIATED TUNGSTEN

L.M. Garrison (garrisonlm@ornl.gov), A. Sabau, B. Gregory, J.W. Geringer, Y. Katoh, S. Copp (Oak Ridge National Laboratory), Y. Hamaji (National Institute of Fusion Science), A. Hasegawa (Tohoku University)

OBJECTIVE

The aim of this work is to understand how neutron irradiation and high heat flux cyclic loading change the morphology and properties of tungsten.

PROGRESS AND STATUS

Samples of K-doped W-3Re and thick plate unalloyed W, each with grains elongated perpendicular to the surface, were exposed to high heat flux (HHF) cycles in the ORNL Plasma Arc Lamp (PAL). Both unirradiated and neutron irradiated samples from the HFIR RB*-19J of the two materials were exposed. The surfaces were imaged with scanning electron microscopy (SEM) before and after HHF exposure and will be used for further analysis.

The SEM images for a single sample condition are shown here. Thick plate, unalloyed W was neutron irradiated in the HFIR at 550°C to a fast fluence of 1.24×10^{25} n/m^2 E>0.1 MeV (~0.24 dpa). Unirradiated and irradiated specimens of the material were HHF tested in the Plasma Arc Lamp (PAL) facility. The PAL uses a high-power photon source to provide a broad and even heat distribution on the sample surface. The samples were exposed to approximately 800 cycles at 4.73 MW/m^2 absorbed heat flux (incident heat fluxes of 10.95 MW/m^2). The SEM examination after PAL exposure showed only slight changes on the surfaces of the samples. The samples showed some annealing in the near surface polished region, but they were all below the damage threshold for cracking or other destructive features.

Sample 5002 is thick plate tungsten produced by ALMT. It was irradiated at 550C to 0.24 dpa and then exposed to HHF conditions as specified above. Before HHF exposure (**Figure 47**) the sample surface is typical of the finish after polishing to 800 grit, showing some polishing scratches, small depressions, and small raised areas on the surface. The engraving of the character "5" was used as an easily identifiable location so the same area could be located after HHF exposure. After HHF exposure (**Figure 48**) all the features that were observed before HHF are still present, with no additional changes as a result of the ~800 HHF cycles. This indicates that more HHF cycles or higher power would be required to see annealing or damage of the neutron irradiated material.
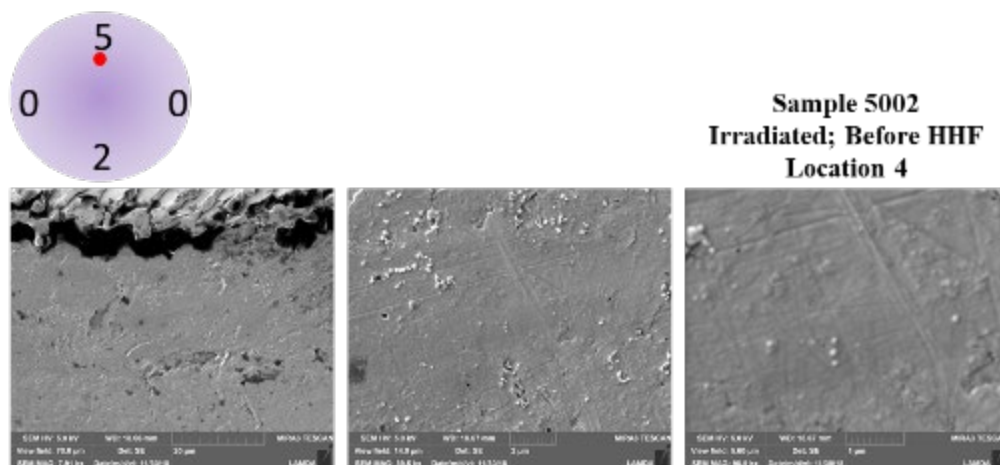
Figure 47. A representative location on the surface of sample 5002 after neutron irradiation, but before HHF exposure. The ridges at the top of the left image are pre-existing damage from the laser engraving of the character "5".
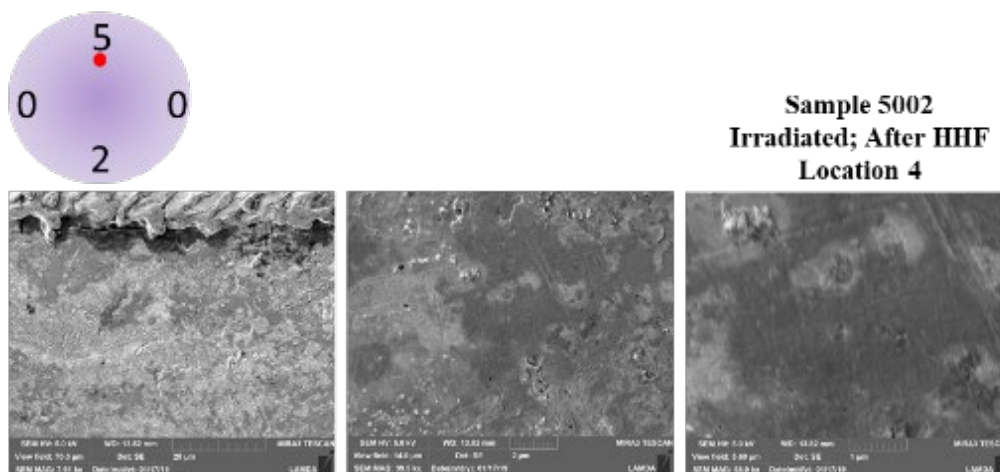
Figure 48. The same location as in Figure 1 after HHF exposure. The contrast in the image is slightly different, but all the same features can be found after HHF exposure, with no additional evidence of the ~800 cycles of HHF.

6.   LIQUID METAL COMPATIBILITY

6.1   STRUCTURAL ALLOY COMPATIBILITY WITH LIQUID Pb-Li IN FLOWING SYSTEMS

B. A. Pint (pintba@ornl.gov), J. Jun

OBJECTIVE

This task investigates the possibility of increasing the allowable Pb-Li temperature in the dual coolant lead-lithium (DCLL) blanket concept to improve the overall system efficiency. The FeCrAl alloys are potential candidates, and monometallic thermal convection loops of a commercial FeCrAl alloy have been operated to determine a maximum operating temperature where the alloy is compatible with the flowing eutectic Pb-Li.

SUMMARY

A fourth monometallic thermal convection loop (TCL) fabricated from dispersion strengthened FeCrAl (Kanthal alloy APMT, Fe-21Cr-5Al-3Mo) tubing was operated for 1000 hr with a peak temperature of 700°C. The experiment was completed in October 2019 and the specimens have not been characterized at this time. The PbLi flow velocity was determined by hot spot tests.

PROGRESS AND STATUS

To assess Pb-Li compatibility and the maximum operating temperature for an alumina-forming alloy or coating, a series of monometallic thermal convection loops (TCLs) have been fabricated from Kanthal alloy APMT (Fe-21Cr-5Al-3Mo) with peak operating temperatures of 550, 600, 650 and 700°C from 2014 to 2019. Each loop operated for 1000 hr and the fourth loop was completed in October 2019 and the specimens in the hot and cold legs of the TCL have not yet been characterized. The key finding from the first three TCL experiments is that by pre-oxidizing APMT to form an external α-Al$_2$O$_3$ layer, the mass loss was minimized but the alumina was transformed to α-LiAlO$_2$, which spalled in some cases. Such behavior needs to be better understood in order to model long-term behavior. Also, above 500°C, there was minimal effect on the post-exposure room temperature tensile properties.

For the fourth TCL experiment with a peak temperature of 700°C, the PbLi flow velocity was checked using a hot spot test where a localized area was externally heated and then the movement of the hot liquid was tracked along the thermocouples (TCs) in the flow path. ***Figure 49*** shows the temperature profiles from 4 TCs during one hot spot test. The flow velocity was calculated using the time between the peaks measured as the hot spot traveled and the distance between TCs. The calculated velocity was 1.4 cm/s, which is slightly faster than the PbLi velocity of 0.6-0.9 cm/s measured in the previous experiments. Once the 40 APMT specimens in the hot and cold legs are removed and cleaned, specimen mass change, room temperature tensile testing and characterization of the surface oxides (including x-ray diffraction) will be completed. Several specimens included in the loop were not pre-oxidized; these will be used to assess the effects of pre-oxidation.
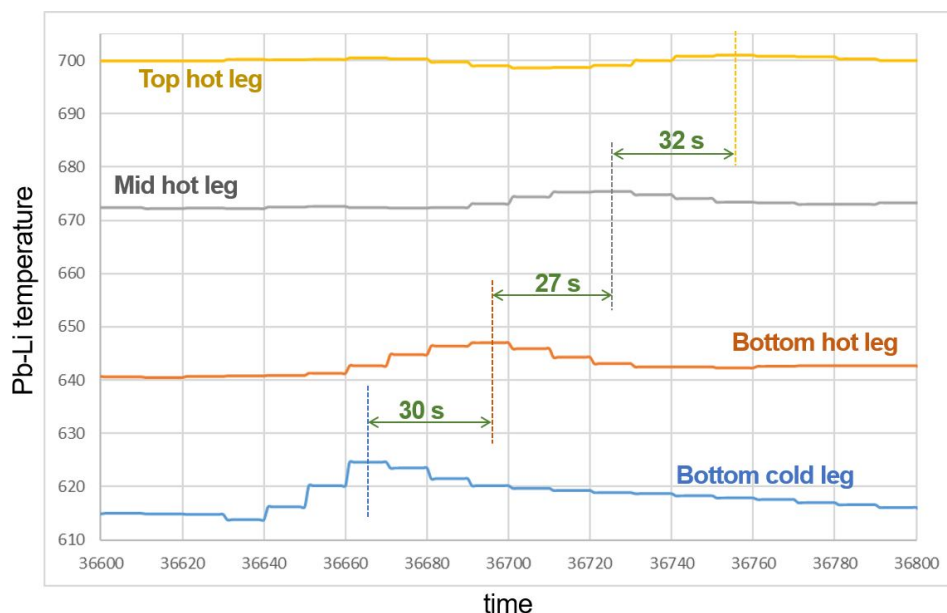
Figure 49. Temperature as a function of time during the hot spot test in the most recent TCL experiment. Temperature peaks appeared at each thermocouple (TC) as locally heated Pb-Li traveled through the flow direction. The flow time between peaks and distance between TCs were used to calculate the flow velocity of the liquid eutectic Pb-Li.

FUTURE PLANS

In FY 2020, this project will complete characterization of the specimens from the fourth TCL experiment and then switch emphasis to liquid Sn compatibility to support the FRONTIER collaboration. A new project focused on blanket conditions will begin to expose more fusion-relevant materials (SiC and low-Cr ODS FeCrAl) under the same conditions of flowing PbLi with a peak temperature of 700°C in the initial loop experiment.

6.2   STRUCTURAL ALLOY COMPATIBILITY WITH STATIC LIQUID METALS Li, Sn AND Sn-Li

B. A. Pint (pintba@ornl.gov), J. Jun

OBJECTIVE

The objective of this task is to evaluate the compatibility of structural steels with thermally grown surface oxides in liquid Li, Sn and Sn-Li. For plasma wall applications, Sn and Sn-Li offer much lower vapor pressures than Li but Li is known to be less corrosive to structural steels at higher temperatures.

SUMMARY

After promising results for pre-oxidation in the first round of isothermal testing in liquid Sn at 400°C, a second round of isothermal Sn exposures at 400°C included pre-oxidized Kanthal APMT (Fe-20Cr-5Al-3Mo) and Fe-20Cr, which form Al_2O_3 and Cr_2O_3 surface layers, respectively. The results were particularly impressive for APMT and an additional exposure was conducted at 500°C, which also showed a low mass change after a 1000 hr exposure.

PROGRESS AND STATUS

The goal of this task is to investigate the concept of surface oxide barriers to protect structural steels in liquid Li, Sn and Sn-Li that are candidate plasma facing liquid metal components in fusion reactors. Previously, isothermal capsule experiments were conducted in Li at 600°C and Sn and Sn-Li at 400°C. As expected, the exposure in Li dissolved the surface oxide, while the pre-oxidation of APMT was very effective, especially in Sn at 400°C. In contrast, a conventional ferritic-martensitic steel, F82H (Fe-8Cr-2W), was heavily attacked in Sn, with much higher mass loss than bare (no pre-oxidation) APMT. A second series of experiments was conducted to determine if the improvement between APMT and F82H could be attributed to the Al addition or the higher Cr content compared to F82H and to determine if a Cr-rich oxide was also protective under the same conditions.

Figure 50 shows the mass change data for the second set of experiments. Without pre-oxidation, the mass losses for Fe-20Cr and Fe-5Al model alloy coupons were much higher than APMT after 1,000 hr in liquid Sn at 400°C. Pre-oxidation of Fe-20Cr for 2 hr at 800°C resulted in a significant improvement as did pre-oxidation of APMT for 2 hr at 1000°C. The latter oxidation treatment was so protective that surface x-ray diffraction only detected α-Al_2O_3 and the ferritic substrate with no Sn compounds detected. Thus, a second exposure for 1000 hr at 500°C was conducted and resulted in only a small mass gain, as shown in ***Figure 50***.

FUTURE PLANS

To confirm the Sn compatibility, a flowing thermal convection loop experiment is being planned as part of the US-Japan FRONTIER collaboration. A review paper on liquid metal compatibility relevant to fusion blankets and plasma facing components is being prepared for publication.
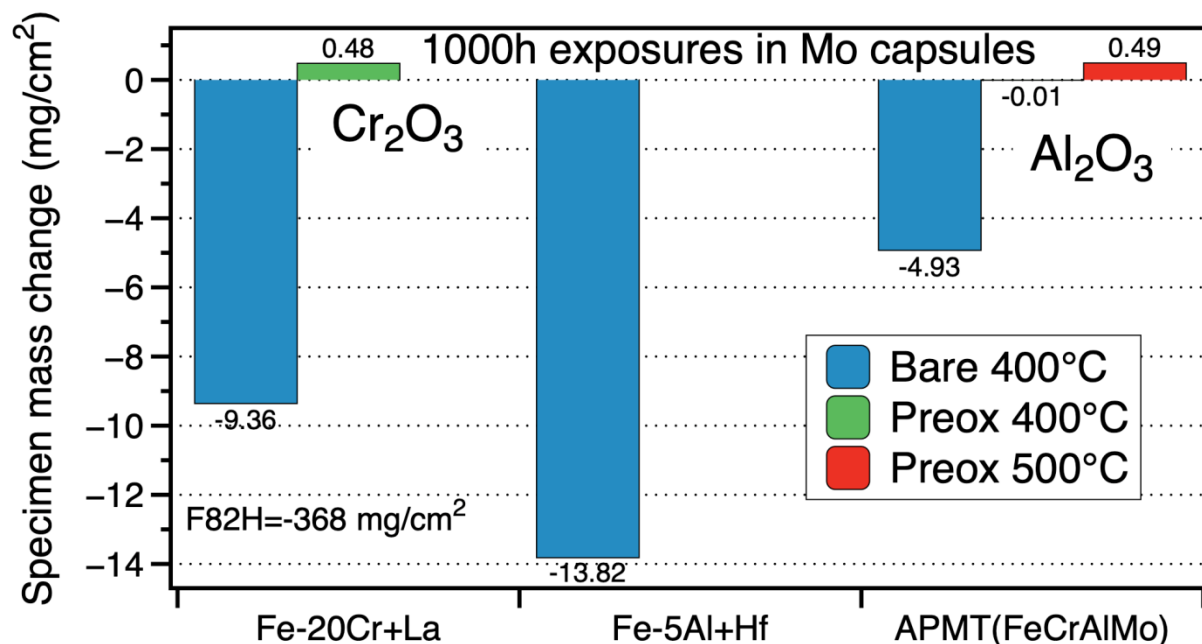
Figure 50. Specimen mass change data for specimens exposed to liquid Sn for 1000 h in isothermal capsule experiments at 400° and 500°C. The APMT specimens were pre-oxidized in air for 2 hr at 1000°C and the Fe-20Cr specimens were pre-oxidized for 2 hr at 800°C. All the mass losses were much less than that observed for FeCrW alloy F82H.

7.   EXPLORATORY, UNIQUE AND INNOVATIVE MATERIALS

7.1   PROPERTIES AND CHARACTERIZATION OF NOVEL COPPER ALLOYS FOR FUSION ENERGY APPLICATIONS

Ying Yang (yangying@ornl.gov), Ling Wang, Steven J. Zinkle (University of Tennessee)

OBJECTIVE

This study aims at developing high strength, high conductivity Cu alloys with improved thermal creep strength for long pulse fusion high heat flux structures, through an accelerated approach of computational thermodynamics guided alloy design.

SUMMARY

Work performed during the reporting period was to investigate the creep properties of a high-purity CuCrNbZr alloy in comparison with properties of the commercial CCZ alloy and identify the role of Laves Cr_2Nb precipitate on the creep property.

PROGRESS AND STATUS

The commercial CCZ alloy (Cu-0.78Cr-0.06Zr, wt.%) produced by Kabelmetal was used as a reference alloy, and was prepared by solution annealing in flowing argon at 980°C for 1 h, water quenched, followed by thermal aging at 475°C for 2 h in flowing helium [1]. The newly developed CCNZ_HP alloy was designed with a nominal composition of Cu-2Cr-1.35Nb-0.15Zr, wt.%. The chemical analysis result on the ingot showed Cu-1.77Cr-1.23Nb-0.18Zr, <0.002Sn, 0.0039Fe, <0.006O and <0.001N, wt.%. Oxygen and nitrogen were analyzed using inert gas fusion (ASTM E 1019-11) and all other elements were analyzed using direct current plasma emission spectroscopy (ASTM E 1097-12). The ingot was melted in an argon protected arc-melting furnace followed by drop-casting into the shape of $1.25\times1.25\times0.75$ cm^3 bar, with an approximate mass of 100 g. The as-cast bar was then multiple-pass cold rolled at room temperature for a total 70% reduction in thickness. The as-rolled material was then solution annealed at 970°C for 20 min, followed by water quench, and then aged at 475°C for 3 h followed by air cooling.

The creep tests were first performed in air at 500°C and 90 MPa. The creep life of CCNZ_HP alloy was 4.0×10^5 s (~110 h), which was about 1.5 times longer than that of the reference CCZ alloy, 2.6×10^5 s (~72 h). Significant oxidation occurred in both alloys during these creep test conditions. To minimize the oxidation impact on a subsequent systematic study of creep strain rates at different stresses, follow-on creep tests on the CCZ and CCNZ_HP alloys were conducted at 500°C in flowing Ar gas with applied stress levels of 90, 100, 110, 125 and 140 MPa. The corresponding plots of creep strain versus time of both alloys are shown in *Figure 51***a** and **Figure 51b**. The creep life of the CCNZ_HP alloy exceeded that of the CCZ alloy for all the applied stresses. The rupture strain for the CCNZ_HP alloy was similarly significantly higher (by about a factor of two) compared to the CCZ alloy for all test conditions. Linear curves were fitted to the applied stress vs. time to rupture data in *Figure 51***c**. The fitting for the CCZ alloy only included data from 90, 110 and 125 MPa applied stresses since the creep under 100 and 140 MPa (denoted by data points with an overlaid X in *Figure 51***c**; data points not plotted in *Figure 51***d** and **Figure 51e** resulted in premature failure as shown in *Figure 51***a.** The fitted curves for applied stress vs. rupture time of the CCZ and CCNZ_HP alloys are nearly parallel to each other, indicating qualitative similarity of the two alloys, whereas from a quantitative perspective the CCNZ_HP alloy had uniformly higher creep strength and longer creep life than the CCZ alloy for all test conditions at 500°C. It is worth

noting that instead of showing a prolonged steady state creep regime, the creep rates of both alloys continued to increase during all tests. This is probably due to the elevated test temperature (~0.6 T_m) [2]. The minimum creep rate vs. applied stress and rupture time for the CCZ and CCNZ_HP alloys are shown in *Figure 51*d and **Figure 51e**, respectively. The CCZ alloys exhibit lower (i.e., superior) minimum creep strain rates than the CCNZ_HP alloys. A power-law equation can be used to obtain a simple estimation of the creep behavior of metallic alloys [3]:

$$\dot{\varepsilon} = A\sigma_a^m exp\left(\frac{-Q_c}{RT}\right), \tag{1}$$

where $\dot{\varepsilon}$ is the minimum creep rate (s^{-1}), A is a material constant (MPa^{-n}, s^{-1}), σ_a the applied stress (MPa), m the apparent stress exponent, Q_c the apparent activation energy for creep (kJ/mol), R the gas constant (8.314 kJ/mol-K) and T is the absolute temperature in K. The apparent stress exponents 8.7±0.9 and 6.6±1.3 were obtained from the slopes of the linear fitting for the CCZ and CCNZ_HP alloys, respectively. Both alloys show creep rates inversely proportional to the time to rupture in *Figure 51*e.
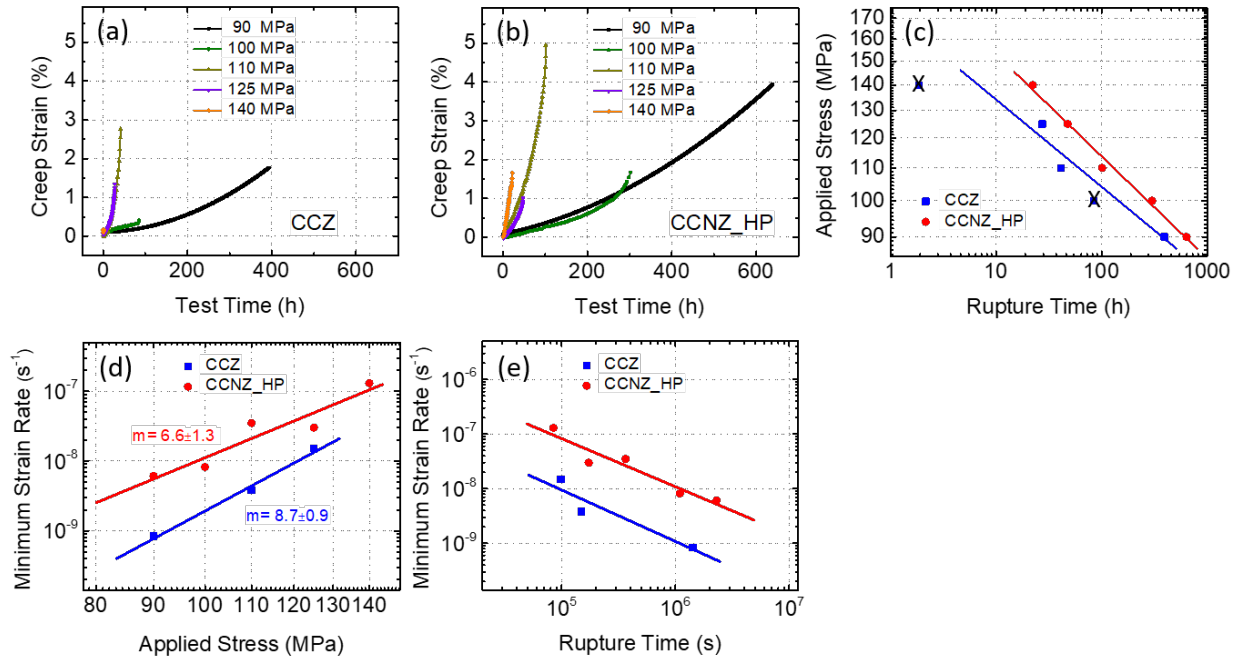
Figure 51. Creep strain vs test time at 500°C for (a) the CCZ alloy and (b) the CCNZ_HP alloy under 90-140 MPa applied stress, (c) applied stress versus rupture time for the two Cu alloys, (d) minimum creep rate versus applied stress, and (e) minimum creep rate versus rupture time for CCNZ_HP and CCZ alloys on a double logarithmic scale.

Based on the best match between the assumed stress exponent and obtained stress exponent, grain boundary sliding (n=2) is the most likely dominant creep mechanism for both the CCZ (n=1.6±0.4) and CCNZ_HP (n=1.7±0.4) alloys at 500°C for applied stress levels of 90-140 MPa. The corresponding threshold stresses were 82 and 79 MPa, respectively. *Figure 52*a shows the plots of $\dot{\varepsilon}^{\wedge(1/2)}$ versus σ_a for the CCZ and CCNZ_HP alloys (i.e., assuming the stress exponent is 2). The minimum creep strain rates as a function of the effective stress on a double logarithmic scale at 500°C for n=2 are shown in *Figure 52*b.

With the grain boundary sliding mechanism, the theoretical steady state strain rate could be calculated from the model by Ruano and Sherby [4]

$$\dot{\varepsilon}_{gbs} = 10^8 \frac{D_{gb}b}{\overline{L}^3} \left(\frac{\sigma_a - \sigma_{th}}{E}\right)^2 \qquad\qquad (3)$$

where D_{gb} is the grain boundary diffusivity (cm^2/s), $\boldsymbol{b}$ the Burgers vector (nm), $\overline{L}$ the mean linear intercept grain size (μm) and E the modulus of elasticity (GPa). The grain boundary diffusivity is given by $D_{gb} = D_{0gb}\, exp\left(\frac{-Q}{RT}\right)$ where D_{0gb} is grain boundary diffusion coefficient (cm^2/s), taken to be ~2 cm^2/s within the range reported for fcc metals by Gibbs and Harris [5], Q the grain boundary diffusion activation energy (133.9 kJ/mol) [6], R the universal gas constant (8.314 J/mol-K), T the absolute temperature in K. The value for b was taken to be 0.256 nm for dislocations in the fcc Cu matrix, and the modulus of elasticity E=100 GPa was estimated for Cu alloys at 773K [7].

The calculated theoretical grain boundary creep strain rates are between the values of 4.9×10^{-10} /s (90 MPa) and 1.4×10^{-8} /s (125 MPa) for CCZ, and 5.2×10^{-9} /s (90 MPa) to 1.6×10^{-7} /s (140 MPa) for CCNZ_HP, which are comparable to their experimental minimum strain rates in **Figure 51d**, consistent with the assumption of the prominent creep mechanisms of the two Cu alloys as grain boundary sliding. Plots of grain size-normalized minimum creep rate versus effective stress of CCZ and CCNZ_HP alloys are shown in **Figure 52c**. The linear fitted line of grain size-normalized creep rates in CCNZ_HP alloys overlapped with original fitted line of CCZ alloys (**Figure 52b**) when creep data for the CCNZ_HP were normalized by cube of mean grain size of CCNZ_HP (22 μm) over CCZ alloy (39 μm), providing support that grain boundary sliding is the main creep mechanism for these test conditions.
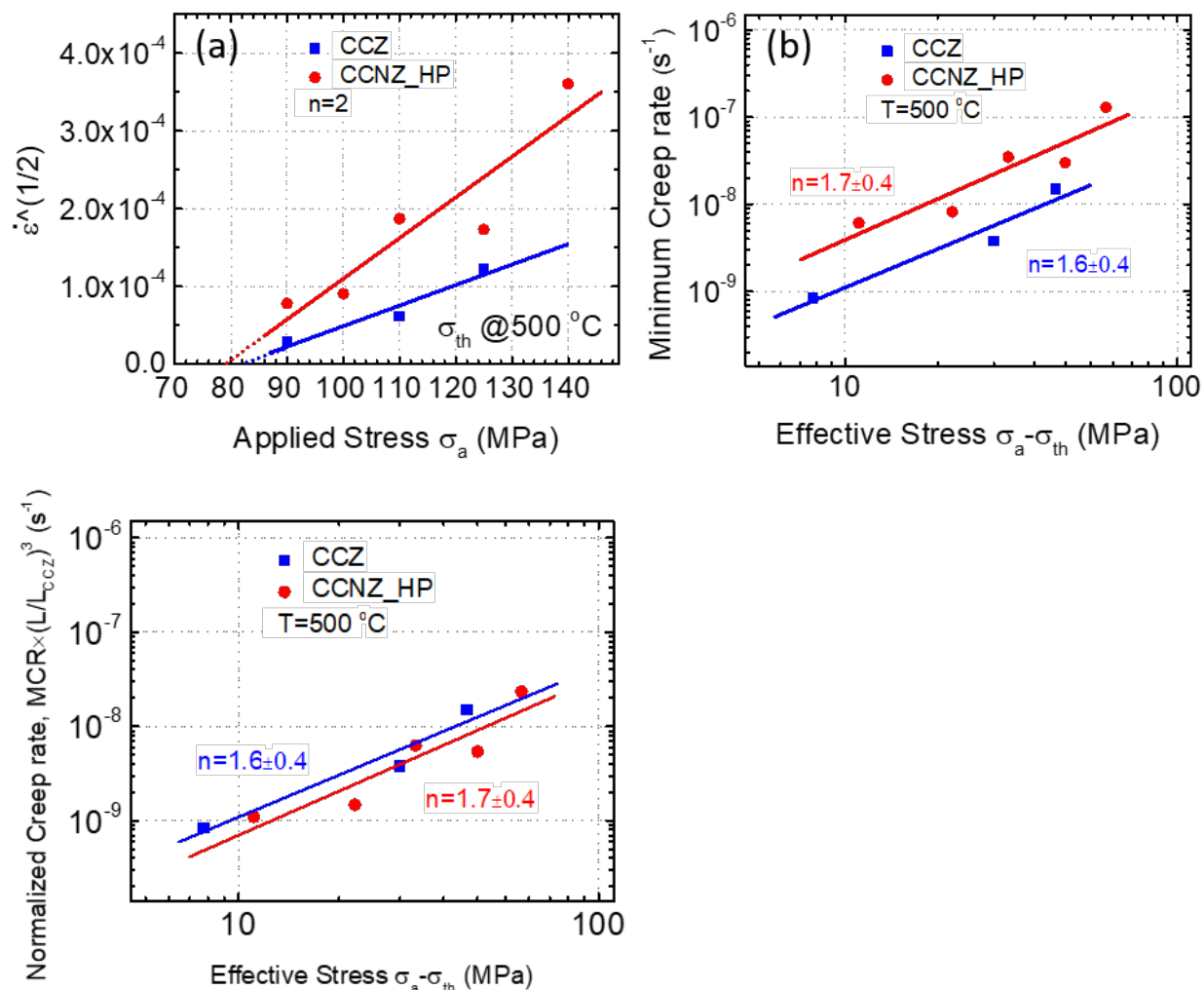
Figure 52. (a) Threshold stress calculation using linear extrapolation method for n=2, (b) minimum strain rate versus effective stress at 500ºC, and (c) normalized minimum creep strain rate as a function of effective stress of CCZ (blue) and CCNZ_HP (red) alloys.

While the creep of both the CCZ and CCNZ_HP alloys are dominated by the grain boundary sliding mechanism, the CCNZ_HP alloy shows higher creep strength and longer creep life (higher creep fracture strain) than the CCZ alloy for all tested conditions. It is intriguing to see the enhanced creep life in the CCNZ_HP alloy even though its minimum creep strain rate is also higher. The higher value of the minimum creep strain rate can be attributed to the finer grain size of the CCNZ_HP alloy. The enhanced creep life behavior and higher creep fracture strain for the CCNZ_HP alloy may be associated with the presence of Laves phase precipitates. It is well known [8] that grain boundaries are a potential source of weakness at high temperatures because they provide both nucleation sites for cavities and paths for the interlinkage of cavities to form intergranular cracks. It is apparent that the larger cracks developed at grain boundaries without Laves phases, and much smaller cracks occurred at grain boundaries covered by Laves phase. This suggests the coarse Laves phase is effective in blunting crack tips and suppressing crack propagation, thereby increasing the creep strength, overall creep fracture strain, and creep life. On the other hand, Laves phase is also very effective to inhibit grain growth during high temperature annealing (such as the solution anneal treatment at 970°C). The non-uniform distribution of Laves phase precipitates at grain boundaries that formed during solidification apparently led to non-uniform grain size

in the CCNZ_HP microstructure. The grains associated with the Laves precipitates remain small in all testing conditions, while the grains far from the Laves precipitates show much larger size. The regions clustered with small grains have a higher tendency for crack initiation, therefore causing a higher minimum creep rate. The non-uniform distribution of Laves phase left a large fraction of grain boundaries uncovered by precipitates, which made the material less effective to resist grain boundary sliding.

FUTURE WORK

Continuing research on these alloys will be directed at optimizing the distribution of Laves Cr_2Nb precipitates through alloy design and thermomechanical treatment.

REFERENCES
[1] K-M Kabelmetal, Technical data brochure on Cu alloy moulds for continuous casting (Elbrodur® CuCrZr alloy).
[2] F. Abe, T. Kern, R. Viswanathan. Creep-resistant steels. Woodhead Publishing Limited and CRC Press, LLC, 2008.
[3] C. R. Barrett, O. D. Sherby, Steady-state creep characteristics of polycrystalline copper in the temperature range 400˚ to 950˚C, Transaction of the Metallurgical Society of AIME, 230 (1964) 1322-1327.
[4] O. Ruano and O. Sherby Low stress creep of fine-grained materials at intermediate temperatures: diffusional creep or grain boundary sliding? Materials Science and Engineering 56 (1982) 167-175.
[5] W. B. Beere, G. W. Greenwood. The effect of hydrostatic pressure on the shrinkage of cavities and metals, Metal Science Journal 5 (1971) 107-113.
[6] S. E. Broyles, K. R. Anderson, J. R. Groza and J. C. Gibeling. Creep deformation of dispersion-strengthened copper, Metallurgical and Materials Transactions A 27 (1996) 1217-1227.
[7] H. M. Ledbetter, E. R. Naimon. Elastic properties of metals and alloys. II. Copper, Journal of Physical and Chemical Reference Data 3 (1974) 897-935.
[8] T. G. Langdon. The role of grain boundaries in high temperature deformation. Materials Science and Engineering A 166 (1993) 67-79.

7.2 EFFECT OF GAMMA IRRADIATION ON SECOND-GENERATION HIGH TEMPERATURE SUPERCONDUCTORS

P. D. Edmondson (edmondsonpd@ornl.gov)

OBJECTIVE

The objective of this ongoing task is to evaluate the effects of gamma irradiation on the superconducting properties of second-generation high temperature superconductors (HTS) as part of the exploration of their possible use in fusion applications.

SUMMARY

In order to explore the viability of the use of HTS materials in fusion applications, it is necessary to investigate and understand the effects of radiation on the functional properties of the HTS material. Considering this, a campaign effort is ongoing to investigate these effects on two second-generation high temperature superconductors based on the yttrium-barium-copper-oxide (YBCO) structure, the results of which will ultimately determine the potential applicability of YBCO-based HTS for fusion. The results will also aid the design of local shielding. A neutron-irradiation campaign previously investigated the effects of particle irradiation; the focus of our current investigations is transitioning to the effects of gamma irradiation.

PROGRESS AND STATUS

Post-irradiation examination using advanced microscopy techniques (atom probe tomography) continues the samples previously irradiated under the neutron-irradiation campaign. These results are providing detailed data on the local compositional variations – particularly that of oxygen – that is well known to have a strong effect on the superconducting properties of the material.

To investigate the effects of gamma irradiation on the HTS materials, a tape of the rare-earth doped Zr-$(Gd_x,Y_{1-x})Ba_2Cu_3O_{7-x}$ coated superconductor was procured from SuperPower. In this material, a high number density of nanoscale $BaZrO_3$ (BZO) particles are aligned with the *c*-axis of the crystal structure providing strong H//c pinning. This results in very high "out of the box" critical current densities due to the optimization of the size and number density of the BZO particles. Small lengths (approximately one inch) were cut from the tape and a gate structure was etched into the top surface of the material using a laser engraving system. This resulted in the formation of a bridge in the material that was 10 mm long and 3 mm wide.

The samples were then exposed to a Co-60 γ irradiation source at room temperature. The source dose was measured before and after each irradiation step and integrated for a total dose measurement. At each dose step, the samples were characterized for critical current density in a varying field and varying angle in a 0.5 T magnet test station. The results are shown in **Figure 53** and **Figure 54**.
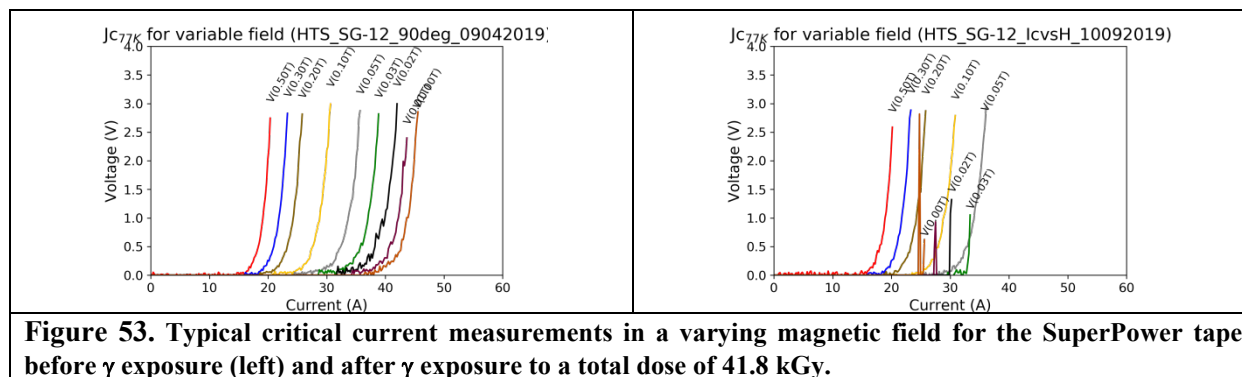
Figure 53. Typical critical current measurements in a varying magnetic field for the SuperPower tape before γ exposure (left) and after γ exposure to a total dose of 41.8 kGy.
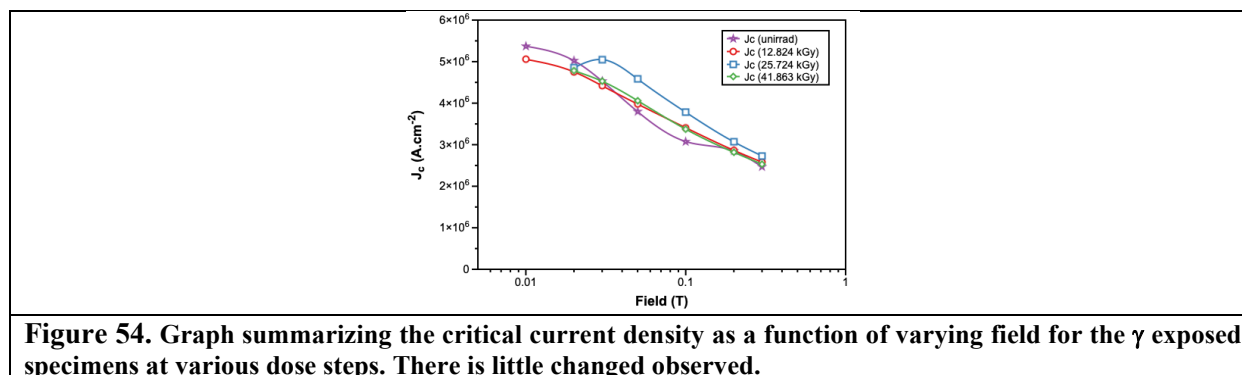
Figure 54. Graph summarizing the critical current density as a function of varying field for the γ exposed specimens at various dose steps. There is little changed observed.

The data displayed in these figures show there is little change in the superconductivity due to γ exposure up to a total dose of 41.8 kGy. However, Co-60 has a discrete spectrum consisting of only two energies of γ, different from the fusion system applications whereby a mixed spectrum would be expected. While this shows that there is promise that the γ exposure may not be a large problem, more work is needed to verify this tentative conclusion.

FUTURE PLANS

These initial results show promise that γ exposure may not be a degradation concern for high temperature superconductors, but there are limitations on the use of the Co-60 sources for this evaluation. If funding becomes available to continue this work, a series of irradiations using the Gamma Irradiation Facility (GIF) at ORNL would provide a mixed γ spectrum more like that expected in a service environment. It is also highly desirable to examine the effects at cryogenic temperatures; that effort will require the design and construction of a cryogenic irradiation station for the GIF.

8.   ADVANCED MANUFACTURING

8.1   ADDITIVE MANUFACTURING: ELECTRON BEAM MELTING OF TUNGSTEN DIVERTOR COMPONENTS

Betsy Ellis (ellisea@ornl.gov), John Echols, Christopher Ledford, Sullivan Figurskey, Timothy Horn, Chris D. Rock, Lauren Garrison, Michael Kirka, Yutai Kato, Ryan Dehoff

OBJECTIVE

The purpose of this project is to evaluate the electron beam additive manufacturing technique for manufacturing tungsten divertor components.

SUMMARY

Sample tungsten parts have been produced by Additive Manufacturing (AM) using electron beam melting. Start plate material, scan strategy, and process parameters producing dense material were identified, and blocks have been manufactured to be used for characterization, including mechanical testing.

PROGRESS AND STATUS

One technique of Additive Manufacturing is electron beam powder bed fusion, or electron beam melting (EBM). The EBM uses an electron beam to sinter and melt successive layers of metal powder to produce a desired shape, allowing the manufacture of parts with high geometric complexity, minimal material waste, and rapid turn-around times. In the case of difficult-to-fabricate metals such as tungsten, EBM also offers the potential to manufacture components that cannot be made using traditional techniques. This report details efforts in using EBM to produce tungsten parts suitable for use in the divertor of a fusion reactor, with the HEMJ tile design chosen as a proof-of-concept geometry.

All trial components were manufactured in an Arcam Q10+ electron beam melting system using plasma-atomized 99.99% tungsten powder with mesh size -90 +45 μm. Start plates were Ti-6Al-4V and layer thickness was 70 μm. Beam current during melting was 21 mA for all builds, with scan strategy, beam speed and spot size varied to explore resulting changes in the structure of the resulting product.

Titanium alloy start plates were chosen to improve adhesion to the build plate, as W and Ti form a continuous solid solution, and the limited thermal conductivity of the Ti alloy helps to retain heat at the build surface. To accommodate the lower melting point of Ti, scan speed was increased for the first several layers, then gradually reduced to achieve energy densities appropriate for melting W. This resulted in an intentionally porous support structure at the base of each build, before transitioning to melt parameters of interest.

The EBM framework offers great flexibility in scan strategy. For this work, both a traditional raster scan and a contour scan strategy were evaluated. When melted using a traditional raster scan strategy, line length varies dramatically during the first few layers of the build, resulting in unequal temperature distributions and leading to delamination. To alleviate this, a contour melting strategy with a triangular pattern was used instead. The beam path follows the outer perimeter of each triangle and continues melting the interior of the triangle in the same pattern, ending at the center of the triangle. This scan strategy equalizes the energy distribution and promotes adhesion to previous layers.

Several trial parts were printed using the HEMJ tile cap geometry, to begin the evaluation of EBM parameters. *Figure 55* shows photographs of four of these parts, and cross sections of two of them revealing the distribution of porosity.
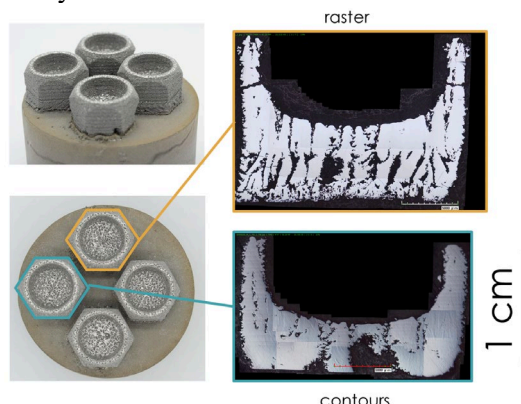
Figure 55. Exploratory divertor tile prints showing the effect of scan strategy. A standard raster scan strategy results in hot spots and delamination, while a contour scan strategy allows more uniform distribution of heat and consequently higher density.

To identify ideal melt parameters for tungsten, arrays of blocks with different energy densities and beam shapes were produced. This was accomplished by varying the beam speed and focal point, while keeping all other variables unchanged. Increasing spot size and decreasing speed tend to decrease porosity, as shown in the micrographs in *Figure 56*. The specimen at the bottom right, with the largest spot size and slowest beam speed, shows a large region of essentially zero porosity at the top of the sample.
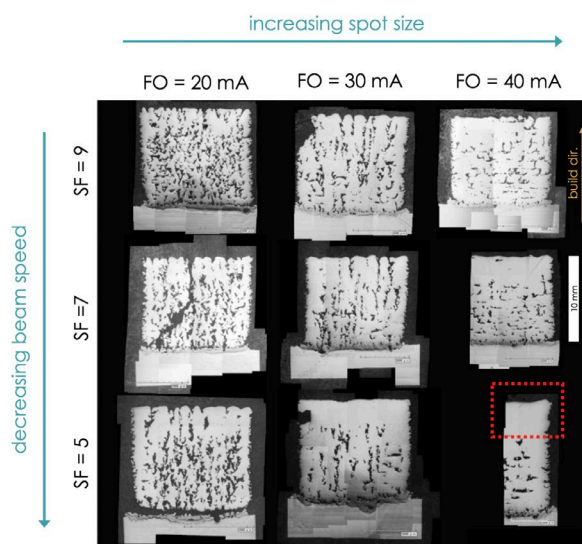
Figure 56. Optical micrographs of cross-sections of exploratory W builds. The beam speed (speed function, SF) and size (focus offset, FO) were systematically varied to identify process parameters giving rise to fully dense material. At lower right is the selected parameter set, which produced fully dense W atop an intentionally porous support structure.

Electron backscatter diffraction was performed on the densest sample (at lower right in *Figure 56*). The results reveal a columnar grain structure, shown in *Figure 57*. Long axes of grains are oriented parallel to the build direction in the center of the part and are tilted slightly away from the build direction at the edges. A mixed (111)/(100) texture dominates.
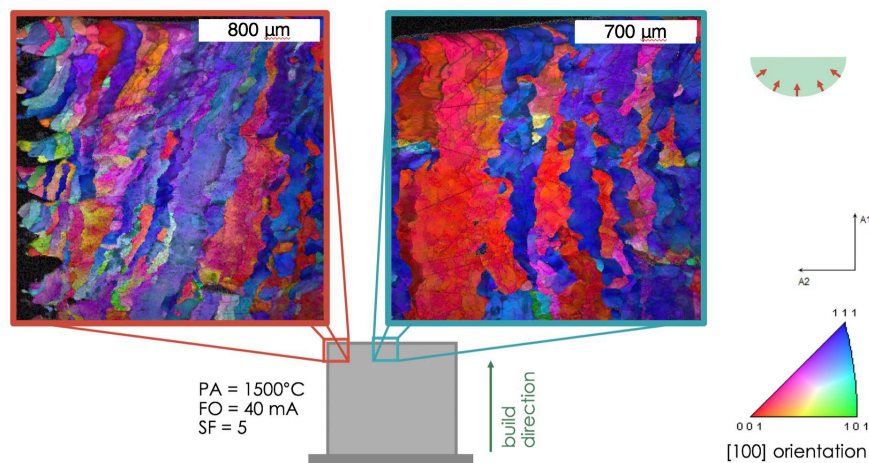
Figure 57. EBSD results showing orientation parallel to the build direction in the dense AM W sample from the lower right of Figure 56.

FUTURE PLANS

Parameters selected above were used to produce the solid W blocks shown in ***Figure 58***. These will be used for fabrication of tensile test specimens. Hot isostatic pressing will be used to reduce residual porosity, and both hipped and un-hipped samples will be tensile tested to measure strength and ductility. Some porosity remains in these larger samples, so one goal of continuing research will be further refinement of process parameters to produce larger regions of full density.
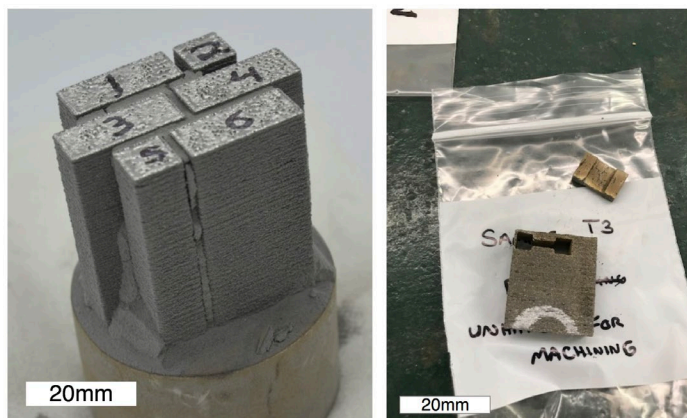
Figure 58. AM W blocks for tensile testing, left, and samples removed for tensile testing, right.

8.2   ADDITIVE MANUFACTURING: FABRICATING ADVANCED IRON ALLOYS

Niyanth Sridharan, Tim Graening (graningt@ornl.gov)

OBJECTIVE

This work is directed at evaluating the applications and advantages of advanced manufacturing (AM) techniques in fabricating ferritic martensitic steels components suitable for use in fusion reactor components. The goals of this program are therefore three-fold:

i)   Document the performance of existing alloys fabricated via AM with the goal of identifying challenges in fabricating current alloys by AM.
ii)   Develop a procedure for high throughput alloy design for AM.
iii)   Develop process-based qualification techniques for ferritic martensitic steels components produced by AM.

INTRODUCTION

The AM is a disruptive manufacturing process which has found widespread adoption in the automotive, aerospace and fossil fired power industries[1]. However, the fusion materials community is just beginning to evaluate taking advantage of the seeming benefits of AM. This is due to the difficulty in qualification of AM processes, non-availability of data to benchmark performance of alloys fabricated via AM with those of the wrought counterparts and finally the lack of new materials developed specifically for AM.

This work package was launched to fulfill the first objective. An Fe-9Cr-2W alloy developed at ORNL for conventional processes was utilized to fabricate coupons for evaluation[3].

EXPERIMENTS

Four identical (40x40x10 mm^3) samples were fabricated using the Fe-9Cr-2WV alloy with the chemistry listed in *Table 8*, using BeAM laser blown powder DED Modulo 450 with a laser power of 700 W and travel speed of 700 mm/min.

Table 8. Composition of the alloy used for fabrication

	Fe	Cr	W	V	Ta	C	Mn	N
ORNL 9Cr-2W alloy	Bal	9.0	2.0	0.25	0.07	0.10	0.40	0.025

Following fabrication three samples were normalized and tempered using different conditions. The conditions used were:

i)   HT-1: 980°C normalize for 30 minutes + Temper at 750°C for 2 h.
ii)   HT-2: 1150°C normalization for 60 minutes + Temper at 750°C for 60 minutes.
iii)   HT-3: 1150°C normalization for 20 minutes, subsequent forced air cooling + Temper at 750°C for 30 minutes.

The heat treatments were performed in an Ar atmosphere to avoid oxidation of the samples. This was then followed by a detailed characterization campaign at various length scales from the optical microscope, SEM, EBSD and TEM to investigate the prior austenite grain structure, martensite packet and block sizes, lath sizes and the fine structure of the precipitates.

RESULTS

Representative results of the characterization of the materials produced by AM, and the effects of the different heat treatments, are shown in ***Figure 59***. The samples in the as-fabricated condition showed presence of delta ferrite and a columnar prior austenite grain structure. Formation of delta ferrite in these steels has been well studied and documented. There are almost no precipitates in the as printed structure which is surprising considering that previous work performed using HT9 and grade 91 showed significant MX and $M_{23}C_6$ carbides in the as-printed state. This might be due to the higher W and N in the steel, both of which increase the tempering resistance of the steel, necessitating the use of long-term tempering treatments to achieve the required precipitate density. Therefore, to eliminate delta ferrite and increase the precipitate density detailed heat treatments were performed. The results show that low temperature normalization did not eliminate the delta ferrite and accelerated the recrystallization of the martensite lath structure. Higher austenitizing temperatures while effective at reducing the delta ferrite content resulted in significant grain growth. The results showed that a higher austenitizing temperature at lower times followed by aging at 750˚C gave the optimum size distribution and number density of precipitates. Among the conditions explored, the optimum normalizing and tempering treatments for this steel and this geometry is 1150˚C-30 minutes followed by tempering at 750˚C for 0.5 h.
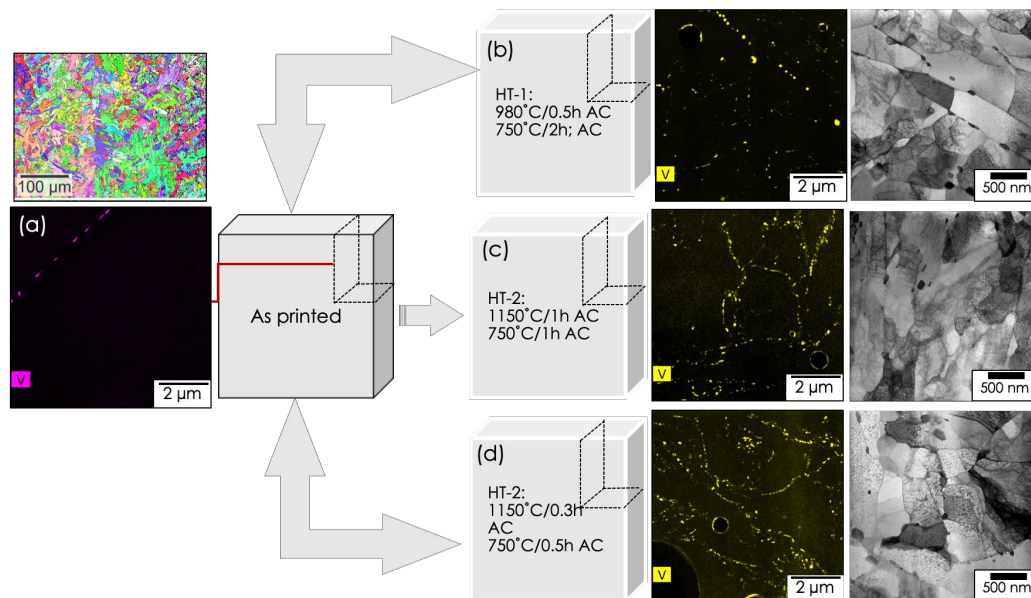
Figure 59. Overview of processing-post processing-microstructure relationship in ORNL 9Cr-2WV alloy (a) TEM and EBSD of the as printed part (b) STEM EDS and TEM micrographs.

Uniaxial tensile tests were performed to evaluate the material mechanical properties. Tests were performed at RT, 500, 600 and 700˚C perpendicular to and in the print direction. The results in ***Figure 60*** show comparable performance to that of the wrought alloy counterparts. However further improvements in high temperature strength need be archived, probably by refining the precipitate through tailoring the alloy composition and adjusting the printing process to decrease the porosity. Fracture toughness and creep tests will be performed with an improved version of alloys created based on this investigation.
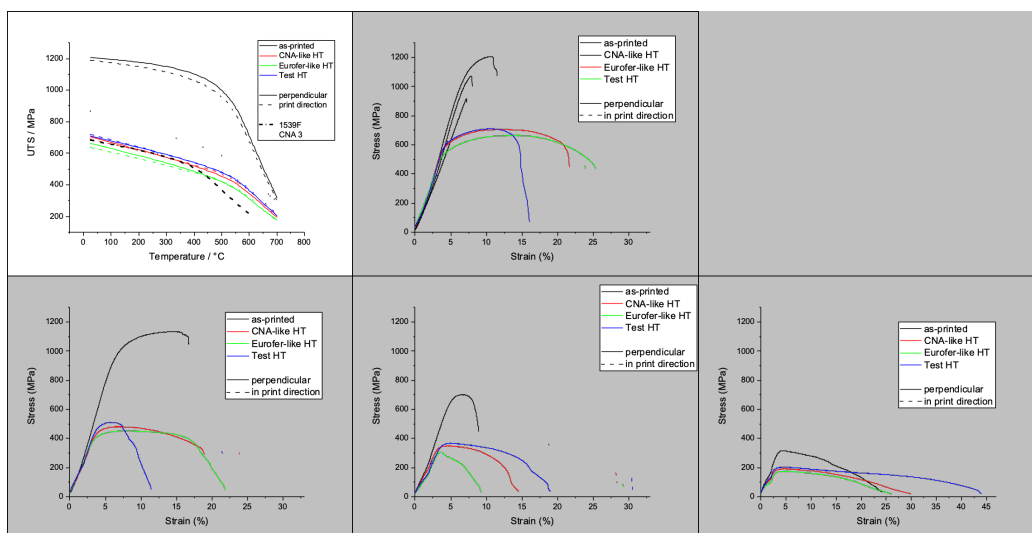
Figure 60. Summary of the mechanical tests performed at room temperature and high temperature. Figure (a) compares the performance of the Fe-9Cr-2W alloy with the newly developed CNA.

FUTURE ACTIVITIES

Further testing to investigate the toughness of the printed alloys will be performed to understand the nature of the scatter in the mechanical properties data. Further optimization of the chemistry of the alloy to increase the number density of precipitates and refine the processing parameters is in progress.

9.   COMPUTATIONAL MATERIALS SCIENCE

9.1   MECHANICAL PROPERTIES AND RADIATION EFFECTS IN FUSION MATERIALS

Y. Osetskiy (osetskiyyn@ornl.gov)

OBJECTIVE

The objective of this task is to obtain a better understanding of the atomic-scale mechanisms operating in fusion materials. Two main groups of effects are under consideration: the mechanisms of radiation damage and the properties of irradiated materials. The main materials studied are ferritic and stainless steels and tungsten-based alloys.

SUMMARY

Comparison of strengthening due to different radiation-induced microstructures was investigated using large-scale atomistic modeling. Voids, He-filled bubbles, Cu-precipitates, impenetrable obstacles (imitating oxide particles), in a bcc Fe matrix and initially coherent Re-rich precipitates in tungsten were modeled as obstacles to edge dislocation glide. A wide range of model and environmental parameters was tested, including obstacles size and position relatively to the dislocation slip plane, ambient temperature and the dislocation speed. Several conclusions were formulated, and conditions that result in maximum possible strengthening are suggested. The results were reported in invited presentations at 6th FM TCP workshop on theory and modeling of nuclear fusion materials (Walla Walla, WA, June 24-26, 2019) and ICFRM-19 (San Diego, October 28-November 2, 2019).

PROGRESS AND STATUS

The plastic behavior of irradiated metals and alloys is controlled by dislocation glide through a field of dispersed obstacles, including forest dislocations or solute atoms introduced during fabrication and modified during irradiation. The existence of several obstacle types operating together is common at radiation conditions. The usual set of obstacles include *inclusion-type* obstacles such as voids and bubbles, secondary phase precipitates, oxides, carbides, etc., *dislocation-type obstacles* such as dislocations, dislocation loops and stacking fault tetrahedra and solute atoms that provide an additional *solute strengthening* contribution. In some important cases many dislocation-type obstacles, such as large, >10nm dislocation loops and stacking fault tetrahedra, act like and can be treated as inclusion-type defects. Therefore, in this work we consider only the localized inclusion-type obstacles for simplicity. This type of obstacles was considered in numerous models over many decades using elasticity theory aimed at predicting materials yield stress caused by irradiation-induced defect density and size. The first models were based on the concept of dislocation line tension, accounting for simple statistical approaches for dislocation obstacle distributions and interactions. In the original version of the dispersed barrier hardening (DBH) model the critical shear resolved stress (CRSS), τ_c, for the dislocation passing through a set of obstacles of diameter D with number density N, is written as $\tau_c = \mu b \sqrt{ND}$ [1]. The original DBH could be generalized for polycrystals and modified to include the obstacle strength factor, α, (see e.g. [2]):

$$\tau_c = M\alpha\mu b\sqrt{ND} \qquad (1)$$

here *M* is the Taylor factor (3.06 for non-textured BCC and FCC metals [9]), μ is the shear modulus, *b* is the value of Burgers vector of the primary glide dislocations. Many radiation hardening studies have used the DBH model, eq.(1) or its modifications [3-5], for data interpretation by choosing the appropriate value

of the obstacle strength factor α. The strength factor is usually taken as constant for different obstacles independent of cluster size, which is a very rough assumption, however. The knowledge of obstacle strength is necessary to predict materials hardening and there were many attempts both experimental and theoretical to estimate its value for different obstacles. Typically, "strong" obstacles are associated with $\alpha \approx 0.25 - 1.0$, where $\alpha = 1.0$ is expected to be the strongest, "Orowan", obstacle with maximum CRSS $\sim \mu b/L$ (here $L = 1/\sqrt{ND}$ is taken as the distance between obstacles). Thus, the experimentally estimated value for faulted dislocation loops resulted in $\alpha \approx 0.5 - 0.4$ at irradiation temperatures of 110°C and 200-275°C, respectively [6]. TEM and tensile data, attributed to the small {001} defects in V-4Cr-4Ti tensile specimens irradiated at 390-415°C [7], deduced $\alpha \approx 0.25$. Obstacle strength of up to 0.8 was estimated in [8] for dislocation loops, precipitates and voids formed under neutron irradiation at 300°C in different ferritic alloys. Experimental determination of α usually is by fitting to a relatively simple model, such as eq.(1) and its variations [9], and still is based on the constant obstacle strength assumption.

Predicting applications of barrier hardening models for a long time were based on dislocation line tension approximation. In these, balancing the constant line tension and critical stress when the dislocation breaks away, $\alpha = \cos\left(\frac{\varphi_c}{2}\right)$ where φ_c is angle between the arms of the dislocation at an obstacle [9]. This angle varies from π - the obstacle strength is zero, to "0" - the "Orowan" obstacle of maximum strength. Foreman Makin model [9] was highly use for decades in modeling flow stress for distributions of different obstacles.

Deeper understanding of strengthening behavior was achieved in a series of dislocation-obstacle modeling approaches reported in [10,11] where the realistic self-interaction between dislocation segments was considered. Treating the results for the periodic array of strong obstacles i.e. $\alpha = 1$, interacting with edge and screw dislocations, Bacon, Kocks and Scattergood (BKS) obtained the following expression for CRSS (omitting the Taylor factor):

$$\tau_c = A \frac{\mu b}{L} \left[ln(D^{-1} + L^{-1})^{-1} + B \right] \qquad (2)$$

here $A = 1/2\pi$ and $A = 1/2\pi(1 - \nu)$ for edge and screw dislocations respectively, B is a constant characterizing interaction between the dislocation and obstacle surface, related to the surface energy, and ν is the Poisson ratio. For treating weaker than "Orowan" obstacles, e.g. $\tau_c = \alpha\mu b/L$ with $\alpha < 1$, the obstacle strength can be derived as:

$$\alpha = A[ln(D^{-1} + L^{-1})^{-1} + B] \qquad (3).$$

This expression introduces a significant correction to the effective strength due to the dislocation self-interaction that depends now on D and L.

Using large-scale atomistic modeling we can parameterize the parameter α for the case of different obstacles. The results on critical resolved shear stress (CRSS) obtained by MD modeling for different obstacles interacting with an edge dislocation at 300K are presented in *Figure 61* as function versus harmonic mean of the obstacle diameter, D, and distance between obstacle centers, L. In this presentation the obstacle strength α is just a slope of dependence for an obstacle type. Thus, voids and bubbles are very well approximated with the red line on *Figure 61*, which is a theoretical prediction for an edge dislocation [10,11]. The Cu-precipitates, the yellow line, are also consistent with edge dislocation predictions if the structural transformation occurring during interaction with precipitates $D > 4$ nm is considered. However, rigid obstacles, approximated by the black line, show much stronger slope and,

thus, the obstacle strength parameter is stronger than the strongest prediction from the theory e.g. screw dislocation behavior.

Atomic-scale dislocation obstacle interaction modeling results in the values for the obstacle strength parameters for different obstacles, given in ***Table 9***.

Table 9. Obstacle strength parameters calculated for several defect classes

obstacle	Theoretical prediction	Estimated from MD	Low dislocation density approximation
Voids	edge	$0.11[ln(D^{-1} + L^{-1})^{-1} + 0.40]$	$0.11[lnD + 0.4]$
He-bubbles	edge	$0.11[ln(D^{-1} + L^{-1})^{-1} + 0.40]$	$0.11[lnD + 0.4]$
Cu-precipitates	corrected edge		
<4nm		$0.11[ln(D^{-1} + L^{-1})^{-1} + 0.15]$	$0.11[lnD + 0.15]$
>4nm		$0.11[ln(D^{-1} + L^{-1})^{-1} + 0.37]$	$0.11[lnD + 0.37]$
Rigid inclusions	-	$0.20[ln(D^{-1} + L^{-1})^{-1} - 0.7]$	$0.20[lnD - 0.7]$
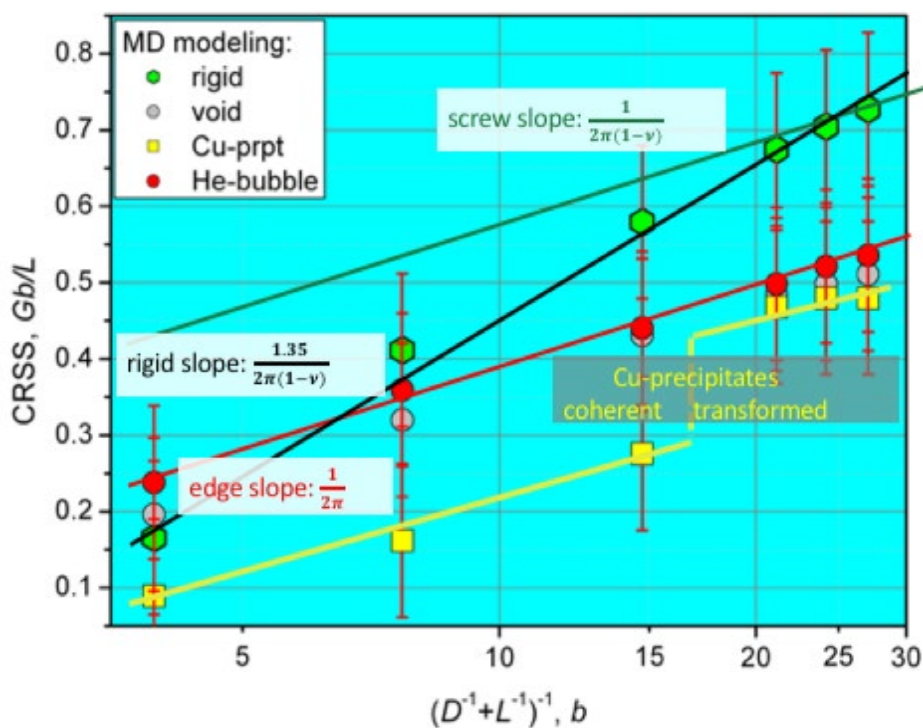
Figure 61. The CRSS obtained from MD modeling of an edge dislocation interacting with different obstacles presented as function of harmonic mean of the obstacle diameter, D, and distance between obstacle centers along the dislocation line, L. The red line is theoretical prediction for an edge dislocation, green line is theoretical prediction for a screw dislocation, green line is a linear approximation for rigid obstacles and yellow line is an edge dislocation dependence broken to account for the structural transformation in Cu precipitates.

Note that obstacle dimeter D in ***Figure 61*** and the above table is measured in dislocation core radius, that is taken here as $|b|=0.248$ nm ($b=1/2a<111>$). Thus, for example, $\alpha=0.38$ for 4 nm void and $\alpha=0.42$ for the same size rigid inclusion. Larger sizes lead to large difference, e.g. for 10 nm voids and rigid inclusions $\alpha=0.45$ and $\alpha=0.60$ respectively.

A publication on the estimation of the obstacle strength parameter α using MD data is in preparation.

FUTURE PLANS

This research will continue modeling obstacles in other materials and environmental conditions including temperature, strain rate and multiple obstacles. Contributions from thermally activated processes will be also studied. The final aim is to obtain a robust approach for estimation of the obstacle strength parameter α.

REFERENCES
[1.] A. Seeger, Radiation damage in solids, IAEA, Vienna 1, 101 (1962).
[2.] F. Kroupa, P.B. Hirsch, Elastic interaction between prismatic dislocation loops and straight dislocations, Discuss. Faraday Soc. 38 (1964) 49e55.
[3.] R.E. Stoller, S. Zinkle, On the relationship between uniaxial yield strength and resolved shear stress in polycrystalline materials, J. Nucl. Mater. 283-287 (2000) 349-352.
[4.] L. Tan and J.T. Busby, Formulating the strength factor a for improved predictability of radiation hardening, Journal of Nuclear Materials 465 (2015) 724e730.
[5.] P.M. Rice, S.J. Zinkle, <u>Temperature dependence of the radiation damage microstructure in V– 4Cr–4Ti neutron irradiated to low dose</u>, J. Nucl. Mater. 258–263 (1998) 1414.
[6.] Jaime Marian, et al., MD modeling of defects in Fe and their interactions, *J. Nucl. Mater.* 323 (2003) 181–191.
[7.] L.L. Snead, et al., Presented at 8th Int. Conf. on Fusion Reactor Materials, Sendai, Japan, 1997; Fusion Materials Semiann. Prog. Report for period ending December 31 1997, DOE/ER-0313/23, p. 81.
[8.] Lambrecht M, et al., On the correlation between irradiation-induced microstructural features and the hardening of reactor pressure vessel steels J. Nucl. Mater. 406 (2010) 84–9.
[9.] A.J.E. Foreman, M.J. Makin, Dislocation movement through random arrays of obstacles, Philos. Mag. 14 (1966) 911.
[10.] D. J. Bacon , U. F. Kocks and R. O. Scattergood, The effect of dislocation self-interaction on the Orowan stress, Philos. Mag., 28 (1973) 1241-1263.
[11.] R.O. Scattergood and D.J. Bacon, The strengthening effect of voids, Acta. Metall., 30 (1982) 1665.

9.2　UNDERSTANDING DEFECT DIFFUSION IN TUNGSTEN-BASED ALLOYS

Y. Osetskiy (osetskiyyn@ornl.gov), G. Samolyuk

OBJECTIVE

The purpose of this research is to understand the defect and atomic transport in W-based alloys under irradiation conditions. We use conventional atomistic techniques and density functional theory (DFT) to study the dynamic properties of point defects and defect clusters, atomic transport due to defect diffusion, segregation and precipitation in the W-Re-Os system.

SUMMARY

Diffusion of interstitial atoms was modeled in W and W-Re alloys. It was found that the presence of Re atoms significantly decelerates the total diffusion. The effective activation energy for trace diffusion is controlled by the binding energy between an interstitial atom and a Re impurity atom. No fast diffusion of Re by an undissociated mechanism as suggested in the literature was observed. The results were presented at ICFRM-19 (San Diego, October 28-November 2, 2019).

PROGRESS AND STATUS

Interstitial diffusion in W and W-Re alloys was studied by MD modeling with a set of interatomic potentials described in [1]. These potentials were fitted to a wide range of experimental and DFT data. The main deficiency of these potentials is overestimated stability of W-Re <110> dumb-bell that is ~0.18eV against ~0.02eV obtained from first-principle modeling. This, in principle, may affect current results that will be verified by *ab initio* MD modeling.

Here we present preliminary results of extensive modeling of interstitial defect diffusion in W-based alloys. We have modeled thermally activated migration of interstitial atoms in bcc pure W and alloys with 1.0, 2.5 and 5.0 at.% Re. The general approach to treating MD data is described elsewhere where we operated mainly with self-diffusion coefficients, D^*, D^*_W and D^*_{Re}, that are defined by treating atomic square displacements (ASD) as a function of simulated time, t (see [1,2] for details). For the tungsten materials we treated long trajectories of up to $>2\times10^6$ jumps of the interstitial atom modeled over a few hundred *ns* physical time. Interatomic interactions were described using IAPs developed for the W-Re system in [3]. These IAPs are fitted to a wide range of properties of pure metals and alloys and ensure qualitatively correct behavior of point defects in the W-Re bcc alloys.

Currently we are studying the interstitial atom (IA) diffusion mechanism. The IA in pure W has a ground state configuration as a <111>-crowdion and performs fast, preferentially one-dimensional, diffusion along the <111> direction. At high temperatures the frequency of crowdion rotation increases making the total diffusion three-dimensional. This motion changes dramatically when Re is alloyed with the W matrix, with binding energy between IA and Re in the W matrix of ~0.8 eV [4]. This high energy tightly
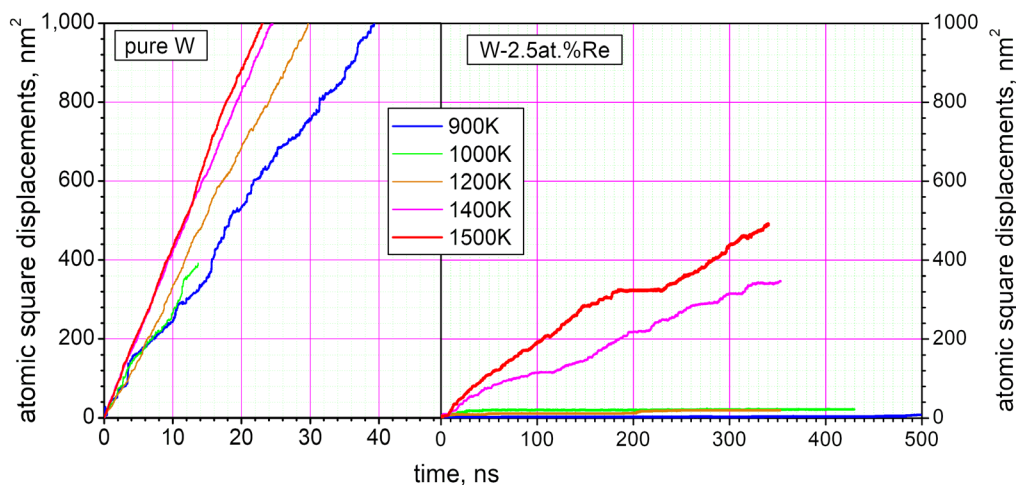
Figure 62. Temporal evolution of atomic square displacement (ASD) in a 4396-atom crystal of pure W (left) and W-2.5 at.%Re initially random alloy during IA diffusion at different temperatures. Note one order in magnitude difference in the scale of the time axis.

binds the Re solute to the IA, and very much affects its diffusion. An example of temporal evolution of atomic square displacement (ASD) in a crystal of W-2.5 at.%Re random alloy during IA diffusion at different temperatures is presented in ***Figure 62***. This shows that the ASD(t) dependence is quite rough and consist of segments with either complete immobility or fast motion (increasing ASD). The former is related to strong biding between the Re solute and interstitial atom configuration, the later reflects a fast IA migration towards the next Re solute atom. Only at the highest temperature studied, 1500K, does ASD(t) come close to a linear function.

Tracer diffusion coefficients calculated for W and all alloys studied here are presented in **Figure 63** as Arrhenius-type plots with the effective activation energies indicated. Note the dramatic increase of the tracer diffusion activation energy from 0.101 eV in pure W to >1 eV in alloys. This reflects the high binding energy between the Re solute and an interstitial defect in the W matrix. This is an important feature of W-Re system for it strongly affects alloys behavior under irradiation. For example, Re segregation should be strongly controlled by interstitial diffusion. We have studied this mechanism and revealed that an interstitial atom drags Re along its diffusion trajectory. The evidence for this is presented in ***Figure 64*** where we plot the mean ratio Re-to-W atoms in each interstitial configuration that appears during migration in all alloys studied. At low T<1200K in both alloys this ratio is close to unity, indicating that the IA is a mixed W-Re dumbbell. This is in principle fully consistent with a high stability of this dumb-bell configuration calculated by *ab initio* and reproduced with the IAPs used here [3]. At higher temperatures the dumb-bell chemistry evolves differently in each alloy. In dilute 1.0 at.% Re alloys purer W-W interstitials appear due to thermal dissociation of W-Re configurations: then the Re/W ratio drops below unity. In the more concentrated 5 at.%Re alloy IA chemistry evolution is different: the

Re/W ratio increases above unity. This means that the number of Re-Re interstitial configurations increases because of the local rearrangement due to more frequent migration of interstitial defects. Note that we modeled up to $>2 \times 10^6$ defect jumps. This high number of jumps helps reveal the certain clustering of Re due to their strong attraction to interstitial defects. This is clear evidence that even at the molecular dynamics time scale, random W-Re alloys are unstable and undergo Re precipitation. A possible mechanism of formation and growth of Re precipitates due to interstitial defects diffusion was studied recently [5] using kMC technique at the mesoscale.

More accurate mesoscale study of precipitation and phase transformations in W-Re alloys under irradiation conditions will be performed in future using diffusion theory and kMC modeling and utilizing the mechanisms and diffusion parameters obtained by molecular dynamics modeling. However, although
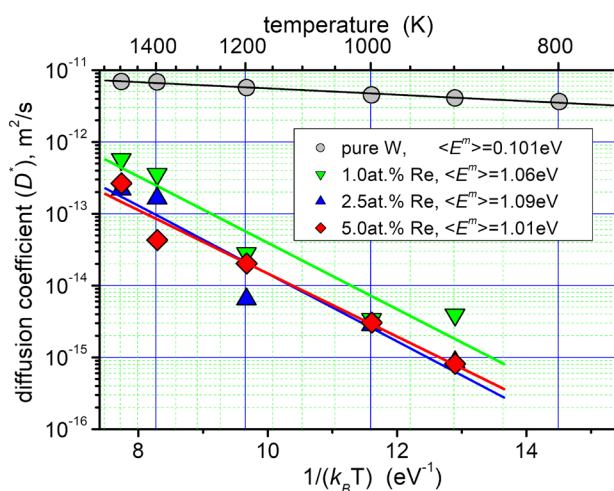
Figure 63. Tracer diffusion coefficients calculated for pure W and 1.0, 2.5 and 5 at.% Re alloys as a function of the reciprocal temperature. The insert indicates the corresponding effective activation energies.

the mesoscale approach allows the expansion of time and spatial scales for phenomena studied such as diffusion, segregation, precipitation and phase transformations, the detailed atomic-scale mechanisms still need to be identified by atomistic modeling. For example, we will investigate interstitial diffusion
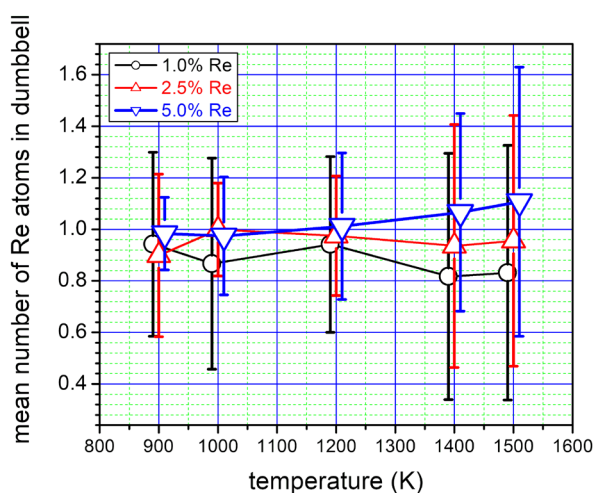
Figure 64. Mean ratio of Re-to-W atoms in each interstitial configuration that appeared during migration in both alloys as a function of ambient temperature. Error bars indicate standard deviation of the mean estimated over ~10^6 instant configurations that appeared after each IA jump.

mechanisms in W-Re systems using direct DFT-based molecular dynamics. Of course, DFT-MD does not allow us to model long-range diffusion as we can do by classical MD, however it helps in identifying

the elementary mechanisms and validation of the empirical IAPs used here. Further progress in this direction depends mainly on the availability of interatomic potentials for the alloys and compositions to be studied.

APPLICATION

The results of this research will be used for predictive modeling of phase stability in W-Re systems under irradiation. This work is currently continuing.

FUTURE PLANS

Kinetic Monte Carlo (kMC) modeling of vacancy and interstitial atom diffusion in W-Re alloys and Re-precipitation will continue. A DFT-based MD study of the fundamental mechanisms of Re diffusion in W-Re alloys will use validated interatomic potentials and will accumulate data for fitting new interatomic potentials for the W-R-Os systems.

REFERENCES

[1.]　Osetsky Y.N., Atomistic study of diffusional mass transport in metals. *Defect and Diff. Forum*, **188-190**, 71-92 (2001).

[2.]　Osetsky Y.N., *et al.*, On the Existence and Origin of Sluggish Diffusion in Chemically Disordered Concentrated Alloys. *Curr. Opin. Solid State Mater. Sci*. **22,** 65-74 (2018).

[3.]　Bonny G., Bakaev A., Terentyev D., and Mastrikov Yu.A., Interatomic potential to study plastic deformation in tungsten-rhenium alloys, *J. Appl. Phys.,* **121,** 165107 (2017).

[4.]　Suzudo T., Yamaguchi M. and Hasegawa A., Stability and mobility of rhenium and osmium in tungsten: first principles study, Model. Simul. Mat. Sci. Eng., 22 (2014) 075006.

[5.]　Huang C-H., Gharaee L., Zhao Y., Erhart P., and Marian J., Mechanism of nucleation and incipient growth of Re clusters in irradiated W-Re alloys from kinetic Monte Carlo simulations, *Phys. Rev.* B **96**, 094108 (2017).

9.3   THE PHASE STABILITY OF PRECIPITATES IN TUNGSTEN ALLOYS

G. Samolyuk (samolyukgd@ornl.gov), Y. Osetskiy

OBJECTIVE

Neutron irradiation results in the transmutation of tungsten atoms to rhenium and osmium. These atoms segregate and together with original W atom form precipitates of structure. It was observed by Chad Parish that under irradiation the precipitates are ordered in a Laves phase structure with composition $WRe_{0.6}Os_{0.4}$ at lower doses and in a hexagonal structure with composition $ReOs_2W$ at high doses. According to previous first principles calculations the hexagonal structure has energy lower by 0.12 eV per atom than the χ structure, and that that the σ phase is more stable than Laves by 0.23 eV per atom. A simple thermodynamic approach is not adequate to explain the observed stability of the Laves phase. Thus, the investigation of phase stability, precipitation and mass transport in W-based materials during irradiation must be expended to large scale atomistic modeling using the new interatomic W, Re, Os potentials. The pure tungsten interatomic potential has been developed within SEED money proposal "*General framework for the development of predictive atomistic force fields and application to multicomponent alloys*". We are now extending this activity to development of Re and W-Re interatomic potentials.

SUMMARY

Our previously developed approach to obtaining interatomic potentials was applied to rhenium. This approach is based on accurately reproducing modeling system trajectories obtained within density functional theory (DFT) calculation by the system of interactions described by interatomic potentials for series of temperatures. For this purpose, a large series of DFT molecular dynamics (MD) calculations of pure systems ordered in hcp, bcc and fcc crystal structures and systems with typical defects have been executed. This data set has been extended by static DFT calculation of defects energetic, energy of three crystal structures, elastic constants, and the equations of state. The initial justification of the rhenium potential developed has been started.

PROGRESS AND STATUS

The general framework developed for interatomic potentials is based on reproducing the system trajectories at different temperatures. Together with system trajectories the information on static configuration DFT results are incorporated as a constraint. The latter is important to model system with defects and different types of precipitates. The calculated properties are summarized in ***Table 10***.

Table 10. Calculated properties of rhenium using the interatomic potential

Structure	System or property	Static/Dynamic (T, K)
hcp	Equation of state	Static (96 atoms)
	perfect	T=300, 2700, 3700
	Defect: BO	T=0, 300, 2700
	Defect: vacancy	T=0, 300, 2700
	Defect: M configuration	T=0, 300, 2700
	Defect: O	T=0, 300, 2700
	Defect: S	T=0, 300, 2700
Liquid	Liquid	T=2700, 3700, 5000
bcc	Perfect	T=300, 2700
fcc	Perfect	T=300, 2700
σ-phase	Perfect, static	T=0

FUTURE PLANS

The series of DFT MD calculation at different temperatures will be executed for W-Re interstitial defect dynamics. This series of calculations pursue double goals: It will be used as input to develop a W-Re interatomic potential and will also allow addressing the question of the W-Re interstitial diffusion mechanism. The newly developed potential will be used in large scale atomistic modeling of precipitation processes in W-Re alloys.

9.4   THERMODYNAMICS OF COMPLEX MULTI-PHASE FUSION ALLOYS

G. Samolyuk (samolyukgd@ornl.gov), Y. Osetskiy

OBJECTIVE

The objective of this task is to develop an approach which allows investigation of the thermodynamic stability of multiphase alloys and defect distributions in the alloys based on first principles. This new approach should allow the investigation of the defect concentration as a function of both the precipitate volume fraction and the size distribution; it also considers the specific orientation of the precipitate-matrix interface. In addition, it should be possible to extend it to systems in quasi-equilibrium state, for example in alloys with large concentrations of vacancies introduced by mechanical alloying, as these are preserved in this approach by applying additional constraint.

SUMMARY

This study describes evolution of a multiphase alloy from a state (referred to as a perfect state - for example, a matrix with a given density of precipitates with definite size and interfaces orientation) to an equilibrium state. These deviations are written as an expansion to a series of simple interacting defects, such as anti-sites, vacancies, or interstitials. This reduces the problem of describing the equilibrium state of a macroscopic number of atoms in the full multicomponent system to the description of the limited set of defects with their characteristic calculated from first principles. Recently the approach was extended to consider consideration of the defects at the interface of the precipitate and matrix. This new approach allows investigating the defect concentration as a function of both precipitate volume fraction and size distribution; it also considers the specific orientation of the precipitate-matrix interface. Herein we apply this approach to investigation of the equilibrium distribution of vacancies in a system containing yttria (Y_2O_3) nanoclusters in a bcc Fe matrix as a prototype of nanostructured ferritic alloys. The result obtained is that the main type of defect corresponds to vacancies localizes at the (100)Fe-O interface from the Fe matrix side. This interface is unstable with respect to production of vacancies – with high accuracy, each Fe atom closest to the precipitate Fe atom layer is replaced by a vacancy. The local concentration of vacancies at (100)Fe-Y interfaces is two orders of magnitude lower than at Fe-O interfaces and is very sensitive to size and fraction of the ODS particles and the alloy temperature. In contrast to the (100)Fe-O interface the so called Klim interface (Fe-Y) is extremely stable, i.e. the local vacancy concentration at this interface at 600 K is less than 10^{-12}.

PROGRESS AND STATUS

This thermodynamic approach has been used to obtain the system thermodynamic potential of the grand canonical ensemble. The equilibrium defect concentration is obtained by constrained minimization of the grand thermodynamic potential. The constraint is introduced to preserve the alloy composition which is defined by the total number of defects. To calculate the total amount of defect the geometric relationship between precipitate size, total volume fraction, interface orientation and number of possible defect positions has been estimated (see ***Figure 65***). Let fraction α of precipitate surfaces have [100] interface and $1 - \alpha$ have Klim interface. The area per atom for [100] interface is $S^{[100]} = a^2$, where a is the Fe

lattice parameter. If the shape of the precipitate is approximated by a sphere of radius $N_R a$ the area of the interface [100] is $\Sigma^{[100]} = \alpha 4\pi (N_R a)^2$. Thus, the number of possible vacancy positions in one layer of [100] interface is

$$N_v^{[100]} = \frac{\Sigma^{[100]}}{S^{[100]}} = \alpha 4\pi (N_R)^2,$$

while for Klim interface

$$N_v^{[\overline{1}\overline{1}2]} = \frac{\Sigma^{[\overline{1}\overline{1}2]}}{S^{[\overline{1}\overline{1}2]}} = (1-\alpha)4\sqrt{\frac{2}{3}}\pi N_R^2.$$

From the relationship for the number of precipitates, m, in the alloy $Fe_{1-x}(Y_2O_3)_x$ one can obtain $m = 2x\,N^3/\left(\frac{8}{3}\pi N_R^3\right)$ and the number of possible defect positions at the interface, vacancies for example, is

$$N_v^{[100]} + N_v^{[\overline{1}\overline{1}2]} = x\left[\frac{3}{2}\frac{\alpha}{N_R} + \sqrt{\frac{3}{2}}\frac{1-\alpha}{N_R}\right]2N^3.$$

These relations allow calculation of the total number of iron, yttrium, , and oxygen atoms in the system; and to close the system of equations for defect concentration by preserving system composition:
$\frac{N_{Fe}}{N_Y+N_O} = \frac{1-x}{x}$, $\frac{N_Y}{N_O} = \frac{2}{3}$.

The calculated local defect concentration as a function of alloy $(Y_{2/5}O_{3/5})_x(bcc\ Fe)_{1-x}$ composition, x, at two temperatures, T, 600 and 1200 K, and two sizes of precipitates, R, 10 and 100 bcc Fe lattice parameters, i.e. 2.87 and 28.7 nm, respectively are shown in *Figure 66*. Here, the size of precipitates changes simultaneously with change of precipitates number in order to preserve composition, x.
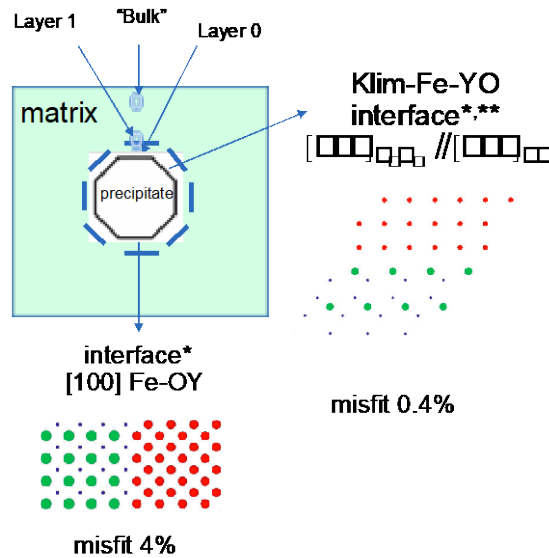
Figure 65. Structure of ODS precipitate interface.

As it can be seen in *Figure 66*, the local concentration of Fe vacancies in first layer of (100)Fe-OY interface, shown by green circles, equals one and does not depend on temperature, T, nor composition, x, nor size of precipitates, R. It is not surprising, considering the negative formation energy of -0.87 eV

(initial estimate). This is so small that even the sizable iron vacancy repulsion, 0.54 eV, is not able to stabilize this interface. Thus, after incorporation of this interaction within MFA, the initial estimate for vacancy formation energy increases, but is still negative, -0.33 eV. That makes iron vacancies at first layer of (100)Fe-OY interface the structural defect.
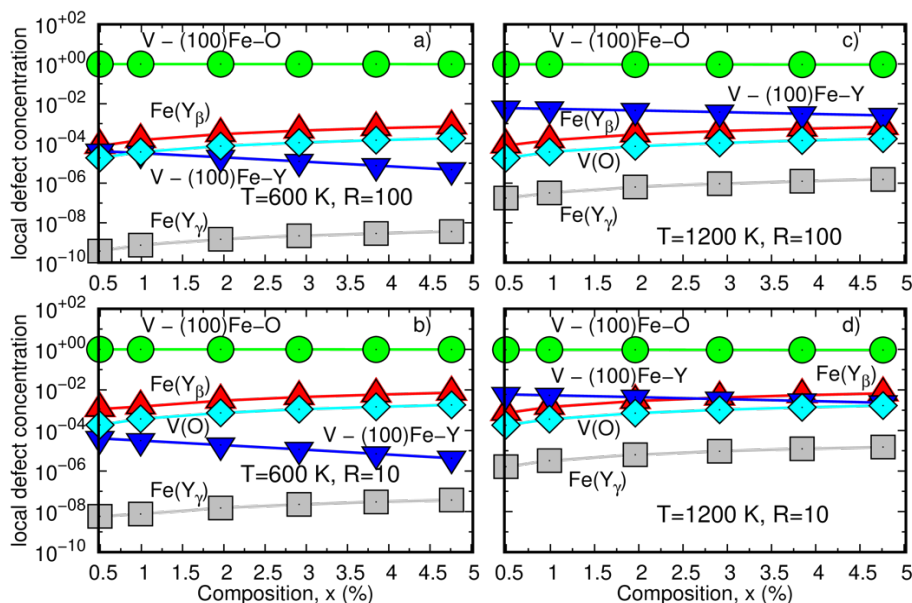
Figure 66. Local defect concentration in $(Y_{2/5}O_{3/5})_x(bcc\ Fe)_{1-x}$ as a function of composition x for a set of ODS particle sizes and temperatures: a) particle radius R=100 (in bcc Fe lattice parameters) and T=600 K, b) R=10 and T=600 K, c) R=100 and T=1200 K, d) R=10 and T=1200 K. Half of the ODS-matrix interfaces correspond to Klim interface and half to (100). Local concentration of Fe vacancies in the first layer of (100)Fe-OY interface are shown by green circles, (100)Fe-YO one by blue down triangles, Fe atom substituting Y in β sites of Y2O3 – red up triangles, vacancies in O sites of Y2O3 – cyan diamonds and Fe atom substituting Y in γ sites of Y2O3 – grey squares.

These defect formation energies have been calculated and published in our previous work [1], while formation energies and interactions of vacancies at the interface were taken from publication by Brodrick et al. [2] The result obtained for [100] interface vacancy concentrations do not look surprising if the large misfit, 4% [2], is taken into consideration. Such overextended interfaces traditionally play a role as sinks for the vacancies. This nonphysical misfit is usually compensated by introduction of extra atomic planes (creating dislocations) from the size of the matrix or precipitate. However, this question is outside of the scope of current research and it is assumed that the precipitate – matrix interface is Klim type. This model leads to result having much more realistic physical sense. The results for defect distributions in this system are presented in ***Figure 67***.

As can be seen many defects correspond to Fe atoms substituting for Y in β sites and vacancies in oxygen sites of Y_2O_3. The concentration of Fe interstitials in Y γ sites is four orders of magnitude lower than in β sites. Concentrations of Fe substitution and oxygen vacancies are approximately equal. This relation directly follows from the second constraint of minimization of the thermodynamic potential, $\frac{N_Y}{N_O} = \frac{2}{3}$. An interesting finding that should be mentioned is the unexpectedly high concentration of Fe substitutions for

yttrium atoms. This result is partially conformed by experimental observation [3]. Also, in full agreement with 2/3 relation is the observed large f oxygen concentration. Thus, for composition, x, close to 5 % and radius of precipitates R=10 lattice parameters, this concentration is larger than 10^{-4} at 600 K (***Figure 67*a**) while at 1200 K (***Figure 67*d**) it reaches 10^{-3}. However, neither the large concentration of vacancies at interface, nor Fe vacancies nor Fe vacancy oxygen clusters (V+O) have been found. There are two reasons behind these results. The first is that we describe the system as close to the equilibrium state. Second, is that in previous theoretical works the authors used a nonphysical chemical potential for the oxygen atom in estimating the formation energy of V+O clusters. This new proposed approach provides a way to a unique definition of this value.
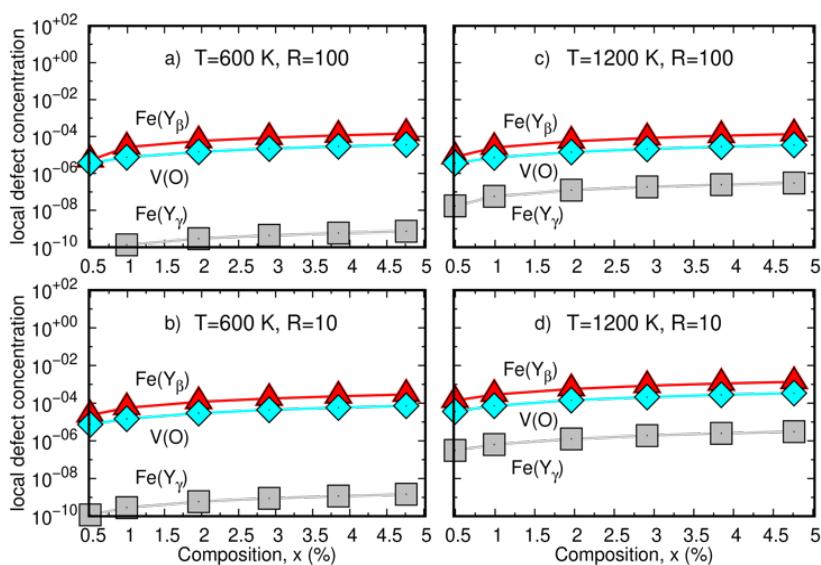
Figure 67. Local defect concentration in $(Y_{2/5}O_{3/5})_x(bcc\ Fe)_{1-x}$ as a function of composition x for a set of ODS particle sizes and temperatures: a) particle radius R=100 (in bcc Fe lattice parameters) and T=600 K, b) R=10 and T=600 K, c) R=100 and T=1200 K, d) R=10 and T=1200 K. The ODS-matrix are joined by Klim interfaces only. Local concentration of Fe atom substituting Y in β sites of Y_2O_3 – red up triangles, vacancies in O sites of Y_2O_3 – cyan diamonds and Fe atom substituting Y in γ sites of Y_2O_3 – grey squares.

FUTURE PLANS

Future work will extend the approach to the case of systems in a quasi-equilibrium state. To treat the case of alloys with large concentrations of vacancies introduced by mechanical alloying.

REFERENCES
[1.] G.D. Samolyuk, and Y.N. Osetsky, "Thermodynamic approach to the stability of multi-phase systems: application to the Y_2O_3–Fe system." *Journal of Physics: Condensed Matter*, 2015. 27(30): p. 305001.],

[2.] J. Brodrick, D.J. Hepburn, and G.J. Ackland, "Mechanism for radiation damage resistance in yttrium oxide dispersion strengthened steels." *Journal of Nuclear Materials*, 2014. 445(1): p. 291-297.

[3.] C. Parish, invited presentation, ICFRM 19, unpublished.

10. INTERNATIONAL COLLABORATIONS

10.1 US-JAPAN (QST) COLLABORATIONS ON STRUCTURAL MATERIALS

J.W. Geringer (*geringerjw@ornl.gov*), X. Cheng, A. Bhattacharya, Y. Katoh (ORNL), T. Nozawa, M. Ando, T. Kato, H. Tanigawa (QST, Japan)

OBJECTIVE

This long-standing collaboration between the U.S. DOE and the National Institutes for Quantum and Radiological Science and Technology (QST), Japan jointly pursues activities using the advanced capabilities for materials irradiation and post-irradiated examination at ORNL, especially the HFIR, the hot cells, and LAMDA. The focus is on ferritic steels and other advanced materials, especially the development of the materials database for the design of facilities beyond ITER. The goals include achieving DEMO-relevant performance data on structural materials neutron irradiated in HFIR to high levels of displacement damage.

SUMMARY

The DOE-QST collaboration continues to steadily build the materials data bases for the RAFM alloys that include F82H, ODS and Eurofer97 steels and other materials such as nuclear grade SiC composites and copper alloys. This database is being used by QST to predict changes in mechanical performance of components of a DEMO fusion reactor.

PROGRESS AND STATUS

During FY 2019 evaluation continued on a series of irradiated RAFM steel specimens designed to evaluate the effects of He on the damage mechanisms in the high dose regime (up to 80 dpa). Microstructural examination is used to not only elucidate the mechanical response at varying He accumulations in the same dose-temperature regime but also to correlate this response to the development of the microstructure including bubble formation and coarsening mechanisms in the alloy. Additional post-irradiation examination includes the disassembly, measurements, investigation and analysis of the creep demonstration (FH-) rabbit series reported in Section 2.9 and the preparation and preliminary hardness testing of the bend bar specimens from HFIR capsules JP28/29 to be tested early in FY 2020.

Irradiation temperature evaluation for the nominal 300°C specimen holders of HFIR capsule RB-19J 300C is continuing, with preliminary results reported during FY 2019.

The HFIR was shut down for most of FY 2019. Irradiation experiments that will continue in FY 2020 include the F13-rabbit capsule series containing F82H specimens and the SCF and JCR series that includes SiC specimens. Pre-irradiation activities accomplished this year included the assembly of the FMP-series capsules containing RAFM steels, SiC and Cu alloys, with irradiation scheduled to start in FY 2020.

The ORNL hosted three QST assignees, T. Nozawa, M. Ando and T. Kato, for four short stays during FY 2019.

FUTURE PLANS

The focus of the DOE-QST collaboration will continue to be on mechanical and fracture toughness testing at temperatures above 573K on the remaining specimens from the high dose HFIR capsules JP28/29 and then continue with similar testing on lower dose specimens from the HFIR JP30/31 experiments.

10.2 US-JAPAN PHENIX AND FRONTIER PROGRAMS

J.W. Geringer (geringerjw@ornl.gov), Y. Katoh, L. Garrison, A, Sabau, B. Pint, C. Kessel

SUMMARY

The US/Japan Fusion Research Collaboration Project PHENIX on Technological Assessment of Plasma Facing Components for DEMO Reactors started in April 2013 and concluded March 2019. The goal of the project was to evaluate critical issues for plasma-facing components (PFCs) under fusion reactor divertor conditions,, including: (1) heat transfer, (2) mechanical properties, (3) neutron irradiation effects, and (4) tritium retention and permeation. The project participants were ORNL, Idaho National Laboratory (INL), Sandia National Laboratory (SNL), Georgia Institute of Technology, National Institute for Fusion Science of Japan (NIFS), and various Japanese universities. The role of ORNL was to participate in Task 1 on high heat flux testing, Task 2 on neutron irradiation effects, and to provide neutron irradiation in HFIR in support of all research tasks.

During the first half of FY 2019 PHENIX concluded some of its PIE activities, and the results were presented at several conferences including PFMC, ISFNT and ICFRM. In addition to the annual steering committee meeting held at ORNL during the first week of February 2019, Kyushu University hosted one workshop entitled "Progress of tritium retention/permeation for neutron damaged W with thermal neutron shield and future planning" during November 2018. The ORNL hosted three Japanese assignees under the personnel exchange agreement and Kyoto University hosted one US assignee (two pending US assignments were cancelled).

In April 2019, the US/Japan Fusion Research Collaboration started a new Project, FRONTIER (Fusion Research Oriented to Neutron irradiation effects and Tritium behavior at material IntERfaces), with the objective of evaluating Reaction Kinetics and Neutron Irradiation Effects at Interfaces in DEMO Divertor Systems. FRONTIER consists of four tasks; (1) evaluate irradiation effects on reaction dynamics at plasma-facing material/structural material interfaces, (2) perform tritium transport through interface and reaction dynamics in accidental conditions, (3) measure corrosion dynamics at liquid-solid interfaces under neutron irradiation for liquid divertor concepts and (4) engineering modeling. As in PHENIX the project participants include ORNL, INL, SNL, NIFS and Japanese Universities. The ORNL is leading three of the four tasks.

During the second half of FY 2019 the FRONTIER efforts focused on developing a first draft of an irradiation matrix accommodating the research goals and logistical constraints of all parties. Work also started on the fabrication of test materials and specimens. In May 2019, ORNL hosted the first workshop meeting to discuss the potential irradiation matrix and materials and fabrication techniques that will be used in the FRONTIER research. The ORNL also hosted two Japanese assignees for Tasks 1 and 3 respectively.

FUTURE PLANS

The first FRONTIER steering committee meeting will be held at ORNL in January 2020.

10.3 US-EUROFUSION PROJECT

J.W. Geringer (geringerjw@ornl.gov), A. Bhattacharya, X. Chen, Y. Katoh (ORNL), T. Graening, L.L. Snead, M. Reith (KIT)

BACKGROUND

The Karlsruhe Institute of Technology (KIT), as a EUROfusion project seeks to provide blanket, baseline, design-relevant data and basic material properties evaluation of EUROFER material variants. The ORNL is under contract to assist the Neutron Irradiation and Material Data task by preparation, irradiation and PIE of these steels to determine their suitability for use in fusion energy systems. This requires the use of several unique ORNL facilities including HFIR and the Irradiated Materials Examination and Testing (IMET) hot cell facility.

PROGRESS

In FY 2019 ORNL continued with one HFIR cycle irradiation of 14 irradiation vehicles (known as "rabbit" capsules) loaded with Eurofer-97 alloys provided by KIT and EUROfusion program collaborators. The 14 rabbits began irradiation in May 2018 with a target of 20 dpa (~12 cycles) at nominal target temperatures ranging from 220°C to 375°C.The HFIR only operated for one cycle (cycle 482), during FY19 after it experienced an unplanned shutdown event shortly after starting cycle 483. The 14 rabbits will continue in HFIR to complete 8 more cycles.

Post-irradiation examination on the Eurofer97 steel variant specimens (irradiated to 2.5 dpa in FY 2018) occurred during FY 2019. Passive thermometry analysis (to verify irradiation temperatures), hardness-, tensile- and fracture toughness testing were completed. Microstructural characterization will continue, including light optical microscopy (LOM), TEM, energy dispersive X-ray spectroscopy (EDX), and study of fracture surfaces.

Detail of the post-irradiation progress will be reported by in January 2020. It will contain the results of the Vickers hardness testing and SiC thermometry analysis.   The PIE will be summarized in a technical report as the final deliverable for this phase of the work.

Sections 2.5, 13.3 and 13.4 summarize limited details related to this project.

10.4   IAEA - STANDARDIZATION OF SMALL SPECIMEN TEST TECHNIQUES FOR FUSION APPLICATIONS

X. Chen (chenx2@ornl.gov), M. A. Sokolov

OBJECTIVE

The International Atomic Energy Agency (IAEA) Coordinated Research Project (CRP) for the standardization of small specimen test techniques (SSTT) for fusion applications aims to harmonize and coordinate worldwide development and acceptance of SSTT for fusion applications. The ORNL participation in this project will contribute in three topic areas: tensile, fracture toughness, and fatigue crack growth rate testing.

SUMMARY

The IAEA CRP for the standardization of SSTT for fusion applications aims to address the following main tasks:
• Analysis of SSTT results focusing on fusion reference structural materials (RAFM steels).
• Topic areas: tensile, creep, low cycle fatigue, fracture toughness, and fatigue crack growth rate testing.
• Definition of a strategy for meaningful Round Robin tests for establishing best practices of SSTT.
• Establishment of guidelines for common practice in the use of SSTT.

The ORNL participation in this project will focus on rationalizing the specimen size effects on properties of RAFM steels measured in tensile, fracture toughness, and fatigue crack growth rate tests. Recommendations will be made on the limitation of specimen downsizing as well as on best practices for using SSTT for fusion applications. As of the end of FY 2019, the test matrices have been finalized among the participants of the CRP and materials are being distributed to participants for specimen machining and testing. It is anticipated that initial testing will be completed by the end of CY 2020.

PROGRESS AND STATUS

The 2nd Research Coordination Meeting for this project was held in January 2019 at the IAEA headquarter in Vienna Austria. Personnel from eight institutions, including ORNL (USA), National Institutes for Quantum and Radiological Science and Technology (Japan), KIT (Germany), CIEMAT (Spain), Shanghai Jiao Tong University (China), National Institute for Fusion Science (Japan), Tohoku University (Japan), and Osaka University (Japan), attended this meeting. ORNL presented results of the literature review on SSTT for three topic areas, i.e. tensile, fracture toughness, and fatigue crack growth rate testing. At the same meeting, the test materials, methodology, specimen geometry, and responsibilities of participants for each topic area were finalized. Three candidate RAFM steels, i.e. F82H, Eurofer97, and CLF, were selected for the CRP. The ORNL will take a leading role in applying the Master Curve method in the ASTM E1921 standard for fracture toughness characterization of RAFM steels. The geometries of fracture toughness specimens to be tested by ORNL include 18x3.3x1.65 mm miniature bend bar specimens, 4 mm thickness mini-CT specimens, and standard 0.5T-CT specimens. A satellite meeting for the project was held in September 2019 in conjunction with the 14th International Symposium on Fusion Nuclear Technology in Budapest Hungary. A brief update was given by task leads of each topic area. During that meeting, the United Kingdom Atomic Energy Authority became a new participating institution for this project.

FUTURE PLANS

A draft guideline for fracture toughness testing using the Master Curve method in the ASTM E1921 standard will be completed in late CY 2019. After that specimen machining will be started. It is anticipated that initial testing will be completed by the end CY 2020.

11. MATERIALS ENGINEERING

11.1 MATERIALS ENGINEERING SUPPORT FOR THE FNSF CONCEPTUAL DESIGN

Arthur F. Rowcliffe (art.rowcliffe@gmail.com)

OBJECTIVE

This task is directed at identifying potential solutions to the definition of structural materials for the FNSF power core components, and the materials for lifetime components such as the vacuum vessel, structural ring and neutron shields. A parallel activity is maintaining the interface between the fusion materials program and the design studies for the next-step FESS activities.

PROGRESS AND STATUS

A range of materials-related issues which have not been considered previously have been identified during the FNSF next step design studies. The most important of these are:

- First Wall solutions including graded W layers;
- transitions from ODS structures in high performance blanket sections to RAFM sections;
- assessment of the impact of recent irradiation data and correlations on system performance;
- solid breeder interactions with RAFMs and Al-bearing alloys;
- structural materials compatibility with high temperature He;
- manufacturing/assembly issues, including modular versus single component blanket designs;
- requirements for reduced activation materials for bolting, fasteners etc. for modular components;
- initial selection of heat exchanger materials.

Additional materials issues under discussion include the following:

- The space between the face sheets of the vacuum vessel and structural ring is utilized for cooling channels and for the shielding filler material which is a RAFM containing 3 w% boron. Shielding performance assumes that the alloy is homogeneous with B atoms simply replacing Fe atoms. However, the very low solubility of B in Fe ensures that, with conventional processing, B will be distributed in an inhomogeneous distribution of coarse boride particles. Advanced processing technologies will be needed to develop nano-scale homogeneous dispersions of boride particles to ensure maximum shielding efficiency.
- Direct exposure to the plasma presents a major challenge in developing materials solutions for RF antenna and launchers. Conceptual designs utilize a He-cooled RAFM structure with a surface coating 10-50 µm of high conductivity copper, on a 30 µm barrier layer of ZrC. Potential issues include void swelling and helium-induced blistering of the copper, possible de-bonding of coatings from the RAFM, and transfer of atoms from the structural material to the Cu resulting in reduced thermal conductivity. Near term needs include reliability assessments of RAFM/ZrC/Cu produced by current coating technologies and fission reactor testing using doping techniques to simulate helium generation. Reliable solutions will probably require adoption of Advanced Manufacturing approaches to RF launcher design and development of high-performance materials solutions.

- The currently assumed upper operating temperature limit (1200-1300°C) for hot-rolled W is based on relatively short-term annealing studies. This recrystallization limit needs to be reassessed to account for long-time, high temperature exposure and radiation effects. Recovery and recrystallization kinetics vary with the processing-induced microstructure and deformation level, solute concentrations, interstitial impurities and the distribution of precipitate phases and dispersoids. Manipulation of these parameters could provide pathways to the development of W-based materials with improved resistance to in-service recrystallization.

12. EXPERIMENTAL TECHNIQUES AND LABORATORY SYSTEMS

12.1 MECHANICAL TEST SYSTEMS FOR IMET HOT CELLS

X. Chen (chenx2@ornl.gov), C. Stevens, K. Smith, Hideo Sakasegawa (QST)

OBJECTIVE

This task is directed at installing a high temperature vacuum tensile test system in the IMET hot cell to provide cutting-edge mechanical testing capability to the Fusion Materials Science Program.

SUMMARY

The installation of a high temperature vacuum tensile test system was completed in March 2019. The tensile frame is stationed in Cell #1 of the IMET at ORNL. The system is capable of both room temperature and elevated temperature mechanical testing in vacuum with a non-contact video extensometer for strain measurement. At the end of FY 2019, we have successfully used the frame for tensile testing in support of the EUROFusion project and the collaboration with the National Institutes for Quantum and Radiological Science and Technology (QST).

PROGRESS AND STATUS

The detailed description of the high temperature vacuum tensile test system can be found in [1] and is briefly described here. ***Figure 68*** shows an overview of the frame in the hot cell. The entire test system consists of these four major parts:

1.   Instron® 5967 electromechanical universal testing system.
2.   Oxy-Gon® FR210 customized tensile test vacuum furnace system.
3.   Pfeiffer® ACP 40 dry roughing pump and TPH 2301 turbomolecular pumps.
4.   ThermoFish Scientific® ThermoFlex15000 air cooled recirculating chiller.

The tensile frame has a loading capacity of 30 kN with a 5 kN load cell currently installed. The frame crosshead speed covers the range of 0.001 to 1000 mm/min. Both tensile and compression tests can be performed using the frame. The ultimate vacuum level achievable for this frame is approximately 7-8 x 10^{-7} torr at 800°C. The heating system utilizes tungsten mesh heating elements with the maximum temperature rated at 1200°C. The usable working zone within the vacuum furnace has dimensions of 7.6 cm diameter x 10 cm height. The system also allows three type N thermocouple measurements with one used for temperature control and one type C thermocouple probe for overtemperature protection.

Currently, an SS-J3 tensile fixture has been installed in the tensile frame. The temperature gradient across the specimen gauge is fully captured by measurements from two thermocouples. The specimen retaining pin design minimizes potential loss of broken tensile specimen halves after testing. In the initial room temperature testing of ten Eurofer97 tensile specimens, both the fixture design and tensile frame exhibited outstanding performance.
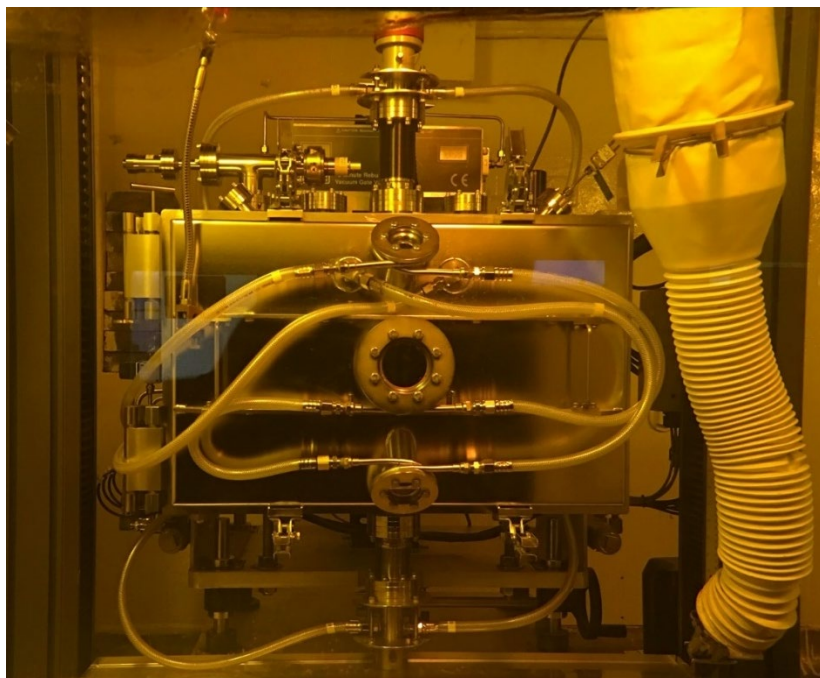
Figure 68. Overview of the high temperature vacuum tensile system installed in the ORNL IMET hot cell.

To facilitate non-contact strain measurements, the ORNL team collaborated with the QST team in designing a non-contact video extensometer system with the QST team leading the camera, lens, light source, and image acquisition system and ORNL team leading the fixture design and system installation. The system is capable of global strain measurements with potential for digital image correlation related measurements. The system is also designed for both room temperature and elevated temperature measurements. The major components for this system consist of:

1.   Keyence CA-H2100M camera.
2.   VS Technology telecentric lens VS-TC1-300CO.
3.   165-SHU UV curing ultra-high-pressure mercury vapor lamp light source.
4.   CV-H1XA Simulation-Software.
5.   Newport DS65-XYZ linear stage.
6.   Dovetail with a stopper design.
7.   Quick-release locking knob.

The non-contact video extensometer system has been used during the out-of-cell verification stage and indicated satisfactory performance.

FUTURE PLANS

For FY 2020, we plan to evaluate another SS-J3 tensile fixture designed by QST and use the non-contact video extensometer system for testing irradiated specimens.

REFERENCES
[1.]   X. Chen, C. Stevens, K. Smith, J.W. Geringer, Y. Katoh, H. Sakasegawa, "High Temperature Vacuum Tensile Frame Equipped with Non-Contact Video Extensometer," *Fusion Materials Semiannual Progress Report*, DOE-ER-0313/66, pp. 189-194.

12.2 TENSILE TESTING STEEL AND TUNGSTEN FIBERS FOR APPLICATIONS IN COMPOSITE MATERIALS

L. M. Garrison (garrisonlm@ornl.gov), M. Gussev (ORNL), M. Weinstein (University of Wisconsin-Madison), C. Lin (University of Illinois)

OBJECTIVE

The goal of this project is to develop a technique for tensile testing steel and tungsten fibers to determine the mechanical properties of the fibers for use in fiber-strengthened composites.

SUMMARY

A new fixture was designed for tensile testing fibers. To cushion the sample in the fixture, each fiber must be precisely glued into a paper frame. Initial tests have been completed on type 304 stainless steel and tungsten fibers. Digital image correlation is used to monitor fiber extension during the tests. Tungsten fibers have localized deformation before fracture, while steel fibers show significant plastic deformation over the full length of the fiber before necking and failure.

PROGRESS AND STATUS

Tungsten fibers (150 µm diameter) can be used for tungsten fiber composites because they are strong and relatively ductile. These beneficial properties also make them difficult to test because they require a strong grip to test without sliding of the fibers. While tungsten fibers are strong, they are susceptible to scratches or stress concentration from the gripping fixture. Steel alloy 304 fibers with diameter 203 µm were selected as initial test material for the fiber gripping method. They are also a useful test of the method because they have significantly different mechanical properties than the tungsten fibers. The fibers, either tungsten or steel, are prepared for testing by mounting on a paper frame using UHU 300 plus epoxy (***Figure 69***). The epoxy and the paper frame serve two purposes: allow easier handling of the fiber without direct contact with the gauge section or risk of bending the fiber and cushioning of the fibers when they are clamped into the fixture. The fibers have 1 cm exposed gauge section in the center of the paper frame.
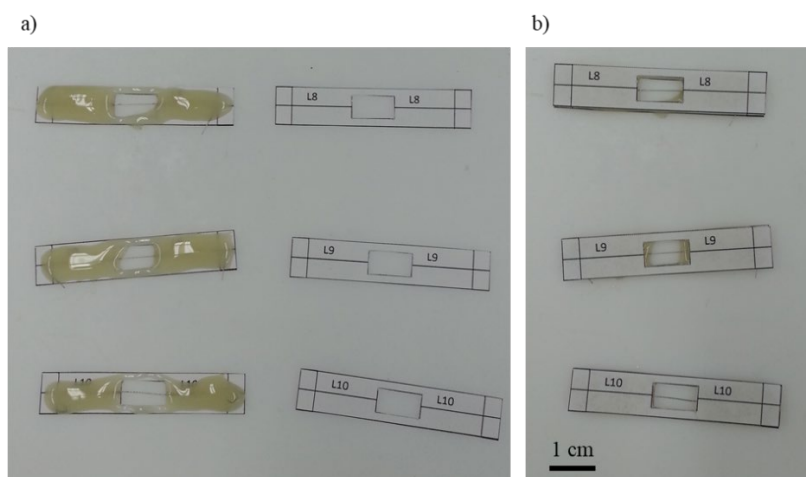
Figure 69. (a) Epoxy is placed on one half of the paper frame and the fiber gently placed into the center. (b) the other half of the paper frame is placed on top and helps flatten and spread the epoxy into an even layer.

A fixture was designed to clamp and hold the fiber in place for tensile testing (***Figure 70***). Braces on the side of the fixture keep the two halves of the fixture at a fixed distance and prevent any undue stress or bending on the fiber during loading. Once the fixture is installed in the tensile frame, the side braces are removed, and the sides of the paper frame are cut so that only the fiber remains connecting the two halves of the fixture (***Figure 71***).
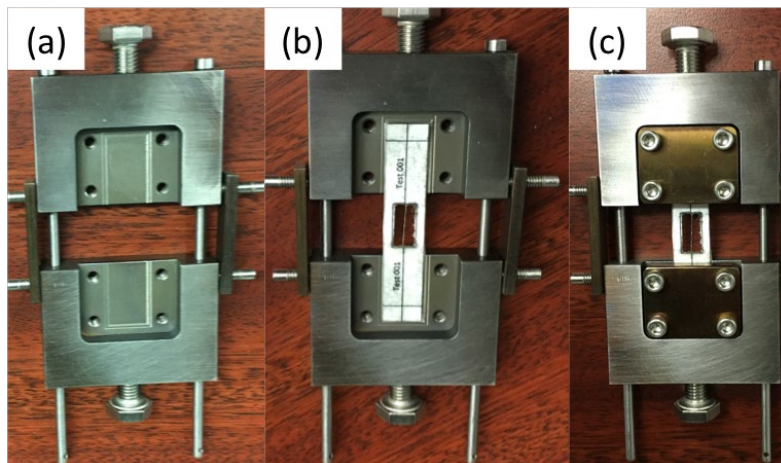
Figure 70. Tensile fixture (a) without sample (b) with sample (c) with sample clamped in place.

Figure 71. Fiber fixture installed in the tensile frame with the camera for digital image correlation immediately in front of the sample.

Digital image correlation (DIC) was used with the fiber tests to provide accurate strain data. The fiber was spray painted with white paint and a black speckle coating (***Figure 72***). Computer software is used to track the change in position of individual dots in the paint pattern and correlates that to strain of the fiber. Tungsten and steel fibers have been successfully tested and the DIC data is being analyzed. SEM images of the fibers after tests show more significant necking of the steel fibers than of the tungsten (***Figure 73***).
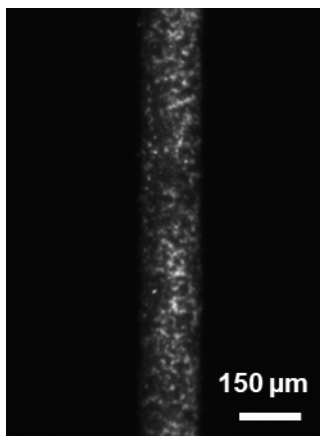
Figure 72. A tungsten fiber painted with the speckle pattern for DIC strain measurement.
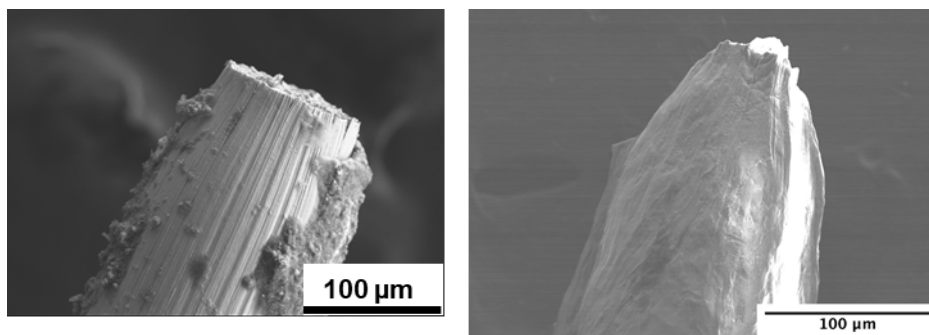
Figure 73. Left-Fracture end of tungsten fiber (surface debris is paint from DIC). Right-Fracture end of Alloy 304 sample.

<div align="center">

13. HFIR IRRADIATION PROGRAM

</div>

13.1 FUSION 2019 IRRADIATION CAPSULE DESIGN

R. Howard (howardrh@ornl.gov), N. Russell

OBJECTIVE

The Fusion 2019 Irradiation program plan was to irradiate 20 or more capsules with design temperatures from as low as 100°C up to 650°C. Specimen loading will include several materials and specimen types to meet objectives of the Fusion Materials program.

SUMMARY

The Fusion 2019 Irradiation program has broad requirements for a larger number of capsules and several different specimen materials. As such, a general capsule design for metal specimens was needed to easily adapt to different irradiation conditions, identify irradiation locations in HFIR and support such a challenging effort. The ORNL irradiation engineering team have developed two generic irradiation capsule designs, called the GENTEN for tensile specimens and GENBEN to accommodate bend bar specimens. These formats will facilitate rapid design of capsules for a wide range of temperatures, specimen composition, and irradiation location in HFIR.

PROGRESS AND STATUS

The GENTEN and GENBEN irradiation capsule formats described last year are being implemented for design of irradiation experiments for HFIR. The GENTEN or general tensile design has undergone a safety analysis and has been approved for use in HFIR. The GENTEN design has been applied to eight high temperature Fusion Augmentation irradiation capsules (FMP10-17) that will be described in more detail below. These GENTEN capsules are scheduled for irradiation cycle 484 in HFIR. The GENBEN or general bend bar design has undergone the same safety analysis as the GENTEN but is still in final approval stages by the HFIR safety team.

13.2   THE FUSION AUGMENTATION HFIR IRRADIATION CAMPAIGN

N. Russell (russellng@ornl.gov)

OBJECTIVE

The Fusion 2019 Irradiation program plans includes 20 capsules for the Fusion Augmentation Campaign, including a wide range of specimen materials. These specimen materials include copper alloys, steels, and silicon carbide. The Fusion Augmentation irradiation capsules are designed to achieve temperatures ranging from 100 to 650°C.

SUMMARY

This HFIR irradiation campaign required 20 capsules (9 at low temperature and 8 at high temperatures with both SSJ tensile specimens and MPC2 coupon specimens, 2 low temperature with M4PCCVN multi-notch bend bar toughness specimens, and 1 with cerium oxide and tungsten on SiC disk specimens.) The low temperature designs achieve temperatures in the range of 100°C to 350°C, while the high temperature capsules are designed for temperatures that range from 385 to 650°C. Each set of irradiation capsules has some to reach low exposure doses (5-7 dpa) and some for higher doses (20-80 dpa). Images of representative SSJ/MPC2 specimen format and toughness specimen capsules are shown in ***Figure 74***.
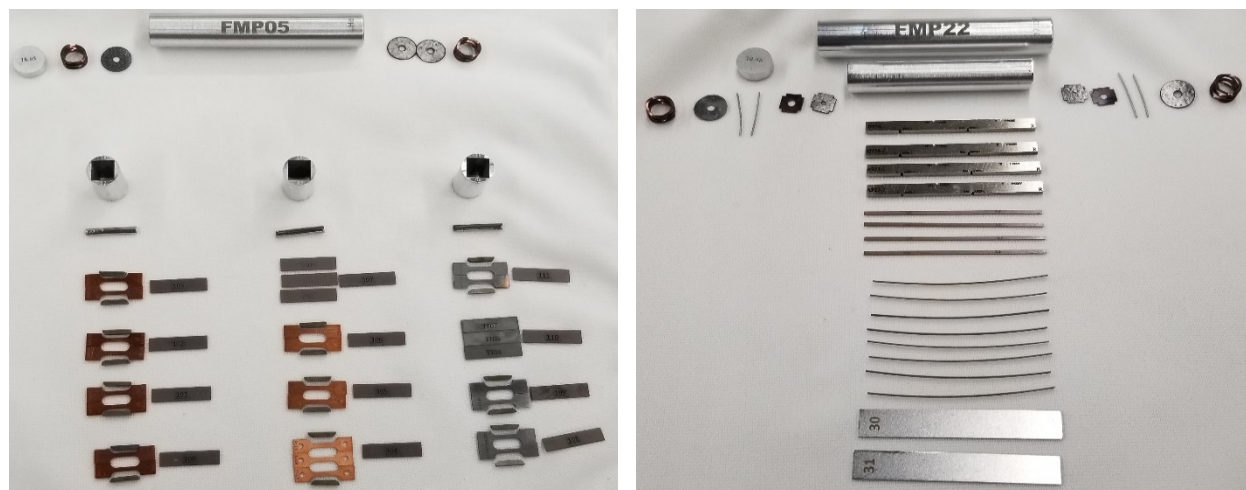
Figure 74. Representative layout of Fusion Augmentation capsule FMP05 including SSJ/MPC2 tensile and coupon specimens (left) and capsule FMP22 holding M4PCCVN multi-notch bend bar toughness specimens (right). These capsules will be assembled, sealed, inspected, then irradiated in HFIR.

PROGRESS AND STATUS

Eight of the initial nine low temperature capsules (FMP02-09) were submitted to HFIR for irradiation in July 2019 (cycle 484). The one capsule that was not included (FMP01) required a design modification to the assembly to accommodate the 100°C requirement. This capsule has since been built and is in the final review process with delivery to HFIR in October 2019 for the following HFIR cycle (cycle 485). The eight-high temperature (FMP10-17) and two bend bar toughness specimen capsules (FMP22, 23) were submitted to HFIR for irradiation in September 2019 (cycle 484). The cerium oxide and tungsten on disk specimen capsule (FMP19) has had parts delivered and inspected. This irradiation capsule is expected to be ready for submission to HFIR for cycle 485.

13.3   THE EUROFER HFIR IRRADIATION CAMPAIGN

R. Howard (howardrh@ornl.gov), N. Russell

OBJECTIVE

This work focused on establishing an irradiation capsule design set appropriate for both SSJ tensile specimens and M4PCVVN bend bar toughness specimens at temperatures ranging between 200°C and 380°C. This work was specifically directed to support the Eurofer 97 irradiations under contract with the Karlsruhe Institute of Technology (KIT), acting as agents for the EUROfusion program.

SUMMARY

This irradiation campaign required 21 HFIR irradiation capsules (7 low dose capsules to compare alloy variations of Eurofer 97and 14 high dose capsules containing reference Eurofer97). These capsules were designed to be irradiated at various temperatures between 200°C and 380°C and were planned for near centerline HFIR flux trap positions.

PROGRESS AND STATUS

The 14 high dose capsules are scheduled to receive nominally 20 dpa over 12 HFIR cycles. These capsules were submitted to HFIR for cycle 480. During the HFIR shutdown, part way through cycle 483, half of these capsules were removed to make room for some low dose Fusion Augmentation irradiation capsules. In the coming next few cycles, these Fusion Augmentation irradiation capsules will be removed and the remaining Eurofer irradiation capsules can be replaced to complete their scheduled irradiation exposures.

13.4   A HYDROGEN-CHARGED IRRADIATION CAPSULE FOR HFIR

N.O. Cetiner (cetinerno@ornl.gov), N. Russell

OBJECTIVE

The objective of this work is the design of a first-of a kind capsule for HFIR that allows neutron irradiation of plasma facing component (PFC) materials in a hydrogen environment. A first use will develop data on the modification of microstructures and physicochemical properties of tungsten metal irradiated in hydrogen.

SUMMARY

Most studies of hydrogen migration in irradiated metals have used a sequential approach of exposing specimens to hydrogen, then irradiating the hydrogen-charged specimens. However, the presence of hydrogen in a metal affects vacancy migration during irradiation and modifies the resulting microstructures, implying that a sequential ion irradiation approach is less desirable than a simultaneous irradiation scheme. To confirm this effect, it is necessary to irradiate tungsten metal specimens in a hydrogen environment. However, filling and seal welding a capsule in hydrogen is difficult due to the extreme flammability of hydrogen in air. Filling a weld chamber with hydrogen and then performing an arc weld in that environment presents safety concerns that, while ultimately manageable, requires a high degree of planning, as well as the development and construction of additional engineering safeguards, and all at a high cost.

A novel irradiation experiment was designed to allow the safe irradiation of tungsten, graphite, or other PFC material specimens in a hydrogen environment. The design uses vanadium disks charged with hydrogen. The hydrogen in solution in the metal matrix is stable at room temperature, so the capsule can be hermetically sealed by welding without significant release of hydrogen. The hydrogen is released into the sealed capsule volume as the V-H specimens in the capsule reach irradiation temperature in the HFIR reactor. At the 400°C design temperature, the hydrogen mole fraction is about 40%. This experiment, to be conducted in HFIR, is designed to expose tungsten, SiC, and graphite disks to hydrogen during neutron irradiation in the sealed rabbit capsule.

PROGRESS AND STATUS

Four irradiation capsules for this program were built in 2018. These capsules are awaiting safety reviews to be fully approved by HFIR so that they can be submitted for irradiation. It is expected that reviews will be completed so that these capsules can be submitted to HFIR for irradiation starting in cycle 485.

13.5 HFIR IRRADIATION EXPERIMENTS

Y. Katoh (katohy@ornl.gov), N.G. Russell, J.L. McDuffee, C. Bryan, J.P. Robertson

SUMMARY

Neutron irradiation experiments were performed in support of the research and development of fusion reactor materials using various materials irradiation facilities in the HFIR.

The reactor was shut down and placed in a safe condition on November 13, 2018, in response to elevated radiation readings within the primary system that cools the core. Examination revealed several of the fuel plates that make up the fuel element had deflected away from their normal position. The ORNL has completed a corrective action plan to improve alignment between design and fuel element manufacturing and to put in place new and more rigorous approaches to fuel element inspection. The reactor is expected to re-start in November 2019, with Cycle Number 484.

The HFIR operated for 6.5 MWD on Cycle 483 before the shutdown, as shown in *Table 11*.

Table 11. Summary of HFIR operation during FY 2019

	HFIR Cycle Number
	483
Cycle start date	11/13/2018
Cycle end date	11/13/2018
MWD this cycle	6.52

Rabbit capsule F13A5 has been removed from the reactor and shipped to the hot cells for disassembly. This capsule containing FeCrAlY steel specimens in the form of bend bars was irradiated at 300°C to 29 dpa.

At the end of FY 2019, 39 target zone rabbit capsules are awaiting continuing irradiation in HFIR toward their target neutron fluences. These capsules are listed in *Table 12* along with the information on materials, specimen types, and irradiation parameters.

Table 12. HFIR fusion materials program rabbit capsules continuing irradiation beyond FY 2019

Experiment Designation	Primary Materials	Specimen Types	Irradiation Temperature (°C)	Max Exposure (dpa)	Number of Reactor Cycles	HFIR Cycles Start – End		
F13B4	FeCrAlY Steel	Tensile	300	50	29	451	-	496
JCR11-05	SiC/SiC	bend bars	950	200	115	444	-	567
JCR11-07	SiC/SiC	Mini bend bars	950	100	47	444	-	491
JCR11-08	SiC/SiC	Mini bend bars	950	200	115	444	-	559
SCF8	SiC/SiC	Miniature flexure bar	600	100	45	457	-	501
SCF9	SiC/SiC	Miniature flexure bar	600	200	90	457	-	547
SCF11	SiC/SiC	Miniature flexure bar	950	100	57	458	-	516
ES01 to ES07 7 tensile capsules	EUROFER 97	Tensile/MPC	220 to 375	20	12	479	-	490
ES11 to ES17 7 bend bar capsules	EUROFER 97	Bend bars	220 to 375	20	12	479	-	490
FMP02 to FMP09	various	Tensile/MPC	200 to 350	range	-	484 ?		
FMP10 to FMP17	various	Tensile/MPC	385 to 650	range	-	484 ?		
FMP22	F82H	Bend Bars	300	20	11	484?		
FMP23	F82H	Bend Bars	300	80	45	484?		

*MPC is a Multi-Purpose Coupon, with the same outer dimensions as a tensile specimen.

14. PUBLICATION AND PRESENTATION RECORD

14.1 PAPERS PUBLISHED IN FY 2019

(Alphabetical by first ORNL author)

A. Bhattacharya, C.M. Parish, T. Koyanagi, C.M. Petrie, D. King, G. Hilmas, W.G. Fahrenholtz, S. J. Zinkle, Y. Katoh, "Nano-scale microstructure damage by neutron irradiations in a novel Boron-11 enriched TiB2 ultra-high temperature ceramic," *Acta Materialia* 165 (2019) 26-39

A. Bhattacharya, C.M. Parish, J. Henry, Y. Katoh, "High throughput crystal structure and composition mapping of crystalline nanoprecipates in alloys by transmission Kikuchi diffraction and analytical electron microscopy," *Ultramicroscopy* 202 (2019) 33-43

A. Bhattacharya, E. Meslin, J. Henry, B. Decamps, F. Lepretre, A. Barbu, "Combined effect of injected interstitials and He implantation, and cavities inside dislocation loops in high purity Fe-Cr alloys," *J. Nucl. Mater.* 519 (2019) 30-44

S. Agarwal, A. Bhattacharya, P. Trocellier, S.J. Zinkle, "Helium induced microstructure damage, nano-scale grain formation and helium retention behaviour of ZrC," *Acta Materialia* 163 (2019) 16-27

Xiang Chen, Arunodaya Bhattacharya, Mikhail A. Sokolov, Logan N. Clowers, Yukinori Yamamoto, TimGraening, Kory D. Linton, Yutai Katoh, Michael Rieth, "Mechanical properties and microstructure characterization of Eurofer97 steel variants in EUROfusion program," *Fusion Eng. & Design* 146 (2019) 2227-2232, https://doi.org/10.1016/j.fusengdes.2019.03.158

K.G. Field, J.L. McDuffee, J.W. Geringer, C.M. Petrie, Y. Katoh, "Evaluation of the Continous Dilatometer Method of Silicon Carbide Thermometry for Passive Irradiation Temperature Determination," *Nuclear Instruments and Methods in Physics Research Section B: Beam Interactions with Materials and Atoms*, 445 (2019) 46-56

Lauren M. Garrison, Y. Katoh, N.A.P. Kiran Kumar, "Mechanical Properties of Single-Crystal Tungsten Irradiated in a Mixed Spectrum Fission Reactor," *Journal of Nuclear Materials* 518 (2019) 208-225

Lauren Garrison, Yutai Katoh, Josina Geringer, Masafumi Akiyoshi, Xiang Chen, Maoto Fukuda, Akira Hasegawa, Tatsuya Hinoki, Xunxiang Hu, Takaaki Koyanagi, Eric Lang, Michael Mcallister, Joel McDuffee, Takeshi Miyazawa, Chad Parish, Emily Proehl, Nathan Reid, " PHENIX US-Japan Collaboration Investigation of Thermal and Mechanical Properties of Thermal Neutron-Shielded Irradiated Tungsten," Fusion Science and Technology 75 (2019) 510-519

M. Akiyoshi, R. Kasada, Y. Ishibashi, L.M. Garrison, J.W. Geringer, W.D. Porter, Y. Katoh, "Validation of miniature test specimens for post-irradiation thermal diffusivity measurement," *Fusion Engineering and Design* 136 (2018) 513–517. doi:10.1016/j.fusengdes.2018.03.008

Eric Lang, Nathan Reid, Lauren Garrison, Chad Parish, Jean Paul Allain, "Elemental Characterization of Neutron-Irradiated Tungsten Using the GD-OES Technique," *Fusion Science and Technology* 75 (2019) 533-541

C.E. Kessel, J.P. Blanchard, A. Davis, L. El-Guebaly, L.M. Garrison, N.M. Ghoniem, P.W. Humrickhouse, Y. Huang, Y. Katoh, A. Khodak, E.P. Marriott, S. Malang, N.B. Morley, G.H. Neilson, J. Rapp, M.E. Rensink, T.D. Rognlien, A.F. Rowcliffe, S. Smolentsev, L.L. Snead, M.S. Tillack, P. Titus, L.M. Waganer, G.M. Wallace, S.J. Wukitch, A. Ying, K. Young, Y. Zhai, "Overview of the fusion nuclear science facility, a credible break-in step on the path to fusion energy," *Fusion Engineering and Design* 135B (2018) 236-270

Tim Gräning, Michael Rieth, Jan Hoffmann, Sascha Seils, Philip D.Edmondson, Anton Möslang, "Microstructural investigation of an extruded austenitic oxide dispersion strengthened steel containing a carbon-containing process control agent," *Journal of Nuclear Materials* 516 (2019) 335-346

Tim Gräning, Michael Klimenkov, Michael Rieth, Cornelia Heintze, Anton Möslang, "Long-term stability of the microstructure of austenitic ODS steel rods produced with a carbon-containing process control agent," *Journal of Nuclear Materials* 523 (2019) 111-120

Xunxiang Hu, Chad M. Parish, Kun Wang, Takaaki Koyanagi, Benjamin P. Eftink, Yutai Katoh, "Transmutation-induced precipitation in tungsten irradiated with a mixed energy neutron spectrum," *Acta Materialia* 165 (2019) 51-61

Xunxiang Hu, Lizhen Tan, Kun Wang, Caleb P. Mssey, David T. Hoelzer, Yutai Katoh, "Deuterium retention in advanced steels for fusion reactor structural application," *Journal of Nuclear Materials* 516 (2019) 144-151

Katherine Haynes, Xunxiang Hu, Brian Wirth, Christopher Hatem, and Kevin Jones, "Defect Evolution in Ultralow Energy, High Dose Helium Implants of Silicon Performed at Elevated Temperatures," *Journal of Applied Physics* 124 (2018) paper 165708

Y. Katoh, L.L. Snead, L.M. Garrison, X. Hu, T. Koyanagi, C.M. Parish, P.D. Edmondson, M. Fukuda, T. Tanaka, A. Hasegawa, "Response of unalloyed tungsten to mixed spectrum neutrons," *Journal of Nuclear Materials* 520 (2019) 193-207

L.L. Snead, Y. Katoh, T. Koyanagi, K. Terrani, "Stored energy release in neutron irradiated silicon carbide," *Journal of Nuclear Materials* 514 (2019) 181–188. doi:10.1016/j.jnucmat.2018.12.005

S. Agarwal, G. Duscher, Y. Zhao, M.L. Crespillo, Y. Katoh, W.J. Weber, "Multiscale characterization of irradiation behaviour of ion-irradiated SiC/SiC composites," *Acta Materialia* 161 (2018) 207–220 doi:10.1016/j.actamat.2018.09.012

Takaaki Koyanagi, Yutai Katoh, Caen Ang, Derek King, Greg E. Hilmas, William G. Fahrenholtz, "Response of isotopically tailored titanium diboride to neutron irradiation," *Journal of American Ceramics Society*, 102 (2019) 85-89

T. Koyanagi, Y. Katoh, M.J. Lance, "Raman spectroscopy of neutron irradiated silicon carbide: correlation among Raman spectra, swelling and irradiation temperature," *Journal of Raman Spectroscopy* 49 (2018) 1686-1692

T. Koyanagi, Y. Katoh, T. Nozawa, L.L. Snead, S. Kondo, C.H. Henager Jr., M. Ferraris, T. Hinoki, Q. Huang, "Recent progress in the development of SiC composites for nuclear fusion applications," *Journal of Nuclear Materials* 511 (2018) 544-555

Makoto Kobayashi, Masashi Shimada, Chase N. Taylor, Dean Buchenauer, Robert Kolasinski, Takaaki Koyanagi, Yuji Nobuta, Yuji Hatano, Yasuhisa Oya, "Influence of dynamic annealing of irradiation defects on the deuterium retention behaviors in tungsten irradiated with neutron," *Fusion Engineering and Design* 146 (2019) 1624–1627

Huaxin Li, Takaaki Koyanagi, Xunxiang Hu, Yutai Katoh, "Multiscale experimental characterization of coatings on ceramics: A case study of tungsten on SiC," *Surface & Coatings Technology* 367 (2019) 1-10

T. Nozawa, T. Koyanagi, Y. Katoh, H. Tanigawa, "High-dose, intermediate-temperature neutron irradiation effects on silicon carbide composites with varied fiber/matrix interfaces," *Journal of the European Ceramic Society*. 39 (2019) 2634-2647

C.P. Massey, S.N. Dryepondt, P.D. Edmondson, M.G. Frith, K.C. Littrell, A. Kini, B. Gault, K.A. Terrani, S.J. Zinkle, "Multiscale investigations of nanoprecipitate nucleation, growth, and coarsening in annealed low-Cr oxide dispersion strengthened FeCrAl powder," *Acta Materialia* 166 (2019) 1-17

Chad M.Parish, Philip D.Edmondson, "Data visualization heuristics for the physical sciences," *Materials & Design*, 179 (October 2019) 107868, https://doi.org/10.1016/j.matdes.2019.107868 -- https://www.sciencedirect.com/science/article/pii/S0264127519303065

C. M. Parish, L. Garrison, E. Lang, J.-P. Allain, and Y. Katoh, "Tungsten Microstructural Results from the Gadolinium-Shielded 19J Irradiation Experiment," Proceedings of Microscopy and Microanalysis 2019, 25-Suppl 2 (2019) 1600-1601

C. M. Parish, "Fuzzy Clustering to Merge EDS and EBSD Datasets with Crystallographic Ambiguity," Proceedings of Microscopy and Microanalysis 25-Suppl 2 (2019) 134

J. Coburn, E. Unterberg, J. Barton, D. Rudakov, I. Bykov, C. M. Parish, R. Wilcox, C. Lasnier, T. Abrams, J. Watkins, D. L. Hillis, and M. Bourham, "Erosion characterization of SiC and Ti3SiC2 on DIII-D using focused ion beam micro-trenches," *Nuclear Materials and Energy* 19 (2019) 316

J. Rapp, M.E. Rensink, T.D. Rognlien, A.F. Rowcliffe, S. Smolentsev, L.L. Snead, M.S. Tillack, P. Titus, L.M. Waganer, G.M. Wallace, S.J. Wukitch, A. Ying, K. Young, Y. Zhai, "Overview of the fusion nuclear science facility, a credible break-in step on the path to fusion energy," *Fusion Engineering and Design* 135B (2018) 236-270

Adrian S. Sabau, Kazutoshi Tokunaga, Michael G. Littleton, James O. Kiggans Jr., Charles R. Schaich, Ralph B. Dinwiddie, Daniel T. Moore, Yoshio Ueda, and Yutai Katoh, "A 6 MW/m2 High-heat flux Testing Facility of Irradiated Materials using Infrared Plasma-Arc Lamps," *Fusion Science and Technology* 00 (2019) 1-12, DOI: 10.1080/15361055.2019.1623571, Published online: 19 Jun 2019

N. Sridharan, J. Poplawsky, A. Vivek, A. Bhattacharya, W. Guo, H. Meyer, Y. Mao, T. Lee, G. Daehen, "Cascading microstructures in Al-Steel interfaces created by impact welding," *Materials Characterization* 151 (2019) 119-128

Niyanth Sridharan and Kevin Field. "A Road Map for the Advanced Manufacturing of Ferritic-Martensitic Steels," *Fusion Science and Technology* 75 (2019) 264-274

L. Tan, Y. Katoh, L.L. Snead, "Development of castable nanostructured alloys as a new generation RAFM steels," *Journal of Nuclear Materials* 511 (2018) 598-604

M.A. Tunes, R.W. Harrison, S.E. Donnelly, P.D. Edmondson, "A transmission electron microscopy study of the neutron-irradiation response of Ti-based MAX phases at high temperatures," *Acta Materialia* 169 (2019) 237-247

K. Wang, R.P. Doerner, M.J. Baldwin, C.M. Parish, "Flux and fluence dependent helium plasma-materials interaction in hot-rolled and recrystallized tungsten," *Journal of Nuclear Materials* 510 (2018) 80-92

K. Nordlund, S.J. Zinkle, A.E. Sand, F. Granberg, R.S. Averback, R. Stoller, T. Suzudo, L. Malerba, F. Banhart, W.J. Weber, F. Willaime, S. Dudarev and D. Simeone, "Primary radiation damage: A review of current understanding and models," *Journal of Nuclear Materials*, 512 (2018) 450-479

14.2 REPORTS ISSUED IN FY 2019

F.W. Wiffen, Y. Katoh, S. Melton, "Fusion Materials Research at Oak Ridge National Laboratory in Fiscal Year 2018," ORNL/TM-2018/1072, November 2018

"Fusion Materials Semiannual Progress Report for the Period Ending December 31, 2018," DOE-ER-0313/65, March 2019

"Fusion Materials Semiannual Progress Report for the Period Ending June 30, 2019," DOE-ER-0313/66, September 2019

14.3 PAPERS SUBMITTED IN FY 2018 & 2019

(Currently awaiting publication)

Shradha Agarwal, <u>Takaaki Koyanagi, Arunodaya Bhattacharya</u>, Ling Wang, <u>Yutai Katoh, Xunxiang Hu</u>, Michael Pagan, Steven J. Zinkle, "Neutron irradiation-induced microstructure damage in ultra-high temperature ceramic TiC," submitted to *Acta Materialia* 2019

Xiang Chen, Mikhail A. Sokolov, Arunodaya Bhattacharya, Logan N. Clowers, Tim Graening, Yutai Katoh, Michael Rieth, "Master Curve Fracture Toughness Characterization of Eurofer97 Steel Variants Using Miniature Multi-Notch Bend Bar Specimens for Fusion Applications," accepted, *ASME PVP2019-93797*

Takashi Nozawa, Hideo Sakasegawa, <u>Xiang Chen</u>, Taichiro Kato, <u>Josina W. Geringer, Yutai Katoh</u>, Hiroyasu Tanigawa, "Non-contact strain evaluation for miniature tensile specimens of neutron-irradiated F82H by digital image correlation," submitted to *Fusion Engineering and Design*

M. Shimada, Y. Oya, W.R. Wampler, Y. Yamauchi, C.N. Taylor, <u>L.M. Garrison</u>, D.A. Buchenauer, and Y. Hatano, "Deuterium Retention in Neutron-Irradiated Single-Crystal and Polycrystalline Tungsten," accepted by *Fusion Engineering and Design*

Eric Lang, Nathan Reid, <u>Lauren Garrison, Chad Parish</u>, J.P. Allain. "Pre-irradiation comparison of W-based alloys for the PHENIX campaign: microstructure, composition, and mechanical properties," submitted to *Fusion Science and Technology,* December 2018

Nathan C. Reid, <u>Lauren M. Garrison</u>, Chase N. Taylor, and Jean Paul Allain, "Elemental Characterization of Neutron Irradiated Tungsten Using the GD-OES Technique," submitted to *Fusion Science and Technology,* December 2018

L. M. Garrison, A. S. Sabau, B. Gregory, J. W. Geringer, Y. Katoh, Y. Hamaji and A. Hasegawa. "Plasma-Arc Lamp High Heat Flux Cycling Exposure of Neutron Irradiated Tungsten Materials," submitted to *Physica Scripta*, June 2019.

C. Li, <u>X. Hu</u>, T. Yang, NAP Kiran Kumar, B.D. Wirth, S.J. Zinkle, "Neutron irradiation response of a Co-free high entropy alloy," submitted to *Acta Materialia*

Katherine Haynes, <u>Xunxiang Hu</u>, Congyi Li, Brian Wirth, Christopher Hatem, and Kevin Jones, "Influence of Dose Rate on Defects Formed in Silicon during Elevated Temperature Helium Implantation," submitted to *Journal of Applied Physics*

Shaw, Guinevere; Garcia, Wendy; <u>Hu, Xunxiang</u>; Wirth, Brian, "Investigating Helium – Hydrogen Synergies in Plasma Exposed Tungsten using Laser Ablation Techniques," accepted by *Physica Scripta*

Yuji Hatano, Daniel Clark, Yoshio Ueda, <u>Yutai Katoh</u>, Takehiko Yokomine, Minami Yoda, <u>Adrian S. Sabau</u>, Tatsuya Hinoki, Akira Hasegawa, <u>Lauren M. Garrison, J. Wilna Geringer</u>, Yasuhisa Oya, Masashi Shimada, Dean Buchenauer, Takeo Muroga, "Overview of Japan-US Project PHENIX: Technological Assessment of He-Cooled Divertor with Tungsten for DEMO Reactors"

D.J. Sprouster, L.L Snead, E. Dooryhee, S.K. Ghose, <u>T. Koyanagi</u> and <u>Y. Katoh</u>, "Pair Distribution Function Analysis of Neutron-Irradiated Silicon Carbide", under review by *Journal of Nuclear Materials*

J. Jun, K. A. Unocic, M. J. Lance, H. M. Meyer and B. A. Pint, "Compatibility of Alumina-Forming Steel with Flowing PbLi at 500°-650°C," submitted to *Journal of Nuclear Materials*

J. Coburn, T. Gebhart, C. Parish, E. Uterberg, J. Canik, M. Barsoum, M. Bourham, "Surface Erosion of Plasma-Facing Materials Using an Electrothermal Plasma Source and Ion Beam Micro-Trenches," submitted to *Fusion Science and Technology*

14.4   PRESENTATIONS DELIVERED IN FY 2019

(*OFES-funded ORNL Authors, by date presented*)

At NuMat 2018: The Nuclear Materials Conference, Seattle, WA, October 14-18, 2018

A. Bhattacharya, T. Koyanagi, C.M. Parish, C. Ang, D. King, G. Hilmas, S.J. Zinkle, Y. Katoh, "Nano-scale microstructure damage by neutron irradiations in novel Boron-11 enriched TiB_2 ultra-high temperature ceramic"

Yutai Katoh, Caen Ang, Phil Edmondson, Phillip Shih, Chad Parish, Matt Tunes, "Property Evolutions of Neutron-irradiated Ti-Si-C and Ti-Al-C MAX-phase Materials"

Takaaki Koyanagi, Kurt Terrani, Yutai Katoh, Torill Karlsen, Vendi Andersson, David Sprouster, Lynne Ecker, **"**In-pile tensile creep of high-purity silicon carbide at 300°C"

Kun Wang, Chad M. Parish, Kevin G. Field, Lizhen Tan, Yutai Katoh, "Microstructural evolution of reduced activation ferritic/martensitic (RAFM) steels after neutron-irradiation up to 72 dpa"

S. Agarwal, T. Koyanagi, Y. Katoh, X. Hu, W.J. Weber, S.J. Zinkle," Microstructural characterization of neutron-irradiated polycrystalline TiC"

Ling Wang, Arunodaya Bhattacharya, Chad M. Parish, Spencer Kropf, David Martin, Brian D. Wirth, and Steven J. Zinkle, "Microstructural evaluation of coherent precipitates in ion irradiated model binary alloys"

C.M. Parish. K. Wang, A. Bhattacharya, P.D. Edmondson, R.P. Doerner, M. Baldwin, and Y. Katoh, "Advanced EBSD- and STEM-based methodologies for studying nuclear materials"

Seminars at the Nuclear, Plasma, and Radiological Engineering Department, University of Illinois

Chad M. Parish, " Advanced EBSD-and STEM-based methodologies for studying materials for extreme environments" – October 2018

Lauren M. Garrison, "Materials for Fusion Reactors: Where are we now?" - January 2019

At TOFE 2018, The Technology of Fusion Energy, an Embedded ANS Topical Meeting, Orlando, FL, November 12-15, 2018

Oral Presentations

P.D. Edmondson, "Effects of Neutron Irradiation on the Microstructure and Superconductivity of Second-generation High Temperature Superconductors Irradiated in HFIR"

Lauren M. Garrison, Yutai Katoh, Wilna Geringer, Masafumi Akiyoshi, Xiang Chen, Makoto Fukuda, Akira Hasegawa, Tatsuya Hinoki, Xunxiang Hu, Takaaki Koyanagi, Eric Lang, Michael McAlister, Joel McDuffee, Takeshi Miyazawa, Chad Parish, Emily Proehl, Nathan Reid, Janet Robertson, Hsin Wang, *"*PHENIX US-Japan Collaboration Investigation of Thermal and Mechanical Properties of Thermal Neutron Shielded Irradiated Tungsten*"*

N. Reid, <u>L. Garrison</u>. J. Allain, "Elemental Characterization of Neutron Irradiated Tungsten using the GD-OES Technique"

J. Jun, B.A. Pint, K.A. Unocic, "Thermal Convection Loop Testing of an FeCrMo Alloy at 450-700°C"

Yutai Katoh, Takaaki Koyanagi, Arunodaya Bhattacharya, Chad M. Parish, Philip D. Edmondson, Caen Ang, Lizhen Tan, Charles H. Henager, Jr., Lance L. Snead, Steven J. Zinkle, *"Potential of Emerging Engineering Materials for Fusion Energy Applications"*

C.E. Kessel, et al (<u>Y. Katoh, B.A. Pint, A.F. Rowcliffe</u>), "An Exploration of Liquid Metal Plasma Facing Components for Fusion"

J. McDuffee, "Irradiation Capabilities and Outlook for Fusion Materials Research"

Adrian S. Sabau, Kazutoshi Tokunaga, Jim Kiggans, Charles R. Schaich, Michael G. Littleton, Daniel T. Moore, Yoshio Ueda, and Yutai Katoh, *"A 12 MW/m^2 High-Heat Flux Testing Facility of Irradiated Materials Using Infrared Plasma-Arc Lamps"*

N. Sridharan, M. Gussev, K. Field, "Advanced Manufacturing of Ferritic Martensitic Steels for Fusion Reactors"

K. Wang, et al, "Surface Roughness and Exposure Energy Effect on the Surface Nanofuzz Growth of Tungsten"

Poster Presentations

E. Lang, L. Garrison, C. Parish, J. Allain, "Effect of Re Doping on W Behavior: Microstructure, Mechanical Properties, and Response to Low Energy He/D Irradiation"

D.R. Patel, <u>T. Koyanagi</u>, "High Temperature Creep Properties of Nuclear-Grade Generation III SiC Fibers"

Eric Lang, Nathan Reid, Lauren Garrison, Chad Parish, J.P. Allain. "Pre-irradiation comparison of W-based alloys for the PHENIX campaign: microstructure, composition, and mechanical properties"

US/Japan Workshop on Fusion Power Plants, Next Steps and Fusion Technologies. ORNL, December 13-15, 2018

Lauren M. Garrison, Yutai Katoh, Josina W. Geringer, Masafumi Akiyoshi, Xiang Chen, Makoto Fukuda, Akira Hasegawa, Tatsuya Hinoki, Xunxiang Hu, Takaaki Koyanagi, Eric Lang, Michael McAlister, Joel McDuffee, Takeshi Miyazawa, Chad Parish, Emily Proehl, Nathan Reid, Janet Robertson, Hsin Wang. "PHENIX US-Japan Collaboration Investigation of Thermal and Mechanical Properties of Thermal Neutron Shielded Irradiated Tungsten"

IAEA 2nd RCM of the CRP on "Towards the Standardization of Small Specimen Test Techniques for Fusion Applications," January 9-11, 2019, Vienna, Austria

X. Chen, M.A. Sokolov, L.N. Clowers, "Master Curve Fracture Toughness Characterization of RAFM Steels for Fusion Applications,"

At IAEA-India: 27ᵗʰ IAEA Fusion Energy Conference, October 22–27, 2018 Ahmedabad, India

H. Tanigawa, E. Diegele, Y. Katoh, T. Nozawa, T. Hirose, M. Gorley, H. Sakasegawa, E. Gaganidze, J. Aktaa, G. Pintsuk, "The strategy of fusion DEMO in-vessel structural material development"

At the MRS Fall Meeting & Exhibition, Boston, MA November 25-30, 2018

Hiroyasu Tanigawa, Masami Ando, <u>Yutai Katoh</u>, Naoyuki Hashimoto, Takuya Nagasaka, "Tensile deformation and fracture mechanism of irradiated RAFM steel"

At the TMS Annual Meeting, San Antonio, TX March 10-14, 2019

A. Bhattacharya, C.M. Parish, J. Henry, N. Sridharan, Y. Yang, L. Tan, Y. Katoh, "High throughput characterization of nano-size precipitates in steels: Transmission Kikuchi diffraction on extraction replicas"

A. Bhattacharya, S.J. Zinkle, P.D. Edmondson, C.M. Parish, T. Koyanagi, Y. Katoh, "Revealing anisotropic swelling trends in irradiated hexagonal/trigonal materials"

Y. Zhao, <u>A. Bhattacharya</u>, J. Henry, S.J. Zinkle, "Ion irradiation induced alpha prime precipitate formation in high purity Fe-Cr alloys"

L. Wang, <u>A. Bhattacharya</u>, C.M. Parish, S. Kropf, D. Martin, B.D Wirth, S.J. Zinkle, "Quantification of 1D vs 3D Defect Migration Behavior in Ion Irradiated Dilute Copper Base Binary Alloys"

C.M. Parish, K. Wang, T. Song, M. Baldwin, and R. Doerner, " Combined nanomechanical and high-resolution microscopy to understand plasma-surface interactions in fusion energy materials"

Ling Wang, Ying Yang, Lance L. Snead, and Steven J. Zinkle, "Tensile and thermal creep behavior of a novel copper alloy for fusion energy applications"

P.D. Edmondson, S. Pedrazzini, "Using atom probe tomography to understand neutron irradiated effects in high temperature superconductors for nuclear fusion applications"

Lauren M. Garrison, Yutai Katoh, Akira Hasegawa, Takeshi Miyazawa, "Mechanical Properties of Tungsten Irradiated with a Thermal Neutron Shield"

S.J. Zinkle, Tengfei Yang, and Congyi Li, "Radiation Effects in High Entropy Alloys: Similarities and Differences with Conventional Alloys"

At the MRS Spring Meeting, Phoenix, AZ April 22-26, 2019

Elizabeth A. I. Ellis, Michael M. Kirka, Chase B. Joslin, Lauren M. Garrison, Christopher Ledford, Sullivan Figurskey, Chris Rock, Timothy J. Horn, Yutai Katoh, and Ryan R. Dehoff, "Texture in Electron Beam Melted Tungsten for Fusion Power"

At the PFMC, Eindhoven, Netherlands, 21-25 May 21-25, 2019

Y. Katoh, L.M. Garrison, X. Hu, T. Koyanagi, C.M. Parish, P.D. Edmondson, L.L. Snead, M. Fukuda, and A. Hasegawa, "Properties and microstructural evolutions of tungsten under mixed spectrum neutron irradiation"

C. M. Parish (Invited), L. M. Garrison, K. Wang, K. G. Field, X. Hu, and Y. Katoh, "Neutron-irradiation-induced microstructures in tungsten and ferritic-martensitic steels analyzed using advanced electron microscopy"

L.M. Garrison, A.S. Sabau, B. Gregory, J.W. Geringer, Y. Katoh, Y. Hamaji and A. Hasegawa, "Plasma-Arc Lamp High Heat Flux Cycling Exposure of Neutron Irradiated Tungsten Materials"

X. Hu, J. Qiu, C. Li, B.D. Wirth, Y. Katoh, "Investigation of Helium Retention in Tungsten Through a Combined Experimental and Modelling Approach"

Yoshio Ueda, Daniel Clark, Yuji Hatano, Tastuya Hinoki, Akira Hasegawa, Yutai Katoh, Lauren M. Garrison, Yasuhisa Oya, Masashi Shimada, Dean Buchenauer, Takeshi Miyazawa, Yuji Yamauchi, Yuji Nobuta, Yukinori Hamaji, Adrian S. Sabau, Josina Wilna Geringer, "Mechanical Property, Microstructure and Hydrogen Isotope Retention of Neutron-Irradiated Tungsten and Advanced Tungsten Materials"

At the 28th IEEE Symposium on Fusion Engineering, in Jacksonville, Florida June 2-6, 2019

Y. Katoh, L.M. Garrison, X. Hu, T. Koyanagi, C.M. Parish, P.D. Edmondson, L.L. Snead, M. Fukuda, A. Hasegawa, "Properties of tungsten after mixed spectrum neutron irradiation"

Lauren M. Garrison, Yutai Katoh, M. Gussev, "Mechanical and interface properties of sintered tungsten-copper composite after neutron irradiation"

At the 6th Fusion Materials Theory & Modeling Workshop, in Walla Walla, WA, June 24-26, 2019, an IEA Fusion Materials Technology Cooperation Program activity

X. Hu, "Experimental investigation of gas behavior in fusion materials and modeling needs"

Yuri Osetskiy, "Atomic-scale hardening mechanisms due to localized obstacles"

At Microscopy and Microanalysis 2019, Portland, OR, August 4-8, 2019

C. M. Parish (Oral), "Fuzzy Clustering to Merge EDS and EBSD Datasets with Crystallographic Ambiguity"

C. M. Parish (Poster), L. Garrison, E. Lang, J.-P. Allain, and Y. Katoh, "Tungsten Microstructural Results from the Gadolinium-Shielded 19J Irradiation Experiment"

At the 14th International Symposium on Fusion Nuclear Technology, in Budapest, Hungary, September 22-27, 2019

A. Bhattacharya, X. Chen, "Advanced structural steels for the fusion reactor: alloy development, irradiation effects and characterization at ORNL"

Xiang (Frank) Chen, Arunodaya Bhattacharya, Tim Graening, Anne A. Campbell, Logan N Clowers, Mikhail A. Sokolov, Josina W. Geringer, Janet Robertson, Yutai Katoh, Michael Rieth, "Fracture Toughness Evaluation of Neutron Irradiated Eurofer97 Using Miniature Bend Bars"

At the 10th International Conference on High Temperature Ceramic Matrix Composites (HT-CMC 10) in Bordeaux, France, September 22-26, 2019

Takaaki Koyanagi, Huaxin LI, Caen Ang, Yutai Katoh, "Electron current assisted direct joining of low resistivity grade silicon carbide"

Yutai Katoh, Takaaki Koyanagi, Arunodaya Bhattacharya, Chad Parish, Philip Edmondson, Caen Ang, Lance Snead, "Opportunities for High Temperature Ceramics and Composites in Fusion Energy Applications"